
Resolving the Hubble Tension with Early Dark Energy

Laura Herold



München 2023

Resolving the Hubble Tension with Early Dark Energy

Laura Herold

Dissertation
an der Fakultät für Physik
der Ludwig–Maximilians–Universität
München

vorgelegt von
Laura Christa Herold
aus Nürnberg

München, den 14. April 2023

Erstgutachter: Prof. Dr. Eiichiro Komatsu

Zweitgutachter: Prof. Dr. Daniel Grün

Tag der mündlichen Prüfung: 30. Mai 2023

Contents

Zusammenfassung	xiii
Abstract	xv
1 The Standard Cosmological Model	1
1.1 Introduction	2
1.2 Friedmann-Lemaître-Robertson-Walker Universe	2
1.3 Distances in an expanding Universe	5
1.4 Inflation	6
1.4.1 Dynamics of a scalar field in an expanding Universe	7
1.4.2 Cosmological perturbation theory	8
1.5 Growth of structure	10
1.5.1 From inflation to the cosmic microwave background	10
1.5.2 Boltzmann equations for linear perturbations	11
1.5.3 Non-linear growth: one-loop perturbation theory	12
1.5.4 Redshift space distortions and Alcock-Paczyński effect	16
1.5.5 Effective field theory of large scale structure	18
2 The Hubble Tension and Early Dark Energy	25
2.1 The Hubble tension	26
2.2 Indirect measurements of H_0	26
2.2.1 The cosmic microwave background	26

2.2.2	Baryon acoustic oscillations in galaxy surveys	30
2.3	Direct measurements of H_0	31
2.3.1	Cepheid-calibrated Type Ia SNe	31
2.3.2	TRGB-calibrated Type Ia supernovae	32
2.3.3	Gravitational-lens time delays	32
2.3.4	Type II SNe	33
2.3.5	Other measurements of the Hubble tension	33
2.4	New physics to resolve the Hubble tension?	34
2.5	A possible solution: Early Dark Energy	35
2.5.1	The axion-like EDE model	36
2.5.2	Dynamics of the EDE model	37
2.6	Can Early Dark Energy resolve the Hubble tension?	41
2.6.1	EDE constraints from <i>Planck</i> CMB and BAO data	41
2.6.2	EDE constraints from LSS	43
2.6.3	Prior volume effects in the EDE model?	44
2.6.4	Ground-based CMB experiments prefer EDE	45
2.7	Other proposed solutions to the Hubble tension	45
3	Statistics of Cosmological Parameter Inference	47
3.1	Parameter estimators	48
3.1.1	Maximum likelihood estimator	48
3.1.2	Least squares estimator	48
3.2	Bayes' theorem	49
3.3	Treatment of nuisance parameters	50
3.3.1	The profile likelihood	50
3.3.2	Marginalization	50
3.4	Frequentist confidence intervals	51
3.4.1	The Neyman construction	51

3.4.2	The Feldman-Cousins prescription	53
3.5	Bayesian credible intervals	57
3.5.1	Markov Chain Monte Carlo	58
4	New Constraint on Early Dark Energy using the Profile Likelihood	61
4.1	Introduction	62
4.2	The EDE model	64
4.3	Deconstructing the current constraints on the EDE model	65
4.3.1	Data and methodology	65
4.3.2	Grid Sampling	65
4.3.3	Profile likelihood	67
4.4	Constructing Confidence Intervals: Profile likelihood	69
4.5	Discussion and conclusion	69
4.6	Supplementary material	71
4.6.1	Preliminary studies using MCMC techniques	71
4.6.2	Best fit and $\Delta\chi^2$ of grid analysis	71
4.6.3	Best-fit values of the parameters for different cosmologies	71
5	Resolving the Hubble tension with Early Dark Energy	77
5.1	Introduction	78
5.2	Early Dark Energy	79
5.3	Analysis Methods	80
5.3.1	Data and modeling	80
5.3.2	Statistical inference: MCMC and profile likelihood	80
5.4	Results and discussion	81
5.4.1	<i>Planck</i> + BOSS full-shape analysis (baseline)	82
5.4.2	Baseline + DES	83
5.4.3	Baseline + SHOES	84

5.4.4	<i>Planck</i> -only constraint and comparison to ACT	84
5.5	Conclusion	85
5.6	Supplementary material	86
5.6.1	Parameter correlations	86
5.6.2	Best-fit parameters and χ^2 contributions	87
6	Cosmological Concordance with Early Dark Energy and Massive Neutrinos?	91
6.1	Introduction	92
6.2	EDE and massive neutrinos	92
6.3	Datasets and methodology	93
6.4	Markov Chain Monte Carlo analysis	94
6.5	Profile likelihood analysis	96
6.6	Conclusions	101
6.7	Supplementary material	101
6.7.1	MCMC for different data set combinations	101
6.7.2	Shifts in nuisance parameters	102
6.7.3	Details about the convergence of the profile-likelihood analysis for cosmologies with EDE and neutrinos	102
7	Conclusions and Outlook	109
	Acknowledgements	126

List of Figures

2.1	CMB temperature power spectrum as measured by <i>Planck</i>	27
2.2	The axion-like EDE potential	37
2.3	Fractional energy density of EDE for different values of the index and initial field value	38
2.4	Total energy density for different species in an EDE cosmology	39
2.5	Relation between the phenomenological and particle-physics parametrization of EDE	40
2.6	Fractional energy density of EDE and expansion rate as a function of redshift	42
3.1	Neyman confidence belt	52
3.2	Likelihood ratio in Feldman-Cousins construction	55
3.3	Feldman-Cousins confidence belt	57
4.1	Grid analysis of EDE showing the mean values of f_{EDE}	66
4.2	Profile likelihood of the fraction of EDE from <i>Planck</i> and BOSS full-shape data	68
4.3	Summary of EDE constraints	70
4.4	Posteriors of different 1-parameter EDE models	72
4.5	MCMC with fixed values of f_{EDE}	73
4.6	Grid analysis of EDE showing the best-fit values of f_{EDE} and $\Delta\chi^2$ values	74
5.1	Profile likelihoods in f_{EDE} for different data sets	81
5.2	Profile likelihoods in H_0 for different data sets	82
5.3	Summary of H_0 constraints	85

5.4	Parameter correlations with f_{EDE}	87
6.1	MCMC posteriors of full 3-parameter EDE model for <i>Planck</i> and BOSS full-shape data	95
6.2	MCMC posteriors of 1-parameter EDE model for <i>Planck</i> and BOSS full-shape data	97
6.3	χ^2 contributions and variation of best-fit values of selected cosmological parameters as a function of M_ν	99
6.4	BAO angular scale within EDE at fixed values of M_ν	100
6.5	MCMC posteriors of the full 3-parameter EDE model for different data sets . . .	103
6.6	MCMC posteriors of the full 3-parameter EDE model for different data sets including DES	104
6.7	Smoothed minimization chains of the full 3-parameter EDE model for <i>Planck</i> and BOSS BAO + full-shape for different M_ν	105
6.8	Profile likelihood in M_ν for run 1	106
6.9	Profile likelihood in M_ν for run 1, 2, 3, 4	107
6.10	Final profile likelihood in M_ν based on run 4	108
7.1	Profile likelihood results of the initial energy density fraction of Λ CDM	110
7.2	Posterior distribution of the parity-violating coupling of EDE and photons	111

List of Tables

2.1	Overview of selected constraints on the fraction of EDE in the literature	42
3.1	Confidence intervals obtained from the Feldman-Cousins prescription	56
4.1	Best-fit parameters for Λ CDM and EDE cosmologies.	74
5.1	χ^2 values for Λ CDM and EDE models	81
5.2	Constraints on f_{EDE} and H_0	82
5.3	Best-fit parameters and χ^2 contributions for Λ CDM and EDE models	88
5.4	Global best-fit parameters	89
6.1	Breakdown of χ^2 contributions and best-fit values of selected cosmological parameters	98
6.2	Minimum χ^2 for run 1 to 4 for M_ν fixed	107

Zusammenfassung

Verschiedene Messungen der Hubble-Konstante, einem Maß für die Ausdehnungsgeschwindigkeit des Universums, ergeben abweichende Werte. Kann diese Diskrepanz – bekannt als “Hubble-Tension” – nicht durch systematische Fehler in den Messungen erklärt werden, so könnte sie ein Hinweis auf neue physikalische Effekte jenseits des Standard- Λ CDM-Modells sein. Ein vielversprechendes Modell zur Behebung dieser Diskrepanz ist *frühe dunkle Energie* (Early Dark Energy, EDE), eine Form von dunkler Energie, die im frühen Universum auftreten soll. In der Literatur besteht jedoch kein Konsens darüber, ob das EDE-Modell sowohl die Hubble-Tension lösen als auch die gute Übereinstimmung mit den Daten des kosmischen Mikrowellenhintergrunds und der großräumigen Struktur des Universums erhalten kann.

In dieser Dissertation beginnen wir mit einem kurzen Überblick über die nötigen Konzepte des Standard- Λ CDM-Modells, der Hubble-Tension, EDE und Statistik. Wir untersuchen den Ursprung gegensätzlicher Schlussfolgerungen zu EDE in der Literatur mithilfe einer Rasteranalyse und finden Hinweise darauf, dass technische Effekte in der Markov-Chain-Monte-Carlo-Analyse, sogenannte Volumeneffekte, eine große Rolle spielen und den Dissens in der Literatur erklären können. Um Konfidenzintervalle zu konstruieren, die unabhängig von Volumeneffekten sind, verwenden wir die Profile-Likelihood-Methode, eine Methode aus der frequentistischen Statistik, die selten für Analysen in der Kosmologie genutzt wird. Mithilfe des Profile-Likelihoods finden wir, dass das EDE-Modell in der Lage ist, die Hubble-Konstante zu erhöhen, um die Hubble-Tension unter eine Signifikanz von $1,7\sigma$ zu reduzieren, während gleichzeitig eine gute Übereinstimmung mit allen in dieser Dissertation betrachteten Datensätzen gewährleistet wird. Obwohl EDE damit vielversprechende Eigenschaften in Bezug auf die Auflösung der Hubble-Tension zeigt, führt es auch zu einer erhöhten Amplitude der Dichteschwankungen im späten Universum, S_8 , was bereits vorhandene Diskrepanzen bei Messungen von S_8 verschlechtert. Wir untersuchen eine natürliche Erweiterung des EDE-Modells, die die Summe der Neutrinomassen als freien Parameter enthält, und bewerten, ob höhere Neutrinomassen die EDE-induzierte Erhöhung von S_8 kompensieren können. Unsere Ergebnisse zeigen, dass dieses Szenario jedoch durch Messdaten der großräumigen Struktur des Universums stark eingeschränkt ist. Wir schlussfolgern, dass das EDE-Modell ein möglicher Kandidat zur Auflösung der Hubble-Tension ist, während die gleichzeitige Behebung der S_8 -Diskrepanz anderer Erklärung bedarf.

Abstract

With the increasing precision of cosmological measurements, a number of discrepancies have emerged among which the *Hubble tension*, a mismatch between different measurements of the current expansion rate of the Universe, is the most significant. If not caused by systematics in the measurements, this tension could be a hint of new physics beyond the standard Λ CDM model. One of the most promising proposed solutions to this tension is *Early Dark Energy* (EDE), which introduces a dark-energy-like component in the early Universe that decays very quickly around recombination. However, there is no consensus in the literature whether the tension-resolving EDE model can provide an adequate fit to cosmological data of the cosmic microwave background and large-scale structure (LSS) of the Universe. Further, it has been suggested that prior volume effects influence the constraints of the EDE model from Markov Chain Monte Carlo (MCMC) analyses, which originate in the specific parametrization of the model, and lead to a strong dependence of the constraints on the prior.

In this thesis, we begin by giving a brief overview about the necessary concepts of the standard Λ CDM model, the Hubble tension, EDE, and statistics. In order to understand the origin of different conclusions about EDE in the literature, we deconstruct the current constraints using a grid analysis and find evidence that prior volume effects affect the constraints of the EDE model from an MCMC analysis, suggesting that these effects are the reason behind the disagreement in the literature. Motivated by this, we use a profile-likelihood analysis to construct confidence intervals for the parameters of the EDE model. The profile likelihood, which is rarely used for cosmological parameter inference, is a standard tool in frequentist statistics to construct confidence intervals, which are independent of a prior and hence serve as a powerful tool to assess the influence of prior volume effects. With the profile likelihood, we find that the EDE model is able to raise the Hubble constant in order to reduce the Hubble tension below a significance of 1.7σ , while presenting a good fit to all data sets considered in this thesis. Although EDE shows promising properties with regards to resolving the Hubble tension, it is well known that introducing EDE comes at the cost of an increased clustering amplitude, which worsens the already existing tension in measurements of the clustering amplitude. We explore one well-motivated extension of the EDE model, which includes the sum of neutrino masses as a free parameter, and assess whether higher neutrino masses can compensate the EDE-induced clustering enhancement. We find that this scenario is disfavored since higher neutrino masses within the EDE model are tightly constrained by LSS data.

Chapter 1

The Standard Cosmological Model

Sections 1.2, 1.4 closely follow the Cosmology lecture by Prof. Kristina Giesel at Friedrich Alexander University in 2018/2019. Section 1.3 follows Weinberg (2008) (their Chapter 1.4) and Dodelson and Schmidt (2020) (their Chapter 2.2.). Section 1.4 follows Dodelson and Schmidt (2020) (their Chapter 7). Section 1.5 follows Jeong and Komatsu (2006), Weinberg (2008) (their Chapter 2 and 3), Dodelson and Schmidt (2020) (their Chapter 8 and 11), and Baldauf (2020).

Summary: In this chapter, we will give a brief overview about the mathematical description of the ‘standard cosmological model’, which starts with the homogeneous and isotropic Universe described by the Friedmann-Lemaître-Robertson-Walker metric (Sec. 1.2). Inflation, a phase of accelerated expansion (Sec. 1.4), explains the homogeneity and isotropy and the origin of the large-scale structure (LSS) of the Universe, which is described in the framework of linear perturbation theory. To describe the non-linear gravitational growth of structure in the late Universe, linear perturbation theory is not sufficient and we will sketch one-loop perturbation theory (Sec. 1.5). We give an overview of one example to describe non-perturbative effects, which is the effective field theory of large-scale structure (Sec. 1.5.5).

1.1 Introduction

The discovery of the theory of general relativity, the detection of the (accelerated) expansion of the Universe, and the evidence for an invisible dark matter component in galaxies, along with the measurement of the cosmic microwave background (CMB) are important milestones that led to the *standard cosmological model*. In this model, the Universe is expanding, meaning that at earlier times, the Universe was hotter, smaller and denser. If we take this argument back in time, at some point the Universe was so dense, hot and small that it was in a regime where physical theories do not apply anymore and a singularity happens, usually called the *Big Bang*. For this reason, this model is also called the Big Bang model.

Inflation provides an explanation for the small initial perturbations out of which the large-scale structure (LSS) of the Universe formed. Observations of the CMB and LSS can give a precise picture of the composition of the Universe. Only about 5% of the energy of the Universe is composed of the common baryonic matter, while the rest is composed of dark components: about 25% of the energy consist of *cold dark matter* (CDM), which has so far only been detected by its gravitational interaction and is known to be largely non-relativistic (‘cold’). The bulk of the energy, about 75%, is contained in *dark energy*, a dark component with negative pressure, which is typically modeled by a cosmological constant, Λ , and can explain the accelerated expansion of the Universe. The standard cosmological model Λ CDM is named after these dark components and presents a remarkably good fit to all cosmological observations.

1.2 Friedmann-Lemaître-Robertson-Walker Universe

Gravity, the force that governs the Universe at large scales, is described by Einstein’s equations

$$R^{\mu\nu} - \frac{R}{2}g^{\mu\nu} + \Lambda g^{\mu\nu} = \frac{\kappa}{2}T^{\mu\nu}, \quad (1.1)$$

where $R^{\mu\nu}$ is the Riemann tensor, R the Ricci scalar, $g^{\mu\nu}$ the metric tensor, Λ the cosmological constant, $\kappa = 16\pi G_N$ is related to Newton’s constant, G_N , and $T^{\mu\nu}$ is the energy-momentum tensor (see e.g. Wald, 1984; Misner *et al.*, 1973). Einstein’s equations (1.1) are the centerpiece of the theory of general relativity (GR) and they describe how gravity can be understood as curvature of spacetime: “Space (g) tells matter (T) how to move, matter (T) tells space (g) how to curve” (Misner *et al.*, 1973).

On large scales, the Universe appears spatially homogeneous and isotropic. The assumption of spatial homogeneity and isotropy is known as the *Cosmological Principle* and is related to the premise that we – as observers – are not located at a special place in the Universe. If one assumes the Cosmological Principle, the spacetime metric, $g^{\mu\nu}$, simplifies to the *Friedmann-Lemaître-Robertson-Walker* (FLRW; Friedmann, 1922; Robertson, 1935; Walker, 1937) metric:

$$ds^2 = -dt^2 + a^2(t) \frac{\delta_{ab}}{1 + \frac{k}{4} \sum_c (x^c)^2} dx^a dx^b, \quad (1.2)$$

where t denotes cosmological time and x comoving spatial coordinates. k is the curvature of the Universe, which can take on $k = -1$ (hyperbolic topology), $k = 0$ (flat topology) and $k = 1$ (spherical topology). The only degree of freedom of the FLRW metric is the *scale factor* $a(t)$, which describes the scale of the volume of the Universe. In an expanding Universe, $a(t)$ grows as a function of time, t . Inserting the FLRW metric (1.2) into the Einstein equations (1.1) and assuming the energy-momentum tensor of a *perfect fluid*¹, $T_{\mu\nu}^{\text{pf}} = (\rho + p)u_\mu u_\nu + pg_{\mu\nu}$, u_μ being the 4-velocity of the observer, one obtains the Friedmann equations (Friedmann, 1922):

$$\left(\frac{\dot{a}}{a}\right)^2 + \frac{k}{a^2} = \frac{8\pi G_{\text{N}}}{3}\rho + \frac{\Lambda}{3}, \quad (1.3a)$$

$$\frac{\ddot{a}}{a} = -\frac{4\pi G_{\text{N}}}{3}(\rho + 3p) + \frac{\Lambda}{3}, \quad (1.3b)$$

where $\rho(t)$ and $p(t)$ are the energy density and pressure of the fluid, respectively. As discussed in the Introduction, observations suggest that the Universe consists of dark energy given by the cosmological constant Λ , cold dark matter ρ_{c} , baryonic matter ρ_{b} , and radiation ρ_{r} . By inserting Eq. (1.3b) into the temporal derivative of Eq. (1.3a), one obtains the continuity equation

$$\dot{\rho} = -3(\rho + p)\frac{\dot{a}}{a}. \quad (1.4)$$

Note that the terms proportional to Λ and k cancel. The Friedmann equations (1.3a), (1.3b) and the continuity equation (1.4) describe the expansion of space given a specific energy composition of the Universe. The central parameter, which describes the rate of expansion of the Universe, is the *Hubble-Lemaître parameter*:

$$H(t) = \frac{\dot{a}}{a}. \quad (1.5)$$

Particularly interesting is the expansion rate of the Universe *today*, $t = t_0$, which is given by the *Hubble constant* or *Hubble-Lemaître constant*:

$$H_0 = H(t = t_0). \quad (1.6)$$

The first Friedmann equation (1.3a) can be rewritten in terms of the Hubble-Lemaître parameter, Eq. (1.5):

$$H^2(t) = \frac{8\pi G_{\text{N}}}{3}\rho_{\text{tot}} - \frac{k}{a^2}, \quad (1.7)$$

where $\rho_{\text{tot}} = \frac{\Lambda}{8\pi G_{\text{N}}} + \rho_{\text{c}} + \rho_{\text{b}} + \rho_{\text{r}}$. It is common to assume a linear equation of state, i.e. $p = w\rho$, where w is the equation-of-state parameter of the fluid. On large scales, one finds that the linear relationship holds approximately: for dark matter and baryonic matter: $w = 0$; for radiation: $w = 1/3$, and for a cosmological constant (Λ): $w = -1$. Inserting the linear equation of state

¹One can show that the energy-momentum tensor of the perfect fluid is the most general energy-momentum tensor that satisfies spatial homogeneity and isotropy.

into the continuity equation (1.4), the energy density as a function of the scale factor takes the form:

$$\frac{\rho(t)}{\rho_0} = \left(\frac{a(t)}{a_0} \right)^{-3(1+w)}, \quad (1.8)$$

where ρ_0 and a_0 are energy density and scale factor today, respectively. The *fractional energy density* is defined as

$$\Omega_I = \frac{\rho_I}{\rho_{\text{crit}}}, \quad \text{where} \quad \rho_{\text{crit}} = \frac{3H^2}{8\pi G_{\text{N}}} \quad (1.9)$$

for $I \in \{c, b, r, \Lambda\}$. ρ_{crit} is the critical density for which the curvature vanishes, $k = 0$. Hence for a flat Universe, $\rho_{\text{crit}} = \rho_{\text{tot}}$. Inserting Eq. (1.8) into Eq. (1.7) and defining $\rho_k := -\frac{3}{8\pi G_{\text{N}}} \frac{k}{a^2}$, one obtains the Friedmann equation in terms of fractional energy densities (1.9):

$$\frac{H^2(a)}{H_0^2} = \Omega_{r,0} \left(\frac{a_0}{a} \right)^4 + \Omega_{m,0} \left(\frac{a_0}{a} \right)^3 + \Omega_{k,0} \left(\frac{a_0}{a} \right)^2 + \Omega_{\Lambda,0}, \quad (1.10)$$

where $\Omega_{I,0}$ denotes the fractional energy density today (the index 0 will be omitted from now on) and $\Omega_m = \Omega_c + \Omega_b$. Defining the dimensionless Hubble constant

$$h = \frac{H_0}{100 \text{ km/s/Mpc}} \quad (1.11)$$

and the physical fractional energy densities $\omega_I = h^2 \Omega_I$, one can rewrite Eq. (1.10) as

$$\frac{H^2(a)}{(100 \text{ km/s/Mpc})^2} = \omega_r \left(\frac{a_0}{a} \right)^4 + \omega_m \left(\frac{a_0}{a} \right)^3 + \omega_k \left(\frac{a_0}{a} \right)^2 + \omega_{\Lambda}. \quad (1.12)$$

Assuming only one dominant component, one can insert Eq. (1.8) into Eq. (1.10) to obtain:

$$a(t) = \begin{cases} a_0 t^{\frac{2}{3(1+w)}} & \text{for } w \neq -1, \\ a_0 e^{\sqrt{\frac{\Lambda}{3}} t} & \text{for } w = -1. \end{cases} \quad (1.13)$$

Instead of expressing the evolution of the Universe in terms of the time, t , or the scale factor, a , it is common to introduce the *redshift*

$$1 + z := \frac{a_0}{a}. \quad (1.14)$$

The redshift describes the relative change in wavelength of a photon that was emitted at scale factor a and detected today, a_0 . We will from now on set $a_0 = 1$. In terms of redshift, Eq. (1.12) becomes

$$\frac{H^2(z)}{(100 \text{ km/s/Mpc})^2} = \omega_r (1+z)^4 + \omega_m (1+z)^3 + \omega_k (1+z)^2 + \omega_{\Lambda}. \quad (1.15)$$

Since observations prefer a flat Universe, the curvature is often fixed to $k = 0$ (e.g. Aghanim *et al.*, 2020b). Assuming a flat Universe, $\omega_k = 0$, and taking into account that the energy density in radiation is negligible in the late Universe ($\omega_r \approx 0$), Eq. (1.15) becomes

$$\frac{H^2(z)}{(100 \text{ km/s/Mpc})^2} = \omega_m (1+z)^3 + \omega_{\Lambda} = \omega_m (1+z)^3 + h^2 - \omega_m, \quad (1.16)$$

where we used $\Omega_m + \Omega_{\Lambda} = 1$. It becomes evident that at late times $H(z)$ for fixed redshift, z , is a function of $\omega_m = \omega_d + \omega_b$, and h only.

1.3 Distances in an expanding Universe

In an expanding Universe, the ‘distance’ between two objects, e.g. two galaxies, becomes an ambiguous term. In this Section, we will review three commonly used distances.

The comoving distance

The comoving distance, χ , is the distance in a coordinate grid that expands with the Universe. Hence, the physical distance, r_p , at a given scale factor, a , is related to the comoving distance, χ , via

$$r_p(t) = a(t) \chi(t). \quad (1.17)$$

To derive an expression for $\chi(t)$, consider a photon that moves at the speed of light c . An infinitesimal light travel-time interval is related to the comoving distance via: $dt = \frac{dr_p(t)}{c} = \frac{a(t)}{c} d\chi$. Hence, the comoving distance can be expressed as

$$\chi(t) = c \int_t^{t_0} \frac{dt'}{a(t')} = \int_0^{z(t)} \frac{c dz'}{H(z')}, \quad (1.18)$$

where we changed variables via $\frac{dz}{dt} = -\frac{a_0}{a(t)^2} \dot{a}(t) = -a_0 \frac{H(t)}{a(t)} \implies \frac{dz}{a_0 H(z)} = -\frac{dt}{a(t)}$ and set $a_0 = 1$. For small redshifts, Eq. (1.18) can be approximated as

$$\chi = \frac{cz}{H_0} \implies cz = \chi H_0, \quad (1.19)$$

which represents the famous linear *Hubble-Lemâitre law*: “redshift \sim distance \times Hubble constant”. The linear relation breaks down at higher redshifts, where also higher order terms need to be taken into account.

The angular diameter distance

One possibility to define distances in an expanding Universe is to require that the following relation holds between the opening angle, θ , the proper size, s , and the distance, D_A , to an object:

$$\theta = \frac{s}{D_A}. \quad (1.20)$$

The distance D_A is called the (physical) *angular diameter distance* and ensures that the familiar relation between angle and distances (1.20) holds (in the small-angle approximation, which is usually a good approximation since angles are typically small in astronomy). To derive an equation for D_A , note that the proper size, s , of the object can also be expressed as $s = \chi(t) \theta \cdot a(t)$, where $\chi(t) \theta$ corresponds to the comoving size of the object. Hence, the angular diameter distance takes on the form

$$D_A(t) = a(t) \chi(t) = \frac{c}{1+z(t)} \int_0^{z(t)} \frac{dz'}{H(z')}. \quad (1.21)$$

The luminosity distance

The *luminosity distance*, D_L , is defined such that the familiar relation between flux, F , of a source with luminosity, L , holds:

$$F = \frac{L}{4\pi D_L^2}. \quad (1.22)$$

Since the Universe is expanding, it holds that $F = \frac{L a^2}{4\pi \chi^2(a)}$, where the additional factor of a^2 comes from the fact that the expansion of the Universe leads to a dilution of photons ($\times a$) and to an increase in wavelength ($\times a$). Hence, the luminosity distance is given by:

$$D_L(t) = \frac{\chi(t)}{a(t)} = [1 + z(t)] \int_0^{z(t)} \frac{c dz'}{H(z')}. \quad (1.23)$$

We will set the speed of light to unity, $c = 1$, from now on.

1.4 Inflation

Inflation is a phase of rapid expansion in the very early Universe, which was proposed in order to resolve the *horizon problem*². The horizon problem refers to the puzzling observation that the Universe is homogeneous and isotropic on large scales – scales much larger than could have been in causal contact in the early Universe. The isotropy is impressively demonstrated by the almost perfectly uniform temperature of the cosmic microwave background (see Sec. 1.5.1). The idea of inflation is to introduce a phase of accelerated expansion, which leads to a decreasing *Hubble radius* $\frac{1}{aH}$. The requirement of a decreasing Hubble radius, $\frac{d}{dt} \frac{1}{aH} = -\frac{\ddot{a}}{a^2} < 0$, translates into the requirement for an accelerated expansion of the Universe $\ddot{a} > 0$. Since the temporal derivative of Eq. (1.13) gives $\ddot{a}(t) \sim \frac{2}{3(1+w)} \left(\frac{2}{3(1+w)} - 1 \right) t^{\frac{2}{3(1+w)} - 2}$, the equation-of-state parameter during inflation has to be:

$$w_\phi < -\frac{1}{3}. \quad (1.24)$$

This means that inflation needs to be driven by an exotic energy component with negative pressure. The simplest model of inflation consists of a single scalar field, ϕ , known as the *inflaton*. In the following, we will review the dynamics of a scalar field in general, which will also be relevant for the Early Dark Energy model, which – in the simplest case – consists of a single scalar field (see Chapter 2).

²Inflation is usually not considered part of the standard cosmological model but rather sets the initial conditions for the standard cosmological model. We will still discuss it here briefly.

1.4.1 Dynamics of a scalar field in an expanding Universe

The action of a scalar field, ϕ , minimally coupled to the metric, $g^{\mu\nu}$, reads

$$\mathcal{S}_\phi = \int d^4x \sqrt{|\det(g)|} \left[-\frac{1}{2} g^{\mu\nu} \partial_\mu \phi \partial_\nu \phi - V(\phi) \right]. \quad (1.25)$$

The first term in square brackets is the kinetic term, the second term is the potential term with generic potential $V(\phi)$. One can compute the background energy-momentum tensor of the scalar field by

$$T_{\mu\nu} = \partial_\mu \phi \partial_\nu \phi - g_{\mu\nu} \left(\frac{1}{2} g^{\alpha\beta} \partial_\alpha \phi \partial_\beta \phi - V(\phi) \right) = \frac{\dot{\phi}^2}{2} \delta_\mu^0 \delta_\nu^0 + \left[\frac{\dot{\phi}^2}{2} - V(\phi) \right] g_{\mu\nu}, \quad (1.26)$$

where we assume ϕ to be homogeneous and that spatial derivatives vanish in the homogeneous and isotropic background. By comparing Eq. (1.26) to the energy momentum tensor of the perfect fluid in the background, $T_{\mu\nu} = (\rho + p) \delta_\mu^0 \delta_\nu^0 + p g_{\mu\nu}$, one can read off the energy density and pressure of the scalar field

$$\rho_\phi = \frac{\dot{\phi}^2}{2} + V(\phi), \quad p_\phi = \frac{\dot{\phi}^2}{2} - V(\phi). \quad (1.27)$$

Inserting Eqs. (1.27) into the first Friedmann equation (1.7) and the continuity equation (1.4) (for $k = 0$, $\Lambda = 0$) yields

$$H^2 = \frac{8\pi G_N}{3} \left(\frac{\dot{\phi}^2}{2} + V(\phi) \right), \quad (1.28a)$$

$$\ddot{\phi} + 3H\dot{\phi} + \frac{dV}{d\phi} = 0. \quad (1.28b)$$

Eq. (1.28b) is the Klein-Gordon equation for a scalar field in an expanding space, where the second term ($3H\dot{\phi}$) is the Hubble-drag term and the third term ($\frac{1}{2}dV/d\phi$) is the potential-gradient term.

Properties of the inflaton

Returning to the requirement that the scalar field that drives inflation needs to satisfy Eq. (1.24), one can easily read off the *slow-roll condition* from Eqs. (1.27):

$$V(\phi) \gg \dot{\phi}^2, \quad (1.29)$$

which ensures that $w_\phi = \rho_\phi/p_\phi \sim -1$. It is still an active field of research to understand how inflation ended and how the postulated inflaton field should decay into the species of the Λ CDM model.

Inflation does not only solve the horizon problem and other problems, e.g. the flatness problem, which is concerned with the fact that the Universe has zero curvature to very high precision, but inflation can also explain the origin of cosmic structure formation: inflation predicts the properties of the initial conditions for the density fluctuations, which have been confirmed observationally. This is the topic of the next section.

1.4.2 Cosmological perturbation theory

The Cosmological Principle states that the Universe is homogeneous and isotropic on large scales. However, there are density fluctuations on smaller scales, which can be observed as e.g. galaxies and galaxy clusters today. One approach to describe small fluctuations in a homogeneous background is *perturbation theory*. The derivations are beyond the scope of this thesis and we will only quote a few important results focusing on the intuitive picture (for a complete treatment, see e.g. Mukhanov, 2005; Weinberg, 2008; Dodelson and Schmidt, 2020). The metric, $g_{\mu\nu}$ and the energy-momentum tensor, $T_{\mu\nu}$, are described by a homogeneous and isotropic background (marked by a bar) plus perturbations, which are small compared to the background (δ):

$$g_{\mu\nu} = \bar{g}_{\mu\nu} + \delta g_{\mu\nu}, \quad (1.30a)$$

$$T_{\mu\nu} = \bar{T}_{\mu\nu} + \delta T_{\mu\nu}. \quad (1.30b)$$

To derive the perturbations of the line element $ds^2 = g_{\mu\nu}dx^\mu dx^\nu$, one writes down all possible terms and applies a scalar-vector-tensor decomposition, where at linear order, the equations of motion for scalar, vector and tensor perturbations decouple. One can show that the vector degrees of freedom are suppressed by the expansion of the Universe. The tensor metric perturbations are *primordial gravitational waves*. Here, we will only quote the scalar perturbations to the metric:

$$ds^2|_{\text{scalar}} = a^2(\eta) \left[-(1 - 2\phi)d\eta^2 + 2(\partial_a B)dx^a d\eta + ((1 + 2\psi)\delta_{ab} + 2\partial_{\langle a}\partial_{b\rangle}\epsilon) dx^a dx^b \right], \quad (1.31)$$

where $\partial_{\langle a}\partial_{b\rangle} := \partial_a\partial_b - \frac{1}{3}\delta_{ab}$ and $\eta = \int \frac{dt}{a(t)}$ is the conformal time. The four scalar perturbations of the metric are³: ϕ , B , ψ , ϵ .

The same can be done for the energy-momentum tensor of the perfect fluid:

$$\delta T_\nu^{(\text{pf})\mu} = (\delta\rho + \delta p)\bar{u}^\mu\bar{u}_\nu + (\bar{\rho} + \bar{p})(\delta u^\mu\bar{u}_\nu + \delta u_\nu\bar{u}^\mu) + \delta p\delta_\nu^\mu + \pi_\nu^\mu, \quad (1.32)$$

where $\delta\rho$ is the density perturbation, δp the pressure perturbation, $u_\mu = dx/dt = \bar{u}_\mu + \delta u_\mu$ is the comoving four velocity of the fluid, and π_ν^μ is the anisotropic stress. By inserting the metric perturbations, one can compute $\delta u_\mu = a(\phi - 1, \partial_a B + \nu_a)$, where ν_a is the velocity perturbation. A scalar-vector decomposition of the velocity perturbation yields $\nu_a = \partial_a\nu + v_a$, where $\partial_a v^a = 0$. Hence, we are left with three scalar perturbations of the energy-momentum tensor: δ_ρ , δ_p , ν .

These perturbations are not invariant under *gauge transformations*, i.e. diffeomorphisms or coordinate transformations of the form $x^\mu \rightarrow x^\mu + \delta x^\mu$. In order to describe physical processes it is necessary to express them in terms of *gauge-invariant parameters*, which are constructed in such a way that the gauge-transformation effects cancel up to linear order in perturbation theory. Examples for gauge-invariant parameters are the comoving curvature perturbation or Mukhanov-Sasaki variable (Mukhanov *et al.*, 1992; Sasaki, 1986) or the Bardeen potentials (Bardeen, 1980). The scalar perturbations are most commonly parameterized by the comoving curvature perturbation:

$$\mathcal{R} = \psi - \frac{\Delta}{3}\epsilon + \dot{a}(B + \nu), \quad (1.33)$$

³Note that ϕ is not the inflaton field in this section.

which has the advantage that it is frozen on scales larger than the Hubble radius. To relate perturbations to observations, one needs to quantize the perturbations, e.g. parameterized by \mathcal{R} , and compute the two-point correlation function $\langle \mathcal{R}(\mathbf{k}) \mathcal{R}^*(\mathbf{k}') \rangle$. Another procedure that is adopted to solve the gauge problem is to fix the gauge to eliminate spurious degrees of freedom present in the perturbations. There are many gauges in the literature that fix different quantities like the Newtonian gauge ($B = 0, \epsilon = 0$), the synchronous gauge ($\phi = 0, B = 0$), the spatially-flat gauge ($\epsilon = 0, \psi = 0$), and others. Each gauge has different advantages like making the physics be simple and apparent (e.g. Newtonian gauge) or to simplify calculations. Therefore, a procedure to study cosmological observations is to choose a gauge in which to perform calculations and then express the result in terms of gauge-invariant variables.

Since inflation puts the entire universe in causal contact at early times, the seeds for the structures we see today could have originated from quantum fluctuations. These quantum fluctuations are then stretched during the inflationary period and grow until they become super-Hubble, when they don't change their wavelength anymore (they 'freeze'). The curvature perturbation, \mathcal{R} , is conserved on super-horizon scales and its value does not change from the value it had when crossing the Hubble radius during inflation until it re-enters the horizon. Once inflation ends, the inflaton decays into the different species of the Λ CDM model (dark matter, baryons, radiation) and the smaller scales start to re-enter the horizon. These perturbations, which were created as quantum fluctuations in the early Universe, are the seeds for the growth of structure in the current Universe. *Single-field slow-roll inflation*, i.e. inflation with one scalar field, which rolls slowly down a potential in order for inflation to last sufficiently long, makes three important quantitative predictions:

1. The density fluctuations are *adiabatic*, i.e. the fractional number density fluctuations are the same for all species:

$$\frac{\delta\rho}{\bar{\rho} + \bar{p}} = \frac{\delta\rho_I}{\bar{\rho}_I + \bar{p}_I}, \quad (1.34)$$

where I stands for dark matter, baryons, or radiation (dark energy is usually assumed to have no perturbations).

2. The amplitude of the density fluctuations follows a *Gaussian* distribution with mean zero, i.e. $\langle \mathcal{R}(k) \rangle = 0$, hence the full information is contained in the variance of the distribution, i.e. the two-point function (in Fourier space for two modes, k and k'):

$$\langle \mathcal{R}(\mathbf{k}) \mathcal{R}^*(\mathbf{k}') \rangle = P_{\mathcal{R}}(k) (2\pi)^3 \delta_D^{(3)}(\mathbf{k} - \mathbf{k}'), \quad (1.35)$$

where $P_{\mathcal{R}}$ is the *power spectrum* and $\delta_D^{(3)}$ is the 3-dimensional Dirac delta.

3. The power spectrum, $k^3 P_{\mathcal{R}}(k)$, of the perturbations is *nearly scale invariant* with spectral index $n_s \simeq 1$:

$$k^3 P_{\mathcal{R}}(k) = 2\pi^2 A_s \left(\frac{k}{k_p} \right)^{n_s - 1}, \quad (1.36)$$

where A_s is the amplitude. Both are typically used as free parameters of the Λ CDM model and determined by a fit to data, e.g. data from the cosmic microwave background. k_p is the pivot scale and is often fixed by convention to $k_p = 0.05 \text{ Mpc}^{-1}$.

All three properties of the density fluctuations have been confirmed observationally. While inflation sets the ‘initial conditions’ of the density fluctuations, the next section will be concerned with the evolution of the density fluctuations and the formation of cosmic structure.

1.5 Growth of structure

1.5.1 From inflation to the cosmic microwave background

After inflation ended, the inflaton is assumed to have decayed into the different components of the Universe: dark matter (DM), baryonic matter, and radiation (photons and neutrinos)⁴. This process is known as *reheating*. All matter in the early Universe was in an extremely hot and dense state, so hot that baryons, photons and neutrinos were tightly coupled and too hot for the nucleons (protons and neutrons) to be bound into atoms. In the following we will sketch the history of the Universe from the radiation-dominated era until the emission of the cosmic microwave background, following Chapters 2 and 3 in Weinberg (2008).

While the Universe was expanding and cooling, certain interactions became less efficient once the interaction rate dropped below the expansion rate $H(z)$. When the temperature of the Universe dropped below $T = 10^{10} \text{ K}$, the conversion between protons and neutrons by weak interaction was not possible anymore in both directions but only in one direction ($n + \nu_e \rightarrow p + e^-$). Therefore, neutrinos decoupled from the baryon-photon plasma and free streamed since then. At a temperature of about $T = 10^9 \text{ K}$ *big bang nucleosynthesis* (BBN) started: protons and neutrons formed deuterium ($p + n \rightarrow d + \gamma$, where $d = {}^2\text{H}$), and then heavier nuclei ($d + d \rightarrow {}^3\text{H} + p$, $d + d \rightarrow {}^3\text{He} + n$, $d + {}^3\text{H} \rightarrow {}^4\text{He} + n$, and so on). At a temperature of $T = 10^4 \text{ K}$ the energy density of radiation fell below the energy density of (baryonic and dark) matter; this epoch is known as *matter-radiation equality*.

Once the temperature dropped below $T = 3000 \text{ K}$ – the Universe was only about 380,000 years old (Aghanim *et al.*, 2020b) at this time – electrons and nuclei started to form atoms. This moment is known as *recombination*. Once electrons were bound to atoms, the – until then opaque – Universe became transparent for photons. These photons, which free stream until today, constitute the *cosmic microwave background* (CMB). The CMB is a snapshot of the very early Universe – showing an almost perfectly isotropic black-body spectrum with temperature of about $T = 2.7 \text{ K}$. There are only tiny fluctuations of the order of $T = 10^{-5} \text{ K}$, demonstrating how homogeneous and isotropic the early Universe was. In Sec. 2.2.1, we will describe how a measurement of the CMB can constrain the composition of the Universe and its current expansion

⁴Dark energy only becomes important at later times and is usually modelled as a cosmological constant.

rate H_0 .

1.5.2 Boltzmann equations for linear perturbations

The components of the Universe (dark matter, baryons, photons, and neutrinos) are coupled: all components couple via gravity, photons and baryons couple via electromagnetic interaction, neutrinos and baryons couple via weak interaction, etc. Describing these components as a perfect fluid, i.e. in each point in spacetime all particles have the same momentum, is only in certain limits a good description. In practice, one needs to solve the *collisional Boltzmann* equation:

$$\frac{df}{dt}(t, \mathbf{x}, \mathbf{p}) = C[f], \quad (1.37)$$

where f is the phase-space distribution function, which describes the number density of particles with position \mathbf{x} and momentum \mathbf{p} at time t . The collision term, C , encodes all interactions between the different species. One typically solves the set of Boltzmann equations with numerical codes like CAMB (Lewis *et al.*, 2000) and CLASS (Blas *et al.*, 2011) in a fixed gauge (e.g. synchronous gauge) to obtain the matter power spectrum

$$\langle \delta(\mathbf{k}, t) \delta^*(\mathbf{k}', t) \rangle = (2\pi)^3 P(k, t) \delta_D^{(3)}(\mathbf{k} - \mathbf{k}'), \quad (1.38)$$

where $\delta(\mathbf{k}, t)$ are the relative density perturbations, also called *density contrast*, around a homogeneous and isotropic matter background $\bar{\rho}(t)$. Hence, the total matter density, $\rho(\mathbf{k}, t)$, can be written as:

$$\rho(\mathbf{k}, t) = \bar{\rho}(t) + \delta\rho(\mathbf{k}, t) = \bar{\rho}(t)[1 + \delta(\mathbf{k}, t)] \quad (1.39)$$

The Boltzmann equations are solved perturbatively up to linear order in density perturbations, δ , to obtain the linear power spectrum, P_{lin} . The linear power spectrum describes the density fluctuations observed in the cosmic microwave background already very well.⁵ However, once the Universe grows older, the density fluctuations become more and more non-linear. The reason behind this is that gravitational collapse leads to very non-linear structures like galaxies. Describing the cosmic web of dark matter and galaxies today, requires considering non-linear perturbations.

In the following, we will distinguish between linear and non-linear scales. The transition between them happens at the non-linear scale, which is often defined as the scale at which the dimensionless matter power spectrum $k^3 P_{\text{lin}}(k)/(2\pi^2)$ becomes of order unity, which is at about $k_{\text{NL}} = 0.25 h/\text{Mpc}$ at $z = 0$ (c.f. Desjacques *et al.*, 2018). Linear scales, $k \gg k_{\text{NL}}$, are well described by linear perturbation theory while non-linear scales, $k \ll k_{\text{NL}}$, are difficult to model analytically. Scales around k_{NL} are often referred to as mildly non-linear scales, which can be described with the tools of the next section.

⁵To determine the cosmological parameters, one typically models non-linear corrections based on the halo model (e.g. Smith *et al.*, 2003), which we will not discuss here.

1.5.3 Non-linear growth: one-loop perturbation theory

In order to describe the non-linearities of the large-scale structure (LSS), it is unavoidable to go to higher orders in perturbation theory. Standard perturbation theory computes higher order perturbative corrections, so-called *loop corrections*, iteratively assuming a fluid description of dark and baryonic matter (Zel'dovich, 1970; Goroff *et al.*, 1986; Jain and Bertschinger, 1994; Scoccimarro and Frieman, 1996a,b).

The idea behind next-to-leading order perturbation theory is to solve the fluid equations iteratively assuming knowledge of the linear matter power spectrum, P_{lin} (which can be obtained from Boltzmann solvers, see Sec. 1.5.2). The following is based on Goroff *et al.* (1986); Jeong and Komatsu (2006). As the power spectrum, $P(k, t)$, is a quadratic quantity of the density contrast in Fourier space, $\delta(\mathbf{k}, t)$ (see Eq. 1.38), the 3rd-order expansion in the density contrast is necessary for obtaining the next-to-leading order correction to $P(k, t)$. We are considering scales, which are large enough such that dark matter and baryons can be treated as a pressureless fluid. Since the peculiar velocities are much smaller than the speed of light and fluctuations are deep inside the horizon, i.e. $k \gg aH$, it is a good approximation to treat the system as Newtonian. The equations for the density contrast, δ , that need to be solved in the following are:

$$\dot{\delta} + \frac{1}{a} \nabla[(1 + \delta)\mathbf{v}] = 0 \quad (\text{continuity equation}), \quad (1.40)$$

$$\dot{\mathbf{v}} + \frac{1}{a} (\mathbf{v} \cdot \nabla) \mathbf{v} = -\frac{\dot{a}}{a} \mathbf{v} - \nabla \phi \quad (\text{Euler equation}), \quad (1.41)$$

$$\Delta \phi = 4\pi G a \bar{\rho} \delta \quad (\text{Poisson equation}), \quad (1.42)$$

where $\mathbf{v} = a d\mathbf{x}/dt$ is the velocity perturbation (which is assumed to be curl free up to linear order), ϕ is Newton's potential (c.f. 1.31), ∇ is the gradient/divergence with respect to comoving coordinates, and $\bar{\rho}$ is the background matter density. The fluid equations can be obtained by taking moments of the collisionless ($C = 0$) Boltzmann equation (1.37), also known as the Vlasov equation (see e.g. Baldauf, 2020). For the Fourier transform, we use the convention:

$$\delta(\mathbf{x}, t) = \int \frac{d^3k}{(2\pi)^3} e^{-i\mathbf{k}\cdot\mathbf{x}} \delta(\mathbf{k}, t). \quad (1.43)$$

Defining the velocity divergence field $\theta := \nabla \cdot \mathbf{v} \implies \theta(\mathbf{k}) = -i\mathbf{k} \cdot \mathbf{v}(\mathbf{k})$ and Fourier transforming the continuity and Euler equation, one finds

$$\dot{\delta}(\mathbf{k}, t) + \frac{1}{a} \theta(\mathbf{k}, t) = -\frac{1}{a} \int \frac{d^3k_1}{(2\pi)^3} \int d^3k_2 \delta_K^{(3)}(\mathbf{k}_1 + \mathbf{k}_2 - \mathbf{k}) \frac{\mathbf{k} \cdot \mathbf{k}_1}{k_1^2} \delta(\mathbf{k}_2, t) \theta(\mathbf{k}_1, t) \quad (1.44)$$

and similarly for θ . One can solve these equations iteratively following the steps:

- 1a) Linearize equations (1.40) - (1.42), i.e. keep only terms linear in δ , \mathbf{v} , and ϕ .

- 1b) Insert the ansatz $\delta_1(\mathbf{x}, t) = \epsilon_1(\mathbf{x})t^{n_1}$ into the linearized equations from 1a and keep only the solutions with leading time dependence. This approximation, which assumes scale-independent growth, is usually a good approximation for matter. Massive neutrinos, however, show a scale-dependent growth and would violate this assumption.
- 2a) Linearize the equations (1.40) - (1.42) around the solution obtained in 1b up to second order in the perturbations.
- 2b) Insert the ansatz $\delta_2(\mathbf{x}, t) = \epsilon_2(\mathbf{x})t^{n_2}$ into the second-order equations from 2a and keep only the solutions with leading time dependence.
- 3a) Linearize the equations (1.40) - (1.42) around the solution obtained in 2b up to third order in the perturbations.
- 3b) Insert the ansatz $\delta_3(\mathbf{x}, t) = \epsilon_3(\mathbf{x})t^{n_3}$ into the third-order equations from 3a and keep only the solutions with leading time dependence.
- 4) Etc.

In the following, we will show explicitly how to obtain the one-loop power spectrum from **Step 1** to **3**.

Step 1a

The linearized form of the Eqs. (1.40) - (1.42) is

$$\dot{\delta}_1 + \frac{1}{a} \nabla \cdot \mathbf{v}_1 = 0, \quad (1.45)$$

$$\dot{\mathbf{v}}_1 = -\frac{\dot{a}}{a} \mathbf{v}_1 - \nabla \phi_1, \quad (1.46)$$

$$\Delta \phi_1 = 4\pi G a \bar{\rho} \delta_1, \quad (1.47)$$

where first-order linear perturbations are denoted by the index 1. Inserting Eq. (1.45) into $\nabla \cdot (1.46)$ gives

$$-a\ddot{\delta}_1 - \dot{a}\dot{\delta}_1 = \dot{a}\delta_1 - \Delta\phi_1.$$

Further inserting $\Delta\phi_1$ from Eq. (1.47), yields an equation for δ_1 :

$$\ddot{\delta}_1 + 2H\dot{\delta}_1 = 4\pi G \bar{\rho} \delta_1. \quad (1.48)$$

Assuming matter domination, $w = 0$, we can use Eq. (1.13) to infer $a(t) = a_0 t^{2/3}$ and $\dot{a} = \frac{2}{3} a_0 t^{-1/3}$ ($a_0 = 1$), as well as $H = \frac{2}{3} t^{-1}$. Inserting this into Eq. (1.48) gives a differential equation for $\delta_1(t)$:

$$\ddot{\delta}_1 + \frac{4}{3} t^{-1} \dot{\delta}_1 - \frac{2}{3} t^{-2} \delta_1 = 0. \quad (1.49)$$

Step 1b

Inserting the ansatz $\delta_1(\mathbf{x}, t) = \epsilon_1(\mathbf{x})t^{n_1}$ into (1.49) yields:

$$n_1(n_1 - 1)\epsilon_1(\mathbf{x})t^{n_1-2} + \frac{4}{3}t^{-1}n_1\epsilon_1(\mathbf{x})t^{n_1-1} - \frac{2}{3}t^{-2}\epsilon_1(\mathbf{x})t^{n_1} = 0,$$

which gives an equation for the index, $n_1^2 + \frac{1}{3}n_1 - \frac{2}{3} = 0$, which has two solutions: one growing mode ($n_1 = \frac{2}{3}$) and one decaying mode ($n_1 = -1$). Since we are only interested in growing perturbations, we discard the decaying mode and find for the density contrast up to linear order

$$\delta_1(\mathbf{x}, t) = \epsilon_1(\mathbf{x})t^{2/3} = a(t)\epsilon_1(\mathbf{x}). \quad (1.50)$$

Note that $\delta_1(\mathbf{x}, t) \sim a$ grows linearly with the scale factor, a . More general, one defines $\delta_1(\mathbf{x}, t) = \epsilon_1(\mathbf{x})D(t)$, where $D(t)$ is the *linear growth factor*. In matter domination is $D(t) = a(t)$. Eq. (1.45) then gives for the velocity perturbation up to linear order

$$\mathbf{v}_1(\mathbf{x}, t) = a\boldsymbol{\nu}_1(\mathbf{x})t^{-1/3}, \quad (1.51)$$

where $\boldsymbol{\nu}_1(\mathbf{x})$ is a function only of \mathbf{x} .

Step 2a

Now, we want to linearize Eqs. (1.40) - (1.42) around the solutions from **Step 1b**. For that, we make the ansatz

$$\delta(\mathbf{x}, t) = \delta_1(\mathbf{x}, t) + \delta_2(\mathbf{x}, t), \quad (1.52)$$

$$\mathbf{v}(\mathbf{x}, t) = \mathbf{v}_1(\mathbf{x}, t) + \mathbf{v}_2(\mathbf{x}, t). \quad (1.53)$$

Inserting this into Eqs. (1.40) - (1.42), and solving the resulting equations analogously to **Step 1a** gives an equation for $\delta_2(\mathbf{x}, t)$:

$$\ddot{\delta}_2 + 2H\dot{\delta}_2 - 4\pi G\bar{\rho}\delta_2 = -\nabla(\epsilon_1\boldsymbol{\nu}_1) \left(\frac{1}{3}t^{-2/3} + 2Ht^{1/3} \right) + \nabla[(\boldsymbol{\nu}_1 \cdot \nabla)\boldsymbol{\nu}_1]t^{-2/3}.$$

Step 2b

Inserting the ansatz $\delta_2(\mathbf{x}, t) = \epsilon_2(\mathbf{x}, t)t^{n_2}$ gives an equation for n_2 :

$$n_2^2 + \frac{1}{3}n_2 - \frac{2}{3} = \frac{t^{4/3-n_2}}{\epsilon_2} \left[-\frac{5}{3}\nabla(\epsilon_1\boldsymbol{\nu}_1) + \nabla((\boldsymbol{\nu}_1 \cdot \nabla)\boldsymbol{\nu}_1) \right],$$

which has the solution: $n_2 = \frac{4}{3}$ and with that

$$\delta_2(\mathbf{x}, t) = \epsilon_2(\mathbf{x})t^{4/3}, \quad (1.54)$$

$$\mathbf{v}_2(\mathbf{x}, t) = a\boldsymbol{\nu}(\mathbf{x})t^{1/3} \quad (1.55)$$

if ϵ_2 is given by $\epsilon_2(\mathbf{x}) = \frac{9}{14} \left[-\frac{5}{3} \nabla(\epsilon_1 \boldsymbol{\nu}_1) + \nabla((\boldsymbol{\nu}_1 \cdot \nabla) \boldsymbol{\nu}_1) \right]$. It turns out to be more convenient to express ϵ_2 in Fourier space:

$$\int \frac{d^3 k}{(2\pi)^3} e^{-i\mathbf{k} \cdot \mathbf{x}} \epsilon_2(\mathbf{x}) = \int \frac{d^3 k_1}{(2\pi)^3} \int \frac{d^3 k_2}{(2\pi)^3} \int d^3 k \delta^{(3)}(\mathbf{k}_1 + \mathbf{k}_2 - \mathbf{k}) F_2 \epsilon_1(\mathbf{k}_1) \epsilon_1(\mathbf{k}_2) e^{-i\mathbf{k} \cdot \mathbf{x}}, \quad (1.56)$$

where

$$F_2 = \frac{5}{7} + \frac{2}{7} \frac{(\mathbf{k}_1 \cdot \mathbf{k}_2)^2}{k_1^2 k_2^2} + \frac{1}{2} \mathbf{k}_1 \cdot \mathbf{k}_2 \left(\frac{1}{k_1^2} + \frac{1}{k_2^2} \right) \quad (1.57)$$

and hence

$$\epsilon_2(\mathbf{k}) = \int \frac{d^3 k_1}{(2\pi)^3} \int d^3 k_2 \delta^{(3)}(\mathbf{k}_1 + \mathbf{k}_2 - \mathbf{k}) \tilde{F}_2(\mathbf{k}_1, \mathbf{k}_2) \epsilon_1(\mathbf{k}_1) \epsilon_1(\mathbf{k}_2). \quad (1.58)$$

Step 3

In order to find $\delta_3(\mathbf{x}, t) = \epsilon_3(\mathbf{x}) t^{n_3}$, repeat **Step 2a** and **Step 2b**, and obtain:

$$\begin{aligned} F_3(\mathbf{k}_1, \mathbf{k}_2, \mathbf{k}_3) = & \frac{1}{18} \left[7 \frac{\mathbf{k}_1 \cdot (\mathbf{k}_1 + \mathbf{k}_2 + \mathbf{k}_3)}{k_1^2} F_2(\mathbf{k}_2, \mathbf{k}_3) + G_2(\mathbf{k}_2, \mathbf{k}_3) \frac{|\mathbf{k}_1 + \mathbf{k}_2|^2}{k_1^2 k_2^2} (\mathbf{k}_1 \cdot \mathbf{k}_2) \right] \\ & + \frac{G_2(\mathbf{k}_1, \mathbf{k}_2)}{18} \left[7 \frac{(\mathbf{k}_1 + \mathbf{k}_2) \cdot (\mathbf{k}_1 + \mathbf{k}_3)}{(|\mathbf{k}_1 + \mathbf{k}_2|^2)} + \frac{|\mathbf{k}_1 + \mathbf{k}_2 + \mathbf{k}_3|^2}{|\mathbf{k}_1 + \mathbf{k}_2|^2 k_3^2} (\mathbf{k}_1 + \mathbf{k}_2) \cdot \mathbf{k}_3 \right], \end{aligned} \quad (1.59)$$

where

$$G_2(\mathbf{k}_1, \mathbf{k}_2) = \frac{3}{7} + \frac{1}{2} \frac{\mathbf{k}_1 \cdot \mathbf{k}_2}{k_1 k_2} \left(\frac{k_2}{k_1} + \frac{k_1}{k_2} \right) + \frac{4}{7} \frac{(\mathbf{k}_1 \cdot \mathbf{k}_2)^2}{k_1^2 k_2^2}. \quad (1.60)$$

Calculating the power spectrum

In **Step 1** to **Step 3**, we found $\delta(\mathbf{k}, t) = \delta_1(\mathbf{k}, t) + \delta_2(\mathbf{k}, t) + \delta_3(\mathbf{k}, t)$ with (in Fourier space):

$$\delta_1(\mathbf{k}, t) = a \epsilon_1(\mathbf{k}), \quad (1.61)$$

$$\delta_2(\mathbf{k}, t) = a^2 \epsilon_2(\mathbf{k}) = \int \frac{d^3 q}{(2\pi)^3} F_2(\mathbf{q}, \mathbf{k} - \mathbf{q}) \delta_1(\mathbf{q}) \delta_1(\mathbf{k} - \mathbf{q}), \quad (1.62)$$

$$\delta_3(\mathbf{k}, t) = a^3 \epsilon_3(\mathbf{k}) = \int \frac{d^3 q_1}{(2\pi)^3} \int \frac{d^3 q_2}{(2\pi)^3} F_3(\mathbf{q}_1, \mathbf{q}_2, \mathbf{k} - \mathbf{q}_1 - \mathbf{q}_2) \delta_1(\mathbf{q}_1) \delta_1(\mathbf{q}_2) \delta_1(\mathbf{k} - \mathbf{q}_1 - \mathbf{q}_2), \quad (1.63)$$

where F_2 is given in Eq. (1.57), and F_3 in Eq. (1.59). The *one-loop power spectrum*, $P^{\text{one-loop}}(k, t)$, can then be computed by inserting $\delta_2(\mathbf{k}, t)$ and $\delta_3(\mathbf{k}, t)$ and expressing it in terms of P_{lin} :

$$P^{\text{one-loop}}(k, t) = \int \frac{d^3 k'}{(2\pi)^3} \langle \delta(\mathbf{k}, t) \delta(\mathbf{k}', t) \rangle = P_{11}(k, t) + P_{22}(k, t) + 2P_{13}(k, t), \quad (1.64)$$

where

$$\begin{aligned}
P_{11}(k) &= P_{\text{lin}}(k), \\
P_{22}(k) &= 2 \int \frac{d^3q}{(2\pi)^3} P_{11}(q) P_{11}(|\mathbf{k} - \mathbf{q}|) (F_2(\mathbf{q}, \mathbf{k} - \mathbf{q}))^2, \\
P_{13}(k) &= 2 \int \frac{d^3q}{(2\pi)^3} P_{11}(k) [F_3(\mathbf{k}, \mathbf{q}, -\mathbf{q}) P_{11} + F_3(\mathbf{q}, \mathbf{k}, -\mathbf{q}) P_{11}(q) + F_3(\mathbf{q}, -\mathbf{q}, \mathbf{k}) P_{11}(q)].
\end{aligned} \tag{1.65}$$

Since $\delta_1(\mathbf{k}, t)$ is Gaussian (see Sec. 1.4.2), P_{12} vanishes.

Eqs. (1.64) and (1.65) are the main results of this section. Given a linear matter power spectrum P_{lin} (which can be obtained using Boltzmann solvers, see Sec. 1.5.2), one can solve the integrals for P_{22} and P_{13} numerically⁶ and obtain the one-loop matter power spectrum, i.e. the power spectrum until fourth order in density perturbations δ . The one-loop power spectrum can be used as a starting point to analyse galaxy clustering data.

1.5.4 Redshift space distortions and Alcock-Paczyński effect

In order to compare the matter power spectrum discussed in the previous sections to the galaxy power spectrum, which can be observed in galaxy surveys, one needs to take into account three further effects: the effect of *redshift space distortions*, the effect of *galaxy bias* and the effect of assuming the ‘wrong’ cosmology (*Alcock-Paczyński effect*). The goal of this section is to sketch the derivation of the linear power spectrum including these two effects. This section closely follows Dodelson and Schmidt (2020), their Ch. 11.

When observing galaxies in spectroscopic galaxy surveys, one cannot directly measure their (comoving) positions, \mathbf{x} , in real space (or wave vector, \mathbf{k} , in Fourier space). Galaxy clustering surveys typically measure the emission spectrum of a galaxy and determine the redshift z of the galaxy by identifying, e.g. spectral lines. Therefore, instead of the position, \mathbf{x} , in real space, we only have access to the redshift and position on the sky given by two angles: (z, θ, ϕ) . To convert angles and redshifts into real space, consider the comoving distance, χ (c.f. Eq. 1.18):

$$\mathbf{x}_{\text{obs}}(z, \theta, \phi) := \chi(z_{\text{obs}}) \hat{n} = \int \frac{dz_{\text{obs}}}{H_{\text{fid}}(z)} \hat{n}, \tag{1.66}$$

where $\hat{n} = \mathbf{x}_{\text{obs}}/|\mathbf{x}_{\text{obs}}|$ is the unit vector on the sphere of the sky. In order to use this conversion one needs to assume a fiducial cosmology (e.g. as constrained by *Planck* CMB data) to infer $H_{\text{fid}}(z)$. The tricky part, when converting galaxy redshift to distance, is that the observed redshift has two contributions, the expansion of the Universe and the peculiar velocity:

$$1 + z_{\text{obs}} = \frac{1}{a}(1 + u_{\parallel}), \tag{1.67}$$

⁶Although P_{22} looks simpler, there is a pole in the integral and one needs to calculate it numerically in two steps.

where $u_{\parallel} = \mathbf{v} \cdot \hat{n}$ is the peculiar velocity of the galaxy. The impact of the peculiar velocities on the observed density field is called *redshift space distortions* (RSD).

Furthermore, the fiducial cosmology could be different from the cosmology of the real Universe. Assuming only small deviations from the true cosmology, one can treat this difference perturbatively:

$$\chi_{\text{fid}}(z) = \chi(z) + \delta\chi(z), \quad (1.68)$$

$$H_{\text{fid}}(z) = H(z) + \delta H(z). \quad (1.69)$$

The impact of assuming a wrong cosmology ($\delta\chi \neq 0$, $\delta H \neq 0$) on the observed matter density field is known as the *Alcock-Paczyński effect* (AP effect).

In the following, we will sketch the derivation of the linear power spectrum including RSD and the AP effect. Expanding Eq. (1.66) in linear order in $\delta\chi$ and u_{\parallel} gives

$$\mathbf{x}_{\text{obs}} = \int \frac{dz}{H(z)} + \frac{1}{aH(z)} u_{\parallel} \hat{n} + \delta\chi(z) \hat{n} = \mathbf{x} + \left(\delta\chi(z) + \frac{u_{\parallel}}{aH} \right) \hat{n}. \quad (1.70)$$

In order to find an expression for the observed density contrast, $\delta_{g,\text{obs}}$, of galaxies, consider that the total number of galaxies needs to be the same in the observed coordinate system, \mathbf{x}_{obs} , and the real-space coordinate system, \mathbf{x} :

$$n_{g,\text{obs}}(\mathbf{x}_{\text{obs}}) d^3x_{\text{obs}} = n_g(\mathbf{x}) d^3x. \quad (1.71)$$

To change between the two coordinate systems, one needs to compute the Jacobian (up to linear order). Converting to polar coordinates with $d^3x = r^2 dr d\Omega$, where r is the comoving radial distance from a spacetime point, one finds:

$$J := \left| \frac{d^3x}{d^3x_{\text{obs}}} \right| = \underbrace{\left[1 + H^{-1} \delta H - 2 \frac{\delta\chi}{\chi} - 2 \frac{u_{\parallel}}{aHr} \right]}_{=:\bar{J}} \left(1 - \frac{1}{aH} \frac{\partial u_{\parallel}}{\partial r} \right), \quad (1.72)$$

where the last term in the square bracket can be neglected since $\frac{u_{\parallel}}{aH} \ll x$. Inserting this into Eq. (1.71) and assuming linear perturbations, δ , around a homogeneous background, \bar{n} , of galaxies, $n_g = \bar{n}_g(1 + \delta_g)$ and $n_{g,\text{obs}} = \bar{n}_g(1 + \delta_{g,\text{obs}})$, gives (up to linear order):

$$1 + \delta_{g,\text{obs}}(\mathbf{x}_{\text{obs}}) = J(1 + \delta_g(\mathbf{x})) = \bar{J} \left[1 + \underbrace{\delta_g(\mathbf{x}) - \frac{1}{aH} \frac{\partial u_{\parallel}}{\partial r}}_{\delta_{g,\text{RSD}}} \right]. \quad (1.73)$$

Since in surveys, we observe galaxies, δ_g , rather than the total matter density field, δ_m , we need to assume a relation between them. Here, we will simply assume a *linear bias relation*, which is accurate at large scales:

$$\delta_g(\mathbf{x}) = b_1 \delta_m(\mathbf{x}). \quad (1.74)$$

We now want to express δ_g in Fourier space in order to compute the power spectrum later. Inserting Eq. (1.74) and Fourier-transforming $\delta_{g,\text{RSD}}$, yields

$$\begin{aligned}\delta_{g,\text{RSD}}(\mathbf{k}) &= \int d^3x e^{-i\mathbf{k}\cdot\mathbf{x}} \left(b_1 \delta_m(\mathbf{x}) - \frac{1}{aH} \frac{\partial}{\partial r} \int \frac{d^3k'}{(2\pi)^3} e^{i\mathbf{k}'\cdot\mathbf{x}'} u_{\parallel}(\mathbf{k}') \right) \\ &= b_1 \delta_m(\mathbf{k}) + f(\hat{k} \cdot \hat{e}_{\text{LOS}})^2 \delta_m(\mathbf{k}) \\ &= [b_1 + f\mu^2] \delta_m(\mathbf{k}),\end{aligned}\tag{1.75}$$

where $\mu_k = \hat{e}_{\text{LOS}} \cdot \hat{k}$ is the angle between the unit k -vector, $\hat{k} = \mathbf{k}/k$, and the line of sight, \hat{e}_{LOS} . We used that the velocity perturbation, $u_{\parallel} = aH f \frac{i\mathbf{k}}{k^2} \delta(k)$, can be expressed in terms of the linear growth rate, $f = \frac{d \ln(D)}{d \ln(a)}$, where D is the linear growth factor (see Eq. 1.50). Note that Eq. (1.75) only includes RSD, no AP effect. Inserting this into Eq. (1.73), gives

$$\delta_{g,\text{obs}}(\mathbf{k}_{\text{obs}}) = \bar{J} \delta_{g,\text{RSD}}(\mathbf{k}_{\text{obs}}) = \delta_{g,\text{RSD}}(\mathbf{k}[\mathbf{k}_{\text{obs}}]),\tag{1.76}$$

with $\mathbf{k}[\mathbf{k}_{\text{obs}}] = ([1 + \alpha_{\parallel}] k_{\text{obs}}^1, [1 + \alpha_{\parallel}] k_{\text{obs}}^2, [1 + \alpha_{\perp}] k_{\text{obs}}^3)$, where

$$\alpha_{\parallel} = \frac{\delta\chi}{\chi_{\text{fid}}} \quad \text{and} \quad \alpha_{\perp} = \frac{\delta H}{H_{\text{fid}}}.\tag{1.77}$$

With that, the observed galaxy density contrast, $\delta_{g,\text{obs}}$, as a function of the observed wave vector, \mathbf{k}_{obs} , can be expressed in terms of the true matter density field as a function of the Fourier space wave vector, \mathbf{k} :

$$\delta_{g,\text{obs}}(\mathbf{k}_{\text{obs}}) = [b_1 + f\mu_k^2] \delta_m(\mathbf{k})|_{\mathbf{k}=\mathbf{k}[\mathbf{k}_{\text{obs}}]}.\tag{1.78}$$

Finally, this can be inserted into the power spectrum:

$$P_{g,\text{obs}}(\mathbf{k}_{\text{obs}}, z) = P_{\text{lin}}(k, z) [b_1 + f\mu_k^2]^2 \Big|_{\mathbf{k}=\mathbf{k}[\mathbf{k}_{\text{obs}}]}.\tag{1.79}$$

This equation is known as the *Kaiser formula*. It is linear in gravitational clustering, in galaxy bias and in redshift-space distortions. This is only a good approximation at large scales. There are several approaches to include non-linearities in all of these aspects, e.g. Taruya *et al.* (2010) also take into account non-linear gravitational clustering and non-linear redshift-space distortions and find approximations for the power spectrum. Another approach to model the mildly non-linear scales is the effective field theory of LSS, which is described in the next section.

1.5.5 Effective field theory of large scale structure

The standard one-loop perturbative approach discussed in Sec. (1.5.3) works very well on mildly non-linear scales ($k \leq 0.5h/\text{Mpc}$) at high redshift ($z > 1$), when non-linearities are still small (Jeong and Komatsu, 2006). However, at low redshifts ($z \approx 0$) the perturbative approach breaks down at mildly non-linear scales ($k \approx 0.1h/\text{Mpc}$): even when adding higher-order perturbative

terms, the analytic prediction does not approach the ‘true’ power spectrum (as obtained from N-body simulations). Additionally, there is no good expansion parameter at small scales since the density fluctuations δ can be much larger than unity. This leads to the problem that there is no good notion of convergence in cosmological perturbation theory. Furthermore, some of the integrals discussed in Sec. 1.5.3 do not converge for certain initial power spectra. The reason behind these problems is that the pressureless ideal-fluid approximation is not a good description of dark matter on (mildly) non-linear scales since effects like shell crossing can take place on smaller scales. Strictly speaking the integrals over k from 0 to ∞ appearing in one-loop perturbation theory are not even well defined since we are lacking understanding of the short-scale physics ($k \rightarrow \infty$), which includes the non-fluidity of dark matter.

The effective field theory (EFT) of LSS (Baumann *et al.*, 2012; Carrasco *et al.*, 2012, 2014) aims to solve these problems by introducing a cutoff or smoothing scale⁷ Λ beyond which the perturbative approach, i.e. the ‘effective theory’, breaks down – much like EFT of particle physics. The physics of the unknown small-scale (ultraviolet, UV) physics beyond the cutoff Λ onto the larger scales will then be encoded in *counterterms*. The counterterms have a mathematical form informed from the EFT, however, their coefficients need to be determined from a fit to data. The such-constructed counterterms will absorb the back-reaction of the unknown small-scale physics on the larger mildly non-linear scales.

In the following we will closely follow the description in Baldauf (2020). We will split all quantities in large-scale and small-scale modes and infer the mathematical form of the counterterms. For that, we need to introduce the cutoff scale Λ (in k -space)⁸, above which the density field is smoothed with some kernel, e.g. a Gaussian kernel:

$$W_\Lambda(k) = e^{-\frac{1}{2} \frac{k^2}{\Lambda^2}}. \quad (1.80)$$

Given a phase-space distribution function (see Eq. 1.37) $f(\mathbf{x}, \mathbf{k}, t) = \sum_{i=1}^N f_i(\mathbf{x}, \mathbf{k}, t)$, where N is the total number of particles and $f_i(\mathbf{x}, \mathbf{k}) = \delta(\mathbf{x} - \mathbf{x}_i)\delta(\mathbf{k} - \mathbf{k}_i)$ is the distribution function of a single particle, one can define the smoothed matter and momentum densities as⁹

$$\rho_\Lambda(\mathbf{x}, t) = \frac{m}{a^3} \int d^3y \int d^3q W_\Lambda(|\mathbf{x} - \mathbf{y}|) f(\mathbf{y}, \mathbf{q}, t), \quad (1.81)$$

$$\pi_\Lambda(\mathbf{x}, t) = \frac{1}{a^4} \int d^3y \int d^3q \mathbf{q} W_\Lambda(|\mathbf{x} - \mathbf{y}|) f(\mathbf{y}, \mathbf{q}, t), \quad (1.82)$$

where $W_\Lambda(\mathbf{x})$ is the Fourier-transformed smoothing kernel. We can now apply the smoothing to the Euler (1.41) and continuity Eqs. (1.4) (or derive these equations by taking moments of the collisionless Boltzmann equation – but this times with the smoothed densities). We will split the density into a smoothed long-wavelength part and a short-wavelength part, e.g. $\rho(\mathbf{x}) = \rho_\Lambda(\mathbf{x}) + \rho_s(\mathbf{x})$ and $\mathbf{v}(\mathbf{x}) = \mathbf{v}_\Lambda(\mathbf{x}) + \mathbf{v}_s(\mathbf{x})$. Finally, we obtain the standard fluid equations but

⁷ Λ is not the cosmological constant in this section.

⁸The cutoff scale needs to be larger than the non-linear scale $k_{\text{NL}} \sim 0.25h/\text{Mpc}$.

⁹ \mathbf{x} and \mathbf{y} refer to comoving coordinates, \mathbf{k} is the comoving wave vector.

with additional terms (e.g. Baldauf, 2020):

$$\dot{\delta}_\Lambda + \frac{1}{a} \partial_j [(1 + \delta) v^j]_\Lambda = 0, \quad (1.83)$$

$$\dot{v}_\Lambda^i + \frac{1}{a} v_\Lambda^j \partial_j v_\Lambda^i + \frac{\dot{a}}{a} v_\Lambda^i + \partial^i \phi_\Lambda = -\frac{1}{\rho_\Lambda} \partial_j [\tau^{ij}]_\Lambda, \quad (1.84)$$

where $[\cdot]_\Lambda$ denotes smoothing with scale Λ . These additional terms, τ^{ij} , can be interpreted as an *effective stress tensor* of an imperfect fluid. The stress tensor is a function of the short-wavelength contributions:

$$\tau_{ij} = \rho v_s^i v_s^j - \frac{(\partial_k \phi_s)(\partial^k \phi_s) \delta_{ij} - 2(\partial_i \phi_s) \partial_j \phi_s}{8\pi G}. \quad (1.85)$$

Eq. (1.85) shows how two short modes, v_s or ϕ_s , can couple to a long mode giving a backreaction of the small scales onto the larger scales.

Since the short-scale physics are very difficult to model analytically, the approach of the EFT of LSS is to take expectation values over the short-wavelength fluctuations (in quantum field theory, this is called ‘integrating out the UV-degrees of freedom’). The expectation value can depend on all terms allowed by the equivalence principle at the given order in perturbations, in particular it can depend on the actual local amplitude of the long modes, e.g. by tidal effects. Therefore, we expand the effective stress tensor perturbatively around the homogeneous solution:

$$\langle [\tau^{ij}]_\Lambda \rangle_{\delta_l} = \underbrace{\langle [\tau^{ij}]_\Lambda \rangle_0}_{=p_b \delta_{ij} \text{ hom.+isotr.}} + \underbrace{\frac{\partial \langle [\tau^{ij}]_\Lambda \rangle_{\delta_l}}{\partial \delta_l}}_{=\rho_b c_s^2 \delta^{ij}} \delta_l + \underbrace{\frac{\partial \langle [\tau^{ij}]_\Lambda \rangle_{\delta_l}}{\partial (\partial_k v^k)}}_{=-\rho_b \frac{c_{bv}^2}{aH} \delta_{ij}} \partial_k v^k - \tau_{\text{visc},\Lambda}(v) + \Delta t^{ij}, \quad (1.86)$$

with $\tau_{\text{visc},\Lambda}(v) = \frac{3}{4} \rho_b \frac{c_{sv}^2}{aH} (\partial^j v_l^i + \partial^j v_l^i - \frac{2}{3} \delta^{ij} \partial_k v_l^k)$ being the shear viscosity term.

The coefficients p_b (effective pressure), c_s (sound speed), c_{bv} (bulk viscosity) and c_{sv} (shear viscosity) are determined by the UV physics. Hence, they are not predictable within the EFT and need to be fitted to data.

The new interaction term, $[\tau^{ij}]_\Lambda$, leads to a new term in the perturbative solution of the fluid equations at third order (see Sec. 1.5.3). The additional term is proportional to a pre-factor, \tilde{c}_s , and needs to be determined from a fit to data:

$$\delta(\mathbf{k}, t) = \delta^{(1)}(\mathbf{k}, t) + \delta^{(2)}(\mathbf{k}, t) + \delta^{(3)}(\mathbf{k}, t) - \tilde{c}_s^2 k^2 \delta^{(1)}(\mathbf{k}, t). \quad (1.87)$$

As a consequence, the one-loop matter power spectrum obtains an additional term as well:

$$P(k, t) = D^2(t) P_{11}(k) + D^4(t) [2P_{13}(k) + P_{22}(k)] - 2\tilde{c}_s^2 k^2 D^2(t) P_{11}(k), \quad (1.88)$$

The additional term in Eq. (1.88) is a *counterterm* with free coefficient \tilde{c}_s , which naturally emerged from introducing a smoothing scale and a split between long- and short-wavelength modes. Note that Eq. (1.88) is independent of the smoothing scale, Λ . This is due to the fact that the counterterm has the correct functional form to absorb the cutoff dependence (e.g. Baldauf *et al.*, 2015).

Hence, introducing the smoothing scale can be regarded as a method to find the mathematical form of the counterterm that describes the effect of the short-scale physics on the long-wavelength modes.

To describe the relation between matter and galaxy density contrast, EFT-of-LSS approaches typically use a non-linear galaxy bias expansion (for a review see Desjacques *et al.*, 2018), which reads up to third order:

$$\delta_g = b_1\delta + \frac{b_2}{2}\delta^2 + b_{G_2}G_2 + \frac{b_3}{6}\delta^3 + b_{\delta G_2}\delta G_2 + b_{G_3}G_3 + b_{\Gamma_3}\Gamma_3 + R_*^2\partial^2\delta. \quad (1.89)$$

where $G_2 \equiv G_2(\phi_g) = (\partial_i\partial_j\phi_g)^2 - (\partial_i^2\phi_g)^2$ is the so-called tidal-field operator and $\Gamma_3 = G_2(\phi_g) - G_2(\phi_v)$. This leads to additional free parameters ($b_1, b_2, b_{G_2}, b_{\delta G_2}, b_{G_3}, b_{\Gamma_3}, R_*^2$). When calculating the monopole, quadrupole and hexadecapole galaxy power spectrum (see below), one finds that four of these terms disappear or are degenerate with other terms. One ends up with¹⁰:

$$\delta_g = b_1\delta + \frac{b_2}{2}\delta^2 + b_{G_2}G_2 + b_{\Gamma_3}\Gamma_3, \quad (1.90)$$

When going over to redshift space and taking velocity bias into account, Eq. (1.88) acquires four counterterms in total (Senatore and Zaldarriaga, 2014; Lewandowski *et al.*, 2018; Perko *et al.*, 2016):

$$\begin{aligned} P_{\nabla^2\delta}^{\text{ctr}}(z, k, \mu) &= -2\tilde{c}_0(z)k^2P_{11}(z, k) - 2\tilde{c}_2(z)f(z)\mu^2k^2P_{11}(z, k) \\ &\quad - 2\tilde{c}_4(z)f^2(z)\mu^4k^2P_{11}(z, k), \\ P_{\nabla^4\delta}^{\text{ctr}}(z, k, \mu) &= -\tilde{c}(z)f^4(z)\mu^4k^4(b_1(z) + f(z)\mu^2)^2P_{11}, \end{aligned} \quad (1.91)$$

where the four coefficients $\tilde{c}_0, \tilde{c}_2, \tilde{c}_4$ and \tilde{c} appear. Note that the counterterm $P_{\nabla^4\delta}^{\text{ctr}}(z, k, \mu) \sim \tilde{c}$ is a two-loop counterterm. Since the 3-dimensional power spectrum in redshift space is anisotropic, one would lose information by considering only the *monopole* power spectrum, i.e. the power spectrum averaged over all angles on the sphere. Therefore, one typically expands the power spectrum $P(z, k, \mu)$ in terms of multipoles¹¹:

$$P_\ell(z, k) = \frac{2\ell + 1}{2} \int_{-1}^1 d\mu \mathcal{L}_\ell(\mu) P(z, k, \mu), \quad (1.92)$$

where \mathcal{L}_ℓ corresponds to the Legendre polynomial of order ℓ and $\mu = \hat{e}_{\text{LOS}} \cdot \mathbf{k}/k$ is the angle between the line of sight, \hat{e}_{LOS} , and the wave vector, \mathbf{k} . P_0 corresponds to the monopole, P_2 the quadrupole, and P_4 to the hexadecapole power spectra. One typically does not go higher in ℓ than the hexadecapole since higher order multipoles do not contain much cosmological information for current galaxy clustering surveys like BOSS due to the low signal-to-noise ratio. When calculating the multipoles of the power spectrum up to the hexadecapole, one finds that only the following combinations appear:

$$c_0 = \tilde{c}_0 + \frac{f}{3}\tilde{c}_2 + \frac{f^2}{5}\tilde{c}_4, \quad c_2 = \tilde{c}_2 + \frac{6f}{7}\tilde{c}_4, \quad c_4 = \tilde{c}_4. \quad (1.93)$$

¹⁰The term proportional to b_{Γ_3} is often assumed to be negligible.

¹¹Alternatively, $P(z, k, \mu)$ is often computed in bins of μ called ‘wedges’.

Finally, one also needs to take into account the stochastic power-spectrum contribution in redshift space, which at next-to-leading order has the following form:

$$P^{\text{ec}}(z, k, \mu) = P_{\text{shot}}(z) + a_0(z)k^2 + a_2(z)\mu^2k^2, \quad (1.94)$$

where P_{shot} , a_0 and a_2 are in principle free parameters¹². The $P_{\text{ctr,RSD},\nabla_z^4\delta}$ counterterm is approximately degenerate with the $a_2\mu^2k^2$ stochastic contribution in the galaxy power spectrum. Hence, we only keep $P_{\text{ctr,RSD},\nabla_z^4\delta}$. Furthermore, the a_0 contribution can be approximately neglected on scales $k \lesssim 0.3h/\text{Mpc}$. So we are only left with the free parameter P_{shot} .¹³

To summarize, the EFT model of the galaxy power spectrum in redshift space has the following form (Senatore and Zaldarriaga, 2014; Perko *et al.*, 2016; Chudaykin *et al.*, 2020):

$$P_{g,\text{RSD}}(z, k, \mu) = P_g^{\text{tree}}(z, k, \mu) + P_g^{1\text{-loop}}(z, k, \mu) + P_g^{\text{ec}}(z, k, \mu) + P_g^{\text{ctr}}(z, k, \mu), \quad (1.95)$$

where the tree-level and one-loop contributions to the power spectrum are given by

$$P_g^{\text{tree}}(z, k, \mu) = Z_1^2(\mathbf{k})P_{11}(z, k), \quad (1.96)$$

$$P_g^{1\text{-loop}}(z, k, \mu) = 2 \int d^3q Z_2^2(\mathbf{q}, \mathbf{k} - \mathbf{q})P_{11}(z, |\mathbf{k} - \mathbf{q}|)P_{11}(z, q) \quad (1.97)$$

$$+ 6Z_1(\mathbf{k})P_{11}(z, k) \int d^3q Z_3(\mathbf{q}, -\mathbf{q}, \mathbf{k})P_{11}(z, q),$$

where the kernels are $Z_1(\mathbf{k}) = b_1 + f\mu^2$, Z_2 and Z_3 , which depend on b_1 , b_2 , $b_{\mathcal{G}_2}$, b_{Γ_3} (their explicit form is given in Chudaykin *et al.*, 2020, their Eq. 2.14). The stochastic contribution P^{ec} is given in Eq. (1.94) and often simply modeled as scale-independent Poisson shot noise, i.e. $P^{\text{ec}}(z, k, \mu) = P_{\text{shot}}$. The counterterms $P_g^{\text{ctr}}(z, k, \mu) = P_{\nabla_z^2\delta}^{\text{ctr}}(z, k, \mu) + P_{\nabla_z^4\delta}^{\text{ctr}}(z, k, \mu)$ are given in Eqs. (1.91). That means, in total the EFT-of-LSS parametrization discussed in this section introduces nine free nuisance parameters:

- 4 bias coefficients: $b_1, b_2, b_{\mathcal{G}_2}, b_{\Gamma_3}$.
- 4 counter-term coefficients (in redshift space): c_0, c_2, c_4, \tilde{c} .
- 1 stochastic term: P_{shot} .

Note that this is not the only parametrization of the EFT. While this parametrization is called ‘east coast’ (EC, used in e.g. CLASS_PT, Chudaykin *et al.*, 2020) parametrization, there is a physically equivalent parametrization called ‘west coast’ (WC, used in pybird, D’Amico *et al.*, 2021a) parametrization (see Simon *et al.*, 2022, for a comparison of both parametrizations).

If one only includes monopole and quadrupole in the analysis, c_4 can be discarded and one ends up with eight nuisance parameters. These nuisance parameters cannot be predicted from

¹² a_0, a_2 are not related to the scale factor here.

¹³In more recent studies, scale-dependent shot noise is included, thereby increasing the number of nuisance parameters by two.

theory and need to be obtained from a fit to data. The EFT approach allows to include the full shape of the power spectrum into the analysis up to mildly non-linear scales. The lack of knowledge of the complicated small-scale physics is absorbed in the bias terms and counterterms. One small complication remains, which is the treatment of large-scale bulk flows, which will be discussed in the next subsection.

IR resummation

The *baryon acoustic oscillations* (BAO, see Sec. 2.2.1) are oscillations in the baryon-photon fluid of the primordial Universe, which leave an imprint in matter density and with that in the LSS of the Universe. The shape of the BAO peak is very sensitive to *bulk flows*, i.e. large-scale displacements that are induced by long-wavelength modes ('infrared modes'). The dominant effect of these bulk flows is a simple translation of matter, resulting in a broadening of the BAO peak. In BAO-only analyses, this broadening is undone by so-called BAO-reconstruction, which reverts the effect of gravity on the BAO signal. This sharpens the BAO but also introduces a distortion of the broadband power spectrum that is not easily removed. Therefore, for an analysis using the full shape of the power spectrum, it is more straight-forward to include the broadening of the BAO in the theory model. In Eulerian perturbation theory, bulk flows are usually treated perturbatively. However, due to the strong non-linearity of the effect, this is very inaccurate. Via a 'detour' to Lagrangian perturbation theory, it is possible to *resum* the perturbative expansion of the translation to an exponential prefactor. This so-called IR resummation gives an accurate non-perturbative treatment of the effect and at the same time does not introduce any new parameters (Senatore and Zaldarriaga, 2015; Baldauf *et al.*, 2015; Vlah *et al.*, 2016; Ivanov and Sibiryakov, 2018; Lewandowski *et al.*, 2018).

Chapter 2

The Hubble Tension and Early Dark Energy

This Chapter follows the recent reviews by Kamionkowski and Riess (2022); Poulin et al. (2023). Sec. 2.2.1 follows the Advanced Course of the International Max Planck Research School by Prof. Eiichiro Komatsu in 2020¹.

Summary: In this chapter, we will give an overview of different measurements of the Hubble constant, H_0 . These are commonly grouped into the indirect measurements (Sec. 2.2), which strongly depend on the assumption of a cosmological model, and the direct measurements (Sec. 2.3), which do not depend or depend only weakly on a cosmological model. In Sec. 2.4, we describe general properties that solutions to the Hubble tension should have, and in Sec. 2.5, we describe one workable solution called *Early Dark Energy* (EDE) and discuss constraints of the EDE model in the literature in Sec. 2.6.

¹<https://wwwmpa.mpa-garching.mpg.de/~komatsu/lectures--reviews.html>

2.1 The Hubble tension

The standard Λ CDM model discussed in Chapter 1 presents a remarkably good fit to all cosmological data sets. However, it comes at the cost of introducing several ingredients beyond the Standard Model of particle physics: dark matter, dark energy and inflation. The underlying micro-physics of these ingredients are still largely unknown and direct detection of the dark components have evaded all efforts so far. CDM and the cosmological constant, Λ , present an effective description, which can successfully describe observational data. One way forward is to look for evidence of a breakdown of this effective description in order to obtain new hints towards understanding the dark sector of the Universe.

During the last 10 years, several tensions have emerged, of which the *Hubble tension* is the most pressing tension (Knox and Millea, 2020; Bernal *et al.*, 2016; Kamionkowski and Riess, 2022; Poulin *et al.*, 2023). The Hubble tension is a discrepancy between different measurements of the current expansion rate of the Universe as defined in Eq. (1.6). It reaches 5σ between the *Planck* cosmic microwave background measurement (Aghanim *et al.*, 2020b, see Sec. 2.2.1), and the SHOES distance ladder measurement (Riess *et al.*, 2022, see Sec. 2.3.1). While the tension is most severe between these two experiments, there are several other experiments that infer H_0 from cosmological data and a very interesting picture emerges: Experiments, which measure H_0 *indirectly* by constraining the Universe at early times and assuming a cosmological model to predict H_0 (for example the *Planck* CMB measurement), favor lower values of $H_0 \sim 67$ km/s/Mpc. On the other hand, experiments that constrain H_0 *directly* without having to assume a cosmological model favor higher values of $H_0 \sim 73$ km/s/Mpc (for example the SHOES experiment). It transpires that the Hubble tension can be viewed as a tension between two classes of experiments, the *direct* and *indirect measurements*. If this tension is not caused by measurement systematics in one or several of the experiments, the tension could be a hint of new physics beyond the Λ CDM model.

In the following, we will begin by discussing a selection of the most constraining direct and indirect measurements of the Hubble constant, H_0 .

2.2 Indirect measurements of H_0

Indirect measurements of H_0 constrain the composition of the Universe at early times and need to assume a cosmological model in order to infer H_0 .

2.2.1 The cosmic microwave background

The *cosmic microwave background* (CMB, see Sec. 1.5.1), shows tiny fluctuations in photon temperature and polarization, which are best represented by the two-point correlation function

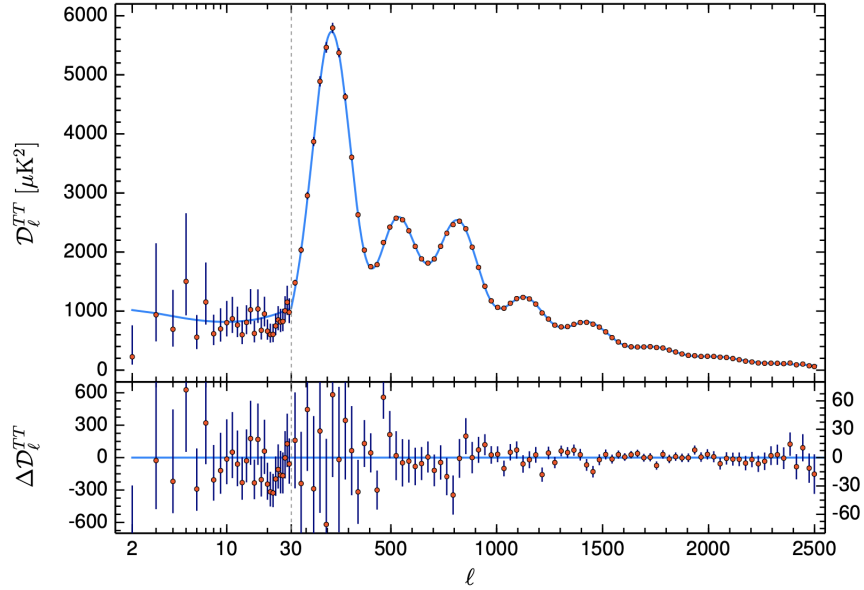


Figure 2.1: CMB temperature power spectrum as measured by *Planck* (red data points) and the Λ CDM model (blue line). The bottom panel shows the deviation of the data from the model. Taken from Aghanim *et al.* (2020b).

in Fourier space, i.e. the power spectrum, usually decomposed in spherical harmonics, C_ℓ or $D_\ell = \ell(\ell + 1)C_\ell/2\pi$ (see Fig. 2.1). The shape of the temperature and polarization power spectra can be accurately predicted for a given cosmological model, e.g. Λ CDM, with Boltzmann solvers (see Sec. 1.5.2). Fitting the theory prediction to the ‘full shape’ of the CMB power spectra gives accurate constraints on the cosmological parameters, e.g. the six Λ CDM parameters. To get an intuition for how the CMB constrains the cosmological parameters, in particular H_0 , it is instructive to look at the quantities that the CMB power spectra are most sensitive to. For the following discussion, we will assume flat ($\Omega_k = 0$) Λ CDM.

Baryon acoustic oscillations

The *baryon acoustic oscillations* (BAO) are the imprint of sound waves in the primordial baryon-photon fluid. They originate from density perturbations with gravity as a driving force while photon pressure provides the restoring force. Since the perturbations are small, they evolve linearly and each Fourier mode can be regarded separately. Once a given mode enters the horizon, it starts oscillating. While the peaks at high ℓ (small scales) in Fig. 2.1 entered the horizon earlier and underwent several oscillations, the first peak at $\ell \sim 300$ could only complete 1/4 of an oscillation, reaching maximal compression. Since the C_ℓ measure the variance of fluctuations, both under- and overdensities appear as peaks, where odd peaks correspond to maximal overdensities and even peaks to maximal underdensities.

Since the BAO have only a limited time to propagate in the baryon-photon plasma – from the hot Big Bang ($z = \infty$) until the time of recombination ($z = z_*$), they imprint a characteristic scale into the density field, the comoving *sound horizon*:

$$r_s = \int_{z_*}^{\infty} \frac{c_s(z)}{H(z)} dz, \quad (2.1)$$

where $c_s(z)$ is the sound speed of the waves in the baryon-photon plasma. Using the relations of an adiabatic and relativistic fluid (e.g. Dodelson and Schmidt, 2020, their Ch. 9), one can infer the sound speed ($c = 1$)

$$c_s(z) = \frac{1}{\sqrt{3(1 + R(z))}} \quad (2.2)$$

as a function of the baryon-to-photon ratio:

$$R(z) = \frac{3\omega_b}{4\omega_\gamma} \frac{1}{1 + z}. \quad (2.3)$$

The CMB can be used to precisely measure the *angular size of the sound horizon*:

$$\theta_s = \frac{a(z_*) r_s}{D_A(z_*)} = \frac{\int_{z_*}^{\infty} c_s(z) dz / H(z)}{\int_0^{z_*} dz / H(z)}, \quad (2.4)$$

where we inserted Eqs. (2.1) and (1.21). θ_s can be inferred from the frequency of the acoustic peaks in the CMB power spectrum and is measured with very high accuracy: $\theta_s = 1.04110 \pm 0.00031$ (Aghanim *et al.*, 2020b). The dependence of the cosmological model in Eq. (2.4) enters mainly via the Hubble parameter (c.f. Eq. 1.15):

$$\frac{H^2(z)}{(100 \text{ km/s/Mpc})^2} = \omega_m(1 + z)^3 + h^2 - \omega_m, \quad (2.5)$$

where $\omega_m = \omega_b + \omega_c$. In the following, we will see that Eq. (2.4) becomes an implicit equation for H_0 in flat Λ CDM since CMB data can constrain ω_r , ω_b and ω_c independently from θ_s .

Constraints on ω_r , ω_b , ω_m from CMB data

The *radiation density*, ω_r , consisting of photons and neutrinos, can be inferred from the temperature and density of the CMB photons. The temperature is fixed by COBE's Far Infrared Absolute Spectrophotometer (FIRAS) finding $T = 2.725 \pm 0.002$ K (Mather *et al.*, 1999; Fixsen *et al.*, 1996). For a black-body spectrum, the energy density in radiation is then given by (e.g. Weinberg (2008), their Ch. 2.1):

$$\rho_{0,\text{CMB}} = \int_0^{\infty} h\nu \cdot n(\nu) d\nu = \frac{8\pi^5 k_B^4}{15h^3 c^3} T^4 = 4.64 \times 10^{-34} \text{ g/cm}^3, \quad (2.6)$$

where $n(\nu)$ is the number density of CMB photons with frequency ν and h is the Planck constant. Taking into account the earlier time of decoupling of neutrinos, one finds that the contribution of neutrinos to the energy density is about $0.4 \rho_{0,\text{CMB}}$. Since the CMB and neutrinos are by far the dominant contribution to the radiation density of the Universe, one finds for the fractional energy density: $\Omega_r = 1.4 \rho_{0,\text{CMB}}/\rho_{\text{crit}} = 4.15 \times 10^{-5} h^{-2}$. Since it is so precisely measured, $\rho_{0,\text{CMB}}$ is usually fixed during parameter inference.

The *baryon density*, ω_b , appears in the equation for the sound horizon θ_s (2.4) via $H(z)$ and the sound speed c_s (2.2) by fixing the baryon-to-photon ratio R . Apart from having an impact on the sound horizon, ω_b has two other effects on the CMB temperature power spectrum:

(1) A higher ω_b leads to a tighter coupling of the photons to the baryon fluid, which leads to less diffusion. Spatial diffusion of photons between hot and cold regions leads to *Silk damping*. Therefore, a higher ω_b leads to less suppression of the temperature power spectrum at large scales ($\ell > 1000$) due to Silk damping.

(2) ω_b also affects the inertia of the baryon-photon fluid: a larger ω_b leads to a larger baryon-to-photon ratio, R , which leads to a larger inertia of the baryon-photon fluid. The baryon inertia increases overdensities as compared to underdensities since the change of direction at a maximal overdensity needs to work against the inertia. The baryon inertia acts like a force term that changes the zero point of the oscillations. As the even and odd peaks in the temperature power spectrum correspond to maximal under- and overdensities in the density field, respectively, a higher ω_b decreases the even while increasing the odd peaks.

The *total matter density*, ω_m , is constrained in particular by the height of the acoustic peaks: Less matter, i.e. a smaller ω_m , leads to a later time of matter-radiation equality. While in a matter-dominated Universe, the gravitational potential is constant, the presence of radiation leads to a decay of the gravitational potential. Hence, a later time of matter-radiation equality leads to a stronger decay of the gravitational potentials at recombination. This effect is known as the *early integrated Sachs-Wolfe effect* (eISW). Since the eISW adds in phase with the BAO, this leads to a boost of all peaks, particularly the first peak.

Constraining the Hubble constant h with CMB data

Since ω_b , ω_r and ω_m can be constrained independently from the sound horizon θ_s , Eq. (2.4) becomes an implicit equation for H_0 . Using a full treatment of the Boltzmann equation system for the CMB temperature and polarization fluctuations, NASA's WMAP CMB experiment determined $H_0 = 70.0 \pm 2.2 \text{ km/s/Mpc}$ (Hinshaw *et al.*, 2013), which is consistent with the low-redshift measurements of H_0 . The Hubble tension was 'discovered' in 2013 between the first data release of ESA's *Planck* satellite, which found $H_0 = 67.3 \pm 1.2 \text{ km/s/Mpc}$ (Ade *et al.*, 2014a) and measurements based on the distance ladder ($H_0 = 73.8 \pm 2.4 \text{ km/s/Mpc}$, Riess *et al.*, 2011; Freedman *et al.*, 2012). The final *Planck* data release gives $H_0 = 67.4 \pm 0.5 \text{ km/s/Mpc}$ (Aghanim *et al.*, 2020b).

Inferring H_0 from the sound horizon depends sensitively on the assumed cosmological model

(here: flat Λ CDM). We will later demonstrate how, with the assumption of a different cosmological model, a CMB-inferred H_0 can be obtained that is more compatible with direct late-time measurements (see Sec. 2.4).

2.2.2 Baryon acoustic oscillations in galaxy surveys

The BAO, which are imprinted in the CMB radiation, also left a pattern in the density field of the early Universe, which can still be observed in the large-scale structure (LSS) today. Galaxy surveys measure the positions of thousands to millions of galaxies in redshift space using spectroscopic data to identify known spectral features (see Sec. 1.5.4), e.g. the 6 Degree Field Galaxy Survey (6dFGS, Beutler *et al.*, 2011), the Sloan Digital Sky Survey (SDSS, Ross *et al.*, 2015), the Baryon Oscillation Spectroscopic Survey (BOSS, Alam *et al.*, 2017). The BAO can be observed as a ‘bump’ in the galaxy two-point correlation function or as a periodic oscillation in the galaxy power spectrum. The BAO were first detected by the SDSS and 2dFGS surveys and have a size of around 150 Mpc today (Eisenstein *et al.*, 2005; Cole *et al.*, 2005).

The characteristic length scale of the BAO in the 3-dimensional galaxy distribution can be used as a standard ruler. Since the BAO scale has the same length in all three spatial dimensions, it can be used to measure distortions in the observed BAO that are caused by the Alcock-Paczyński effect, i.e. by assuming a fiducial cosmology that differs from the underlying true cosmology. The distortions are parameterized by $\alpha_{\perp} = \frac{\delta\chi}{\chi_{\text{fid}}} = \frac{\delta D_A}{D_{A,\text{fid}}}$ in the direction perpendicular to the line of sight and $\alpha_{\parallel} = \frac{\delta H}{H_{\text{fid}}}$ in the direction parallel to the line of sight (c.f. Sec. 1.5.4). From the α -parameters, one can infer the true angular diameter distance and true Hubble parameter at the redshift z of the survey:

$$D_A(z) = D_{A,\text{fid}}(z)(1 + \alpha_{\perp}), \quad H(z) = H_{\text{fid}}(z)(1 + \alpha_{\parallel}). \quad (2.7)$$

Both $D_A(z)$ and $H(z)$ depend on H_0 and Ω_m . One possibility to break the degeneracy between H_0 and Ω_m is by observing BAO at different redshifts. Another possibility is to use the knowledge of the relation of the BAO to the sound horizon in Eq. (2.4). The angular size of the sound horizon, θ , at redshift, z , is

$$\theta(z) = \frac{a(z) r_s}{D_A(z)}, \quad (2.8)$$

where $a(z) r_s$ is the physical size of the sound horizon at redshift z . The size of the sound horizon at recombination, r_s , depends on ω_m , H_0 , ω_r and ω_b (c.f. Eq. 2.4). ω_r is fixed by the CMB temperature. ω_b can be obtained independently from CMB data by using observations of element ratios created during big bang nucleosynthesis (BBN, see Sec. 1.5.1). The primordial deuterium-to-hydrogen ratio is very sensitive to ω_b and can be used to constrain it precisely, e.g. $D/H = 2.527 \pm 0.030 \times 10^{-5}$ (Cooke *et al.*, 2018). With ω_b fixed, Eq. (2.8) breaks the degeneracy between Ω_m and H_0 when combining BAO from various redshifts including $z = z^*$. Using BAO measurements from SDSS and (e)BOSS combined with a BBN constraint, Alam *et al.* (2021) obtain $H_0 = 67.35 \pm 0.97$ km/s/Mpc.

Such a measurement of H_0 is considered an indirect measurement since it depends on r_s , which is sensitive to the cosmological model at early universe, as well as on D_A , which is sensitive to the cosmological model at late times.

2.3 Direct measurements of H_0

Direct measurements do not or only weakly depend on the assumed cosmological model. Many innovative ways have been used in the literature to infer H_0 from low-redshift probes. We will only discuss a small fraction of them in the following.

2.3.1 Cepheid-calibrated Type Ia SNe

The SH0ES (‘Supernovae, H_0 for the Equation of State of dark energy’) collaboration measures H_0 using the *distance ladder*. The idea behind the distance ladder is to infer the recession velocity v and distance D of *standardizable candles* deep in the Hubble flow in order to infer H_0 .

The SH0ES experiment uses Type Ia supernovae (SNe) as standardizable candles. Type I SNe are characterized by their spectra, which do not show a hydrogen line since the star has been stripped of their outer hydrogen shells (Carroll and Ostlie, 1996). Precise measurements of the light curve, i.e. the luminosity as a function of time, can be calibrated using the light-curve vs. luminosity relation in order to obtain the absolute magnitude (or luminosity) of the SN, from which the distance to the SN can be inferred.

Since SNe are relatively rare events, SNe Ia are only observed in distant galaxies. To calibrate the SN light-curve-luminosity relation, one can use different *anchors*. The SH0ES project uses Cepheid variable stars as anchors, which are pulsating stars with a very precise relation between pulsation period and luminosity. Using galaxies, which host both Cepheids and one or several SNe Ia, one can employ the Cepheid period-luminosity relation to calibrate the SN Ia light-curve-luminosity relation. Cepheids are much more common than SN Ia and a large number of them can be observed in the Milky Way. The Cepheids in the Milky Way themselves can be calibrated with parallax measurement by telescopes like Gaia (Riess *et al.*, 2021). The parallax method is a geometric method that utilizes the movement of the Earth (or the satellite) with respect to the comoving frame to measure the apparent angle that a distant object, e.g. a Cepheid variable star, subtends on the sky; this is a direct measure of the distance of the object. However, it can only be used for very close objects, i.e. not outside the Milky Way.

Using Cepheid-calibrated Type Ia SNe, the SH0ES collaboration inferred $H_0 = 73.04 \pm 1.04$ km/s/Mpc (Riess *et al.*, 2022).

2.3.2 TRGB-calibrated Type Ia supernovae

An alternative calibrator for the SN Ia in the Hubble flow is the tip of the red giant branch (TRGB). Red giants are stars that evolved from the main sequence, which have burned all the hydrogen in the core and started burning hydrogen in a shell around the core, developing a convection zone on the surface of the star. Therefore, although being cooler and taking on a red-orange color, they become brighter than when they were on the main sequence. The red giants follow the red-giant branch on the Hertzsprung-Russel diagram. The TRGB marks the position in the Hertzsprung-Russel diagram where the temperature in the core of the star becomes high enough that helium fuses to carbon and further to oxygen. This process makes the core expand and dilutes the hydrogen-burning shell and consequently cools it rapidly. The sudden cooling leads to an abrupt decrease in luminosity, which in turn leads to the sudden cutoff in the red giant branch known as the TRGB. Therefore, the TRGB is a standardizable empirical measure of the luminosity of the brightest objects in a given stellar population (Carroll and Ostlie, 1996).

The brightest stars in the TRGB are similarly accurate standardizable candles as the Cepheids, however, they are not as bright as the Cepheids. Since they are based on different physics, they present an important alternative calibrator of the SNe Ia. Using TRGB-calibrated SNe Ia, the Carnegie-Chicago Hubble Program (CCHP) determined the Hubble constant to be $H_0 = 69.8 \pm 2.5$ km/s/Mpc (Freedman *et al.*, 2019). This measurement of H_0 is consistent with both the *Planck* CMB-inferred value (Aghanim *et al.*, 2020b) and the value inferred from Cepheid-calibrated Type Ia SNe (Riess *et al.*, 2022) and hence, does not display any Hubble tension. Other groups independently used TRGB-calibrated SNe Ia and found slightly different values (Anand *et al.*, 2022; Yuan *et al.*, 2019) due to different choices in the calibration of the TRGB with geometric distance indicators like parallax or megamasers and due to differences in the treatment of the SNe Ia in the Hubble flow (Kamionkowski and Riess, 2022). Understanding the difference between H_0 using Cepheid- and TRGB-calibrated SNe is important and the James Web Space Telescope may help to resolve this difference.

2.3.3 Gravitational-lens time delays

If light rays from a background source pass by a massive foreground object, e.g. a galaxy cluster, their path is deflected by the gravitational potential of the foreground object. This effect is referred to as *strong gravitational lensing* when multiple images of the same object occur.

If a time-varying source, e.g. an active galactic nucleus (AGN) or a SN, is multiply lensed, the difference in path length of the different images leads to time delays in the arrival time of the photons. This time delay can be used to infer H_0 (Refsdal, 1964) via the time delay distance, which is given by

$$D_{\Delta t} = (1 + z_d) \frac{D_d D_s}{D_{ds}}, \quad (2.9)$$

where z_d is the redshift of the lens, and D_d , D_s , D_{ds} are the angular diameter distances of the lens,

the source and between lens and source, respectively. The physical angular diameter distance $D_A(z) = a(z) \int_0^z dz/H(z)$ (see Eq. (1.21)) depends on H_0 and ω_m (if $\Omega_k = 0$) via $H(z)$ (see Eq. (2.5)). The dependence on H_0 is much stronger than on ω_m and hence there is only a mild dependence on the cosmological model. The time delay distance $D_{\Delta t}$ in Eq. (2.9) can be inferred from the measured time delay between the separate images of the source (Suyu *et al.*, 2018).

Using 6 gravitationally-lensed quasars, the H0LiCOW collaboration (‘ H_0 Lenses in COSMOGRAIL’s Wellspring’, Suyu *et al.*, 2017) inferred $H_0 = 73.3_{-1.8}^{+1.7}$ km/s/Mpc (Wong *et al.*, 2020). This is in 3.1σ tension with the value inferred by *Planck* and in agreement with the SH0ES result. However, this analysis assumed a fixed mass density profile of the foreground lens. Varying the lens potential has a strong impact on the inferred value of H_0 due to the *mass sheet degeneracy* (Birrer *et al.*, 2020). This degeneracy can be broken by high-resolution imaging and accurate spectroscopy of the lens (Shajib *et al.*, 2023) and is topic of active research in the TDCOSMO collaboration (‘Time Delay Cosmography’).

Instead of quasars, the HOLISMOKES collaboration (‘Highly Optimised Lensing Investigations of Supernovae, Microlensing Objects, and Kinematics of Ellipticals and Spirals’, Suyu *et al.*, 2020) uses strongly-lensed SNe to constrain H_0 and will provide another independent direct measurement of H_0 .

2.3.4 Type II SNe

Type II SNe are supernovae, which contain strong hydrogen lines. They consist of stars whose mass is above the Chandrasekhar mass limit. Hence, once fusion cannot maintain the pressure to withstand the gravity, they explode in a core-collapse SN (Carroll and Ostlie, 1996).

One can calibrate the light-curve-luminosity relation of Type II SNe similarly to the Type Ia SNe using Cepheids or the TRGB. Using this method (de Jaeger *et al.*, 2022) found $H_0 = 75.4_{-3.7}^{+3.8}$ km/s/Mpc.

Since the underlying physics of Type II SNe² are better understood than of the Type Ia, one can model the light curves and the spectra of SN II and directly infer the absolute magnitude of the SN. This method is known as *expanding photosphere method* (Schmidt *et al.*, 1992) and can be used as a one-step inference of H_0 without the need of the distance ladder. This method is still being developed but will soon provide first constraints on H_0 (Gall *et al.*, 2018; Csörnyei *et al.*, 2023).

2.3.5 Other measurements of the Hubble tension

There are numerous other ways to measure the expansion rate of the Universe, which are beyond the scope of this short introduction. We will name a few further methods in the following.

²One typically uses Type IIP SNe.

Surface brightness fluctuations use the ‘granularity’ of galaxies to infer the distance and find $H_0 = 73.3 \pm 3.1$ km/s/Mpc (Blakeslee *et al.*, 2021). *Fast radio bursts* are very bright bursts of radio emission, which can be used to infer H_0 via the electron dispersion measure along the line of sight giving $H_0 = 62.3 \pm 9.1$ km/s/Mpc (Hagstotz *et al.*, 2022). *Megamasers*, which are sources of monochromatic microwave radiation from accretion discs containing water (the H_2O line) around black holes, open the possibility for geometric distance inference and yield $H_0 = 73.9 \pm 3.0$ km/s/Mpc (Pesce *et al.*, 2020). The *ages* of old objects like globular clusters and very-low-metallicity stars (e.g. Jimenez *et al.*, 2019) can be used to infer H_0 . Also gravitational waves (Schutz, 1986) can be used to determine H_0 , although the uncertainties are still large.

Improving the uncertainties from these measurements presents a promising avenue and will shed new light on possible systematics behind one or several of the H_0 measurements.

2.4 New physics to resolve the Hubble tension?

Since the ‘discovery’ of the Hubble tension between the distance ladder (Riess *et al.*, 2011; Freedman *et al.*, 2012) and *Planck* 2013 data (Ade *et al.*, 2014a), a great effort has been spent on the search for possible systematics in either or several of the measurements. However, no plausible explanation has been put forward, which can explain nowadays’ 5σ tension between direct and indirect measurements (e.g. Freedman *et al.*, 2019; Efstathiou, 2020; Mortsell *et al.*, 2022; Di Valentino *et al.*, 2021; Abdalla *et al.*, 2022).

If on the other hand, if the H_0 tension is not caused by systematics in one or more of the experiments, the tension could hint towards new physics beyond the standard Λ CDM model. Many possible extensions of Λ CDM have been proposed in the literature, which could alleviate or resolve the tension. Since the direct measurements of H_0 discussed in Sec. 2.3 do not (or only weakly) depend on the cosmological model but rather on very different astrophysical modelling, it is difficult to introduce new physics that *decrease* the preferred values of H_0 of the direct measurements. Therefore, the common scheme to attempt to resolve the H_0 tension is to *increase* the value of the indirect measurements of H_0 discussed in Sec. 2.2 by modifying the cosmological model. Both indirect measurements discussed in Sec. 2.2 depend sensitively on the angular size of the sound horizon, θ_s (c.f. Eq. 2.4). It becomes apparent that there are two main avenues to resolve the H_0 tension by introducing new physics: The first is to modify the cosmological model in the early Universe between the Big Bang ($z = \infty$) and recombination ($z = z_*$) by introducing new physics that modifies the physical size of the sound horizon r_s . This can be done by modifying the sound speed of the baryon-photon fluid c_s or by modifying the expansion history $H(z)$ in the early Universe. This type of solutions has been dubbed *early-Universe solutions*.

The second avenue is to introduce new physics in the late Universe, known as *late-Universe solutions*, in order to modify the expansion rate $H(z)$ between the redshift of recombination ($z = z_*$) and today ($z = 0$). However, this second avenue turns out to be very challenging. Due

to the large amount of data that is available between redshift $z = 0$ and redshift $z = 1$ from e.g. BOSS BAO and uncalibrated Pantheon SN data, the *relative* expansion rate $H(z)$ at low redshifts is tightly constrained (Bernal *et al.*, 2016; Addison *et al.*, 2018; Lemos *et al.*, 2019; Aylor *et al.*, 2019; Knox and Millea, 2020). This leaves little room for changes of $H(z)$ at low redshift. For example, the late-Universe solutions considered by Schöneberg *et al.* (2022) manage to achieve a high H_0 when considering *Planck* CMB and BOSS BAO data combined with a SH0ES-informed prior on H_0 . However, when including the full Pantheon and SH0ES likelihood, a mismatch in the absolute SN luminosity M_B between the model and the Pantheon data appears. Hence, most late-Universe solutions, which simply modify $H(z)$ at low redshifts, trade the tension in H_0 for a tension in the absolute SN luminosity M_B (Camarena and Marra, 2021; Efstathiou, 2021). This apparent resolution of the tension can be avoided by using a likelihood in M_B instead of H_0 .³

As a consequence of the difficulty of finding late-Universe solutions, the community turned towards finding workable early-Universe solutions (Knox and Millea, 2020; Schöneberg *et al.*, 2022). One prime example of such solutions is *Early Dark Energy* (EDE), which we will discuss in the next section.

2.5 A possible solution: Early Dark Energy

The idea behind *Early Dark Energy* (EDE) is simple: EDE introduces an additional component in the early Universe, which boosts the expansion rate $H(z)$ before recombination. From Eq. (2.4), we see that this reduces the physical size of the sound horizon r_s . Since θ_s is fixed by observations (it is very precisely measured by *Planck* CMB data), a reduced r_s leads to a reduced angular diameter distance to last scattering, D_A , in Eq. (2.4).

The angular diameter distance is inversely proportional to the expansion rate, $D_A \sim 1/H(z)$, which is given by Eq. (2.5) and depends on ω_r , ω_m , and h . Since ω_r and ω_m are not only constrained via the position of the CMB peaks, i.e. θ_s , but are fixed by other CMB observables (c.f. Sec. 2.2.1), the increase of $H(z)$ translates directly into an increase of h . Therefore, introducing an extra component before recombination that boosts $H(z)$, leads to an increase of the expansion rate today, H_0 . Since direct measurements of H_0 are about 10% higher than the indirect measurements, this effect needs to reduce the sound horizon by about 10% to resolve the Hubble tension. In the following, we will discuss a working example of how this energy injection before recombination could be realized by a dark-energy-like component in the early Universe.

³See however Krishnan *et al.* (2020), who find a hint of time evolution in the BAO, SNe and cosmic chronometers, which disfavors early-time solutions to the Hubble tension.

2.5.1 The axion-like EDE model

Early Dark Energy has become an umbrella term for a whole plethora of models, which fulfill the basic idea described above. The presence of early dark energy has been studied already since the year 2000 in the context of quintessence models (Doran *et al.*, 2001; Wetterich, 2004; Doran and Robbers, 2006).

In this thesis, we will focus on the ‘canonical’ *axion-like EDE* model, which is a promising candidate to resolve the H_0 tension and is the most well-studied EDE model in the literature. The EDE model consists of an axion-like scalar field ϕ , with potential

$$V(\phi) = V_0[1 - \cos(\phi/f)]^n, \quad (2.10)$$

with $V_0 = m^2 f^2$, where m is called ‘mass’⁴ and f the spontaneous symmetry breaking scale. The potential from Eq. (2.10) is shown in Fig. 2.2 for different indices n , where n determines the steepness of the potential. The standard axion potential is obtained if $n = 1$.⁵ This type of potential was proposed by Kamionkowski *et al.* (2014) in order to explain why the onset of accelerated expansion caused by (late) dark energy occurred only recently. EDE has been first proposed as a solution to the H_0 tension by Karwal and Kamionkowski (2016) and shown to be able to solve the H_0 tension by Poulin *et al.* (2018, 2019)⁶.

Apart from the axion-like potential in Eq. (2.10), many alternative ideas for the EDE potential have been proposed in the literature. We will name a few well-studied examples in the following (for a review see Poulin *et al.*, 2023). *Rock ’n’ Roll EDE* (Agrawal *et al.*, 2019) for example assumes a power law potential of the form $V(\phi) \sim \phi^{2n}$, which approximates the axion-like potential in Eq. (2.10) for small ϕ/f . The *Acoustic EDE* model generalizes the EDE model (at the level of the background) by using a phenomenological fluid description of EDE parameterized by the sound speed c_s^2 and equation-of-state parameter w_{ADE} (Lin *et al.*, 2019). *New Early Dark Energy* (NEDE) realizes the onset of decay by a phase transition by coupling the NEDE field to a trigger field. The trigger field continuously changes the potential perceived by the NEDE until the NEDE field tunnels to its true vacuum, where it starts to decay. This tunneling process is more natural than the axion-like EDE potential (Niedermann and Sloth, 2021, 2020). The NEDE phase transition can also be realized by a coupling to a dark gauge sector dubbed *Hot NEDE* (Niedermann and Sloth, 2022). The EDE field can also be realized by axion-dilaton destabilization (Alexander and McDonough, 2019), the existence of anti-De Sitter vacua (Ye and Piao, 2020), in the framework of α -attractors (Braglia *et al.*, 2020b), in $F(R)$ gravity (Oikonomou, 2021), in the context of *Chain EDE* (Freese and Winkler, 2021), in the context of *Chameleon EDE* (Karwal *et al.*, 2022), in a more general framework of the equation of state (Nojiri *et al.*, 2021) or different microphysics (Sabla and Caldwell, 2022).

⁴The effective mass of the potential is defined as $m_{\text{eff}}^2 = \frac{dV(\phi)}{d\phi}$ close to the minimum of the potential, $\phi \approx 0$. Hence, $m_{\text{eff}} \sim m$ only for $n = 1$.

⁵Higher indices of n can be generated by higher-order instanton corrections (Kappl *et al.*, 2016).

⁶The EDE model considered by Karwal and Kamionkowski (2016) did only include EDE as a background quantity and concluded that EDE is not able to resolve the tension. However, when including perturbations, which is a more consistent treatment of the model, Poulin *et al.* (2019) show that EDE can resolve the H_0 tension.

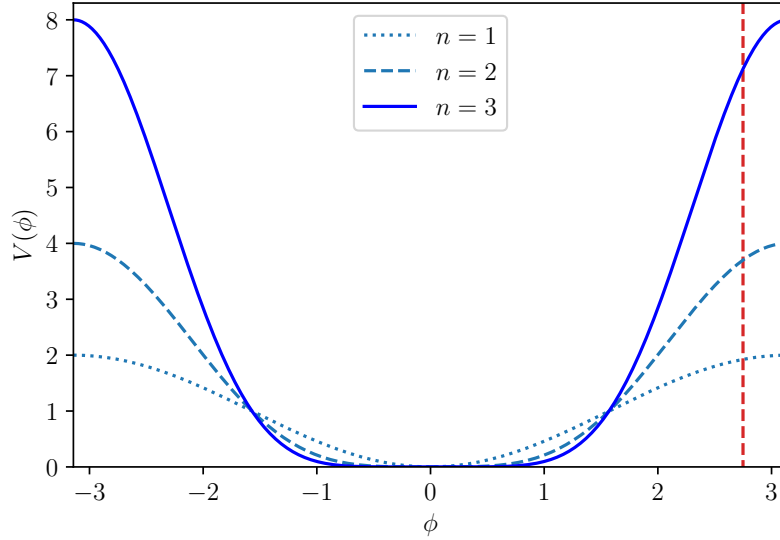


Figure 2.2: The axion-like EDE potential from Eq. (2.10) for $f = m = 1$ and different choices of the index n . The vertical red-dashed line marks the best-fit initial field value $\theta_i = \phi_0/f$ for $n = 3$ obtained from a fit to *Planck* and BOSS full-shape data (see App. 5.6).

2.5.2 Dynamics of the EDE model

The EDE background

The dynamics of a scalar field are governed by the Klein-Gordon equation (c.f. Sec. 1.4):

$$\ddot{\phi} + 3H\dot{\phi} + \frac{dV(\phi)}{d\phi} = 0, \quad (2.11)$$

where $\langle \cdot \rangle$ denotes the derivative with respect to cosmological time, t . At early times, the expansion rate, $H(t)$, is large and the Hubble-friction term, $3H\dot{\phi}$, dominates such that the potential-gradient term $dV(\phi)/d\phi$ in Eq. (2.11) can be neglected: $\ddot{\phi} + 3H\dot{\phi} \approx 0$. Since $\dot{\phi} \gg V(\phi)$, the equation of state parameter is (c.f. Eq. 1.27):

$$w_{\text{EDE}} = \frac{p}{\rho} = \frac{\frac{\dot{\phi}^2}{2} - V(\phi)}{\frac{\dot{\phi}^2}{2} + V(\phi)} \approx -1 \quad \text{for } z \gg z_c. \quad (2.12)$$

Hence, the *slow-roll phase* leads to an accelerated growth of the field, similar to inflation (Sec. 1.4). The *critical redshift*, z_c , marks the redshift at which the Hubble friction term becomes of the same size as the potential-gradient term. Note that Eq. (2.12) justifies calling this field (early) dark energy. Since in the radiation and matter dominated eras, the Universe undergoes decelerated expansion (c.f. Eq. 1.13), i.e. $H(z)$ decreases, at times $z \ll z_c$, the Hubble friction

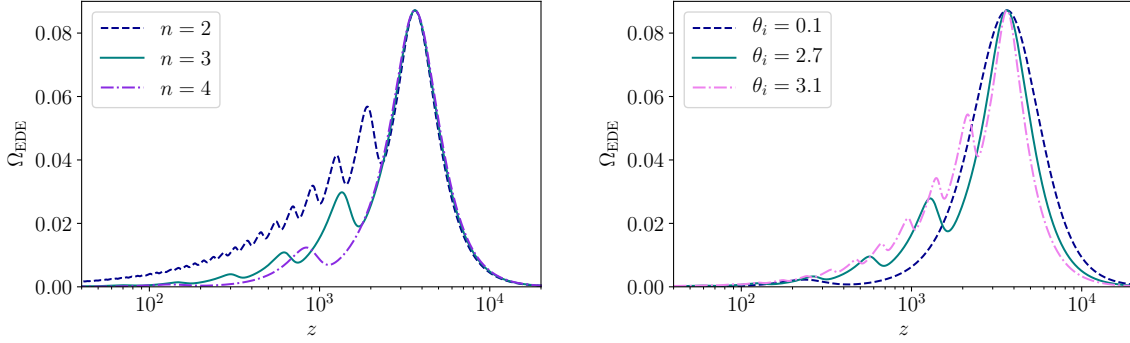


Figure 2.3: Fractional energy density of EDE, Ω_{EDE} , as a function of redshift, z for different values of the index, n , for $\theta_i \approx 2.7$ (left), and different values of the initial value of the scalar field, $\theta_i = \phi_i/f$, for $n = 3$ (right). All cosmological parameters are fixed to the best-fitting parameters obtained for *Planck* and BOSS data (see Tab. 5.6.2). All plots in this section are based on computations done with CLASS_PT (Chudaykin *et al.*, 2020, see text).

term can be neglected compared to the potential-gradient term: $\ddot{\phi} + \frac{dV(\phi)}{d\phi} = 0$. One can easily see that this leads to oscillatory solutions, e.g. expanding the potential for small fields ϕ gives $V(\phi) \approx V_0 \left[\frac{\phi^2}{f^2} \right]^n$, which for $n = 1$ has solutions of the form $\phi(t) \sim \cos\left(\sqrt{\frac{2V_0}{f^2}}t\right)$. By solving the differential equation for $V(\phi) \sim \phi^{2n}$ and using the virial theorem, one can show that during the oscillatory phase the time-average of the equation-of-state parameter is (Poulin *et al.*, 2018):

$$\langle w_{\text{EDE}} \rangle = \frac{n-1}{n+1} \quad \text{for } z \ll z_c, \quad (2.13)$$

where $\langle \cdot \rangle$ denotes the average over time. Inserting Eq. (2.13) into Eq. (1.8), we find for the fractional energy density in EDE:

$$\Omega_{\text{EDE}}(t) = \frac{\rho_{\text{EDE}}}{\rho_{\text{crit}}} \sim [a(t)]^{-3(1+\frac{n-1}{n+1})}. \quad (2.14)$$

Hence, the higher n , the quicker the field redshifts or ‘decays’. E.g. for $n = 1$, the EDE field redshifts like matter ($w = 0$), for $n = 2$, the field redshifts like radiation ($w = 1/3$), and for $n > 3$, the field redshifts faster than radiation ($w > 1/2$). In Fig. 2.3 (left), we show the fractional energy density in EDE, Ω_{EDE} , for different indices n : the larger n , the faster the EDE field redshifts away. The other parameters are fixed to the best fit obtained from *Planck* and BOSS full-shape data for fixed $n = 3$ and tabulated in App. 5.6. When letting the index, n , vary in an analysis using *Planck* CMB, BOSS BAO, and Pantheon and SH0ES SN data, the best fit lies close to $n = 3$ (Smith *et al.*, 2020).⁷ In principle, n can be considered as a free parameter of the model. However, since n does not have a strong influence on the ability of EDE to resolve the Hubble tension as long as $n \geq 3$, it became customary in the EDE literature to fix the index to $n = 3$ (Poulin *et al.*, 2023).

⁷Poulin *et al.* (2023) update the result by Smith *et al.* (2020) and find $n = 3.37^{+0.41}_{-0.99}$.

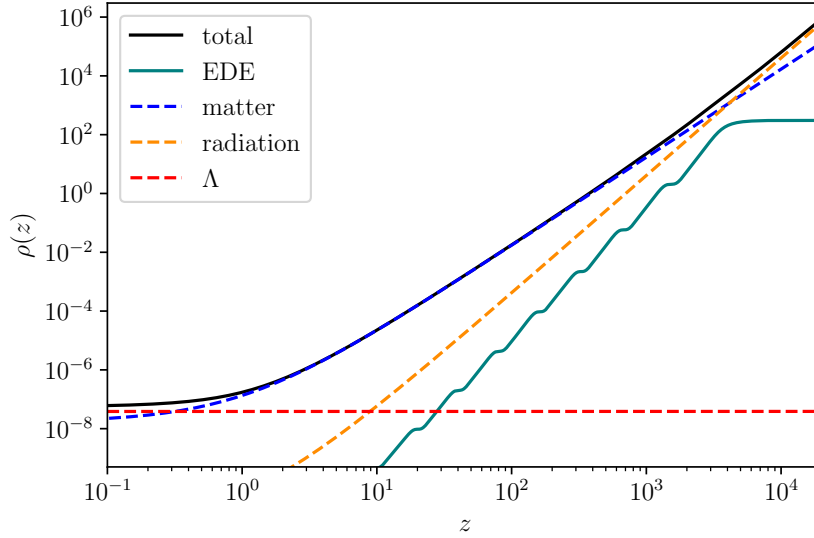


Figure 2.4: Total energy density, $\rho(z)$, for different species for the EDE cosmology with $n = 3$ that corresponds to the best fit to *Planck* and BOSS full-shape data. EDE (teal solid line) constitutes a subdominant component, which decays faster than radiation (orange) after $z_c = 3.6 \times 10^3$.

In Fig. 2.4, we show the contributions to the total energy density, $\rho(z)$ (black solid) for the best-fitting EDE model with $n = 3$ obtained from a fit to *Planck* and BOSS data (see App. 5.6), containing a maximum fractional energy density $f_{\text{EDE}} \approx 9\%$ of EDE. At high redshifts, ρ_{EDE} (teal solid line) is approximately constant, until at the critical redshift, $z_c = 3.6 \times 10^3$, the field starts oscillating and decays faster than matter (blue dashed line) and radiation (orange dashed line).

The initial value of the EDE field in the potential (2.10), i.e. the initial field displacement, is typically parameterized by the dimensionless parameter: $\theta_i := \frac{\phi_i}{f}$, where $\phi_i = \phi(t = 0)$. Fig. 2.3 (right) shows the fractional energy density in EDE, Ω_{EDE} , for different values of θ_i . The closer θ_i is to $\pi \approx 3.1$ (purple dashed line), the higher the field starts in the potential (2.10) and the faster the field oscillates. CMB and BAO data prefer θ_i to be near the peak of the potential Smith *et al.* (2020). From a fit, to *Planck* and BOSS full-shape data, we obtain a best-fit $\theta_i = 2.749$ (see Ch. 5), which is indicated as the vertical dashed red line in Fig. 2.2 and plotted as the solid teal line in Fig. 2.3 (right).

The fractional energy density in the EDE field, Ω_{EDE} peaks at the critical redshift z_c , i.e. when the Hubble friction term and the potential-gradient term in Eq. (2.11) become of the same size, $3H\dot{\phi}^2 \approx V(\phi)$, and the field starts to oscillate in the potential. At z_c , the EDE field reaches its

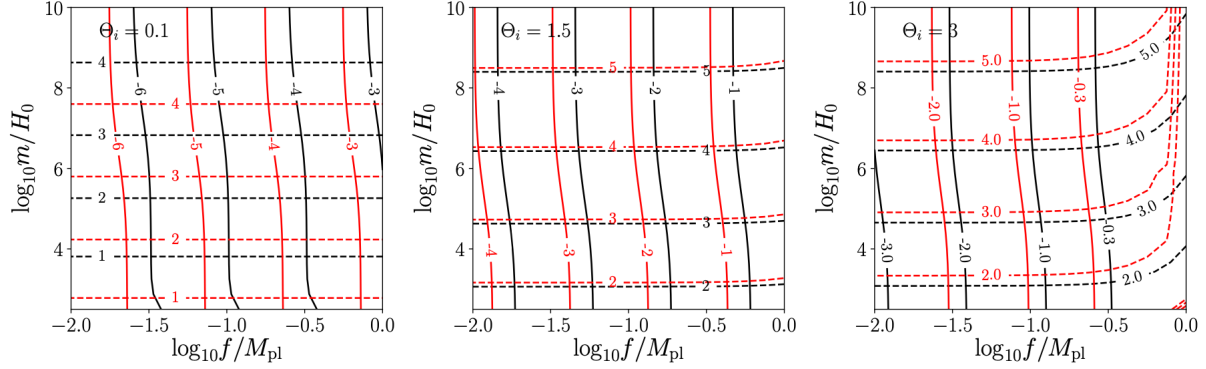


Figure 2.5: Relation between the phenomenological parameters $\{f_{\text{EDE}}, z_c\}$ and the particle-physics parameters $\{m, f\}$ for three different values of θ_i (indicated in the upper left corner of each subplot). Vertical solid lines show contours of constant $\log_{10} f_{\text{EDE}}$ and horizontal dashed lines show contours of constant $\log_{10}(z_c)$, while red lines show contours for $n = 2$, black lines show contours for $n = 3$. Taken from Smith *et al.* (2020).

maximal fractional energy density, $f_{\text{EDE}} := \Omega_{\text{EDE}}(z_c)$. Inserting Eq. (1.9), we obtain

$$f_{\text{EDE}} = \frac{\rho_{\text{EDE}}}{\rho_{\text{crit}}}(z_c) \approx \frac{8\pi G_N V(\phi_i)}{3H(z_c)^2}, \quad (2.15)$$

where we took into account that $V(\phi(z_c)) \approx V(\phi_i)$ since the field is frozen before z_c . This relates the maximum fraction of EDE, f_{EDE} , to the EDE parameters m and f for given values of z_c and θ_i .

There are two common ways to parameterize the EDE model while fitting to data: the *particle physics parametrization* given by $\{m, f, \theta_i\}$ and the *phenomenological parameterization* given by $\{f_{\text{EDE}}, z_c, \theta_i\}$. Fig. 2.5 shows how both parametrizations are related. m is strongly correlated with the onset of oscillations and, therefore, with z_c . The decay constant f on the other hand, sets f_{EDE} . The more commonly used parametrization when constraining the parameters with data in the literature is the phenomenological parametrization.

The EDE perturbations

The perturbations of the EDE field, $\phi = \bar{\phi} + \delta\phi$ can be described by the Klein-Gordon equation up to linear order in perturbations (in synchronous gauge and Fourier space, e.g. Smith *et al.*, 2020):

$$\delta\ddot{\phi}(k) + 3H\delta\dot{\phi}(k) + \left(\frac{k^2}{a^2} + \frac{dV(\phi)}{d\phi^2}\right)\delta\phi(k) = -\frac{\dot{\psi}\dot{\bar{\phi}}}{2}, \quad (2.16)$$

where ψ is the trace of the spatial-spatial metric perturbation (see Eq. 1.31). In practice, Eq. (2.16) is solved numerically and integrated in the framework of a Boltzmann solver. EDE (and more

general axion-like fields) have been implemented as an extension of the Boltzmann solver CLASS (Blas *et al.*, 2011) in AxiCLASS⁸ (Smith *et al.*, 2020). An alternative extension of CLASS including EDE appeared in CLASS_EDE⁹ (Hill *et al.*, 2020), which we will use in the following. Both implementations solve the full Klein-Gordon eq. (2.16). All plots in this section have been done using CLASS_EDE and include EDE perturbations up to linear order.

2.6 Can Early Dark Energy resolve the Hubble tension?

EDE aims to resolve the Hubble tension by introducing a dark-energy like component ($w_{\text{EDE}} = -1$ at early times), which increases the expansion rate just prior to recombination at a redshift of around $z \sim 10^3$. This is shown in Fig. 2.6 for two different cosmologies corresponding to the best-fitting parameters to *Planck* and BOSS (baseline) and baseline and SHOES. Ω_{EDE} peaks at $z_c = 3.6 \times 10^3$, leading to an increase in the expansion rate, $H_{\text{EDE}}(z)$, compared to $H_{\Lambda\text{CDM}}$ in the ΛCDM model around recombination. This decreases the size of the sound horizon, r_s , which leads to an increased $H(z)$ also at low redshifts (see overview in Sec. 2.4). In the following we will review the recent literature on constraints on EDE and discuss whether EDE can resolve the Hubble tension *and* present a good fit to different cosmological data sets.

2.6.1 EDE constraints from *Planck* CMB and BAO data

It was shown in Poulin *et al.* (2018, 2019) that the axion-like EDE model introduced in Sec. 2.5 can resolve the Hubble tension. In a fit to *Planck* (TT, TE, EE and lensing) CMB data, BAO and redshift-space distortion (RSD) data from 6dFGS, SDSS, BOSS, and SN data from Pantheon and SHOES they find a relatively high maximum fraction of EDE, $f_{\text{EDE}} = 0.050_{-0.019}^{+0.024}$, and a high $H_0 = 70.6 \pm 1.3$ km/s/Mpc. This value is compatible with the direct measurements of H_0 from SHOES, while improving the goodness of fit compared to the ΛCDM model by $\Delta\chi^2 = -14.5$. Since these first constraints, there have been many works constraining the parameters of the EDE model with different data-set combinations. We will discuss a few representative studies in the following and present an overview of the constraints on f_{EDE} and H_0 in Table 2.1.

Using slightly updated data sets compared to Poulin *et al.* (2019) and an improved modelling¹⁰, Smith *et al.* (2020) find $f_{\text{EDE}} = 0.107_{-0.030}^{+0.035}$ and $H_0 = 71.49 \pm 1.20$ km/s/Mpc. Both works suggest that EDE presents a possible solution to the H_0 tension.

While introducing EDE has the largest impact on H_0 , it also induces shifts in other ΛCDM

⁸<https://github.com/PoulinV/AxiCLASS>

⁹https://github.com/mwt5345/class_edc

¹⁰Poulin *et al.* (2019) use approximate ‘cycle-averaged’ fluid equations for the scalar-field perturbations, while Smith *et al.* (2020) solve the full fluid equations for the homogeneous part and perturbations up to linear order.

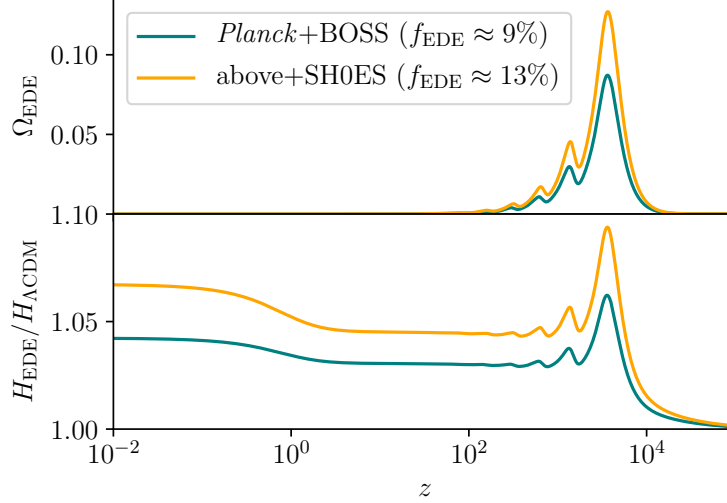


Figure 2.6: The fractional energy density of EDE, Ω_{EDE} (*top*), and the expansion rate, $H_{\text{EDE}}/H_{\Lambda\text{CDM}}$ (*bottom*), as a function of redshift z for different maximum fractions of EDE, f_{EDE} , corresponding to the best fit to *Planck* and BOSS full-shape data (teal) and *Planck*, BOSS full-shape and SH0ES data (orange).

Data sets	f_{EDE}	H_0 [km/s/Mpc]	Reference
<i>Planck</i> ; 6dFGS+SDSS (BAO), BOSS (BAO+RSD); Pantheon, SH0ES	$0.050^{+0.024}_{-0.019}$	70.6 ± 1.3	Poulin <i>et al.</i> (2019)
<i>Planck</i> ; 6dFGS+SDSS (BAO), BOSS (BAO+RSD); Pantheon, SH0ES	$0.107^{+0.035}_{-0.030}$	71.49 ± 1.20	Smith <i>et al.</i> (2020)
<i>Planck</i> ; 6dFGS+SDSS (BAO), BOSS (BAO+RSD); DES, KiDS, HSC; Pantheon	< 0.06	$68.92^{+0.57}_{-0.59}$	Hill <i>et al.</i> (2020)
<i>Planck</i> ; BOSS (BAO+FS)	< 0.072	$68.54^{+0.52}_{-0.95}$	Ivanov <i>et al.</i> (2020b)
<i>Planck</i> ; BOSS (BAO+FS); Pantheon	< 0.045	$67.39^{+0.46}_{-0.68}$	D'Amico <i>et al.</i> (2021b)
ACT, <i>Planck</i> (low ℓ); SDSS+BOSS (BAO)	$0.091^{+0.020}_{-0.036}$	$70.9^{+1.0}_{-2.0}$	Hill <i>et al.</i> (2022)
ACT, SPT, <i>Planck</i> (low ℓ)	$0.163^{+0.047}_{-0.04}$	$74.2^{+1.9}_{-2.1}$	Smith <i>et al.</i> (2022)

Table 2.1: Overview of selected constraints on the fraction of EDE, f_{EDE} , and the Hubble constant, H_0 , for EDE cosmologies with fixed index $n = 3$. The data sets, which have been considered in the respective study, are indicated in the first column. Note that the data sets from different studies can originate from different data releases.

parameters. Since EDE increases $H(z)$ before recombination, EDE cosmologies feature a suppressed growth of structure in the early Universe compared to Λ CDM. This suppressed growth leads to a stronger decay of the gravitational potential compared to a Universe filled with matter and radiation, enhancing the *early integrated Sachs-Wolfe effect* (eISW, see Sec. 2.2.1). The eISW effect enhances the amplitude of the acoustic peaks (particularly the first) and is, therefore, strongly constrained by CMB data. To compensate the enhanced eISW effect induced by the presence of EDE, EDE cosmologies feature a higher ω_c , n_s , and A_s (Smith *et al.*, 2020; Hill *et al.*, 2020; Vagnozzi, 2021). In the next section, we will discuss how measurements of the LSS can help to break degeneracies among the Λ CDM parameters that are generated by introducing EDE.

2.6.2 EDE constraints from LSS

Weak gravitational lensing or *cosmic shear* is a distortion of the observed shapes of galaxies as their light passes through the LSS on its way to Earth. The effect of weak lensing on a single galaxy is small but can be observed statistically for a large number of galaxies in weak lensing surveys like the Dark Energy Survey (DES, Abbott *et al.*, 2022), the Kilo Degree Survey (KiDS, Asgari *et al.*, 2021) or the Hyper Supreme Cam (HSC, Hikage *et al.*, 2019) survey.

Weak lensing surveys are particularly sensitive to $S_8 = \sigma_8(\Omega_m/0.3)^{0.5}$, where σ_8 is the amplitude of (linear) matter density fluctuations smoothed over a kernel with radius $R = 8 \text{ Mpc}/h$ (e.g. Dodelson and Schmidt, 2020):

$$\sigma_8^2 := \frac{1}{2\pi^2} \int d^3k P_{\text{lin}}(k) |W_8(k)|^2, \quad (2.17)$$

where P_{lin} is the linear matter power spectrum and $W_8(k)$ is the Fourier transform of a top-hat filter with a radius of $8 \text{ Mpc}/h$. Measurements of S_8 from weak lensing experiments yield higher values than indirect measurements from the CMB by $2 - 3\sigma$. This discrepancy is known as the S_8 *tension* (see Abdalla *et al.*, 2022, for a review). The increase in ω_c , n_s , and A_s in EDE cosmologies leads to a further increase of the CMB-inferred value of S_8 , *worsening* the S_8 tension.

Including data from the weak lensing surveys DES, KiDS and HSC, which prefer lower values of S_8 than CMB data, and excluding SH0ES from the analysis, Hill *et al.* (2020) find very tight upper limits on the fraction of EDE, $f_{\text{EDE}} < 0.06$, and a low $H_0 = 68.92_{-0.59}^{+0.57}$. Indeed, only when including the direct measurement of H_0 from SH0ES, they find high values of f_{EDE} , which lead to values of H_0 consistent with the SH0ES measurement.

A similarly tight constraint on f_{EDE} and low values of H_0 are obtained when including data of the full-shape of the BOSS galaxy power spectra data analysed with a model based on the effective field theory (EFT) of LSS discussed in 1.5.5. Compared to the traditional approach, which uses the BAO scale, the Alcock-Paczyński effect and RSD, this approach fits the full functional shape of the galaxy power spectrum. The EFT of LSS provides a model for the galaxy power spectrum, which is accurate up to mildly non-linear scales (see Sec. 1.5.5). The increase of S_8 in EDE cosmologies relative to Λ CDM leads to an increase of power in the galaxy power spectrum at

scales around $0.1h/\text{Mpc}$, which is accessible by current galaxy surveys like BOSS. Using the *Planck* CMB data and the full shape of the galaxy power spectrum based on the EFT of LSS, Ivanov *et al.* (2020b) find $f_{\text{EDE}} < 0.072$ and $H_0 = 68.54^{+0.52}_{-0.95} \text{ km/s/Mpc}$. D’Amico *et al.* (2021b) find $f_{\text{EDE}} < 0.45$ and $H_0 = 67.39^{0.46}_{-0.95}$ when additionally including SN data from Pantheon.¹¹

These analyses question the ability of EDE to simultaneously resolve the H_0 tension and fit LSS data sets, which are sensitive to the amplitude of matter clustering, S_8 . However, it has been pointed out by Smith *et al.* (2020) that the constraints on the EDE model can be subject to prior volume effects, which we will discuss in the next section.

2.6.3 Prior volume effects in the EDE model?

(*Prior*) volume effects, also known as projection effects or marginalization effects, refer to a strong influence of the prior in the *marginalized* or projected posterior, where marginalization refers to the integration over nuisance parameters (see Sec. 3.3.2). This typically happens if the data does not constrain all parameters of the model well (i.e. the model has too many parameters), the posterior is non-Gaussian, and/or the parameter structure of the model leads to large prior-volume differences. Prior volume effects will be discussed in more detail in Chapter 3.

Smith *et al.* (2020) argue that the structure of the EDE model can be particularly prone to prior volume effects¹²: EDE is typically parameterized by three parameters (for the index $n = 3$): the ‘abundance parameter’, f_{EDE} , and two parameters that describe EDE more closely, z_c and θ_i . This means that when the abundance approaches zero, $f_{\text{EDE}} \approx 0$, the two EDE parameters, z_c and θ_i , become unconstrained. In this limit, the model recovers ΛCDM with two extra parameters that are unconstrained by the data. On the other hand, when $f_{\text{EDE}} > 0$, the two parameters z_c and θ_i need to take on specific values in order to ensure a good fit to the data, for example CMB data. As a consequence, the prior volume (in the $f_{\text{EDE}} \times z_c \times \theta_i$ parameter space) for $f_{\text{EDE}} \approx 0$ is larger than for any $f_{\text{EDE}} > 0$. The *marginalized* f_{EDE} posterior is obtained by integrating the posterior over all parameters, including z_c and θ_i . Since the parameter (or prior) volume is much larger for $f_{\text{EDE}} \approx 0$ than for $f_{\text{EDE}} > 0$, the marginalization can lead to an up-weighting of small values of f_{EDE} .

In order to explore the influence of prior volume effects in analyses of EDE including LSS, Smith *et al.* (2021) fix z_c and θ_i to their best-fit values obtained by a fit to *Planck* data (referred to as ‘1-parameter model’)¹³. By fixing the two parameters, which are unconstrained, there is no volume difference between $f_{\text{EDE}} \approx 0$ and $f_{\text{EDE}} > 0$. Using BOSS full-shape data, *Planck* CMB and Pantheon SN data, they find $f_{\text{EDE}} = 0.0523^{+0.026}_{-0.036}$ for this 1-parameter model, while they find $f_{\text{EDE}} < 0.053$ for the full 3-parameter Markov Chain Monte Carlo (MCMC). Alternatively putting a tight Gaussian prior on z_c and θ_i also leads to higher values of f_{EDE} and H_0 as compared

¹¹See also recent constraints from Lyman- α forest data (Goldstein *et al.*, 2023), which disfavor the EDE model.

¹²The order of the cited articles is not chronological. Prior volume effects were already discussed by Smith *et al.* (2020) before weak-lensing and full-shape clustering data was used to constrain EDE.

¹³A 1-parameter model was already considered by Niedermann and Sloth (2020) in the context of NEDE.

to the full 3-parameter MCMC. (Smith *et al.*, 2021) show further that a model with $f_{\text{EDE}} = 0.09$ presents a similarly good fit as ΛCDM with $\Delta\chi^2 = 0.12$. Although fixing two parameters to their best-fitting values can lead to double-counting of the data set and under-estimation of the statistical errors, this study gives evidence for the influence of prior volume effects in the analysis of the EDE model using CMB and LSS probes.

In order to understand whether EDE presents a viable solution to the Hubble tension, it is vital to understand the influence of prior volume effects on the constraints of the EDE model. We will devote Chapters 4 and 5 to this open problem.

2.6.4 Ground-based CMB experiments prefer EDE

The Atacama Cosmology Telescope (ACT, Aiola *et al.*, 2020) is a ground-based CMB experiment, which improves the accuracy of *Planck* at small angular scales (high ℓ). While full MCMC analyses of *Planck* data do not show a preference for EDE, analyses of ACT data have shown a $2 - 3\sigma$ preference for EDE over ΛCDM (Hill *et al.*, 2022; Smith *et al.*, 2022). For the combined data set of ACT DR 4, large-scale *Planck* TT (which is similar to WMAP data) *Planck* lensing, and BAO from SDSS and BOSS, Hill *et al.* (2022) find $f_{\text{EDE}} = 0.091^{+0.020}_{-0.036}$ and $H_0 = 74.2^{+1.9}_{-2.1}$. The preference for EDE is driven by a residual pattern in low- ℓ ACT EE and TE polarization data. It is still unclear whether this pattern is physical or due to systematics.

The South Pole Telescope (SPT, Dutcher *et al.*, 2021) reaches a similar precision as ACT albeit with a slightly more restricted multipole range. Smith *et al.* (2022); La Posta *et al.* (2022) find that SPT data does not show strong evidence for EDE but due to the large error bar is compatible with both the *Planck* and ACT results.

Interestingly, the constraints on the EDE critical redshift, z_c , from *Planck* and SH0ES differ from the ones obtained by data sets including ACT or including SPT: While *Planck*, BAO and SH0ES prefer EDE to be important around recombination, $\log_{10}(z_c) = 3.57^{+0.056}_{-0.140}$ (Smith *et al.*, 2020), ACT, low- ℓ *Planck* and BAO do prefer EDE to be important at later times: $\log_{10}(z_c) < 3.36$ (Hill *et al.*, 2022). We will discuss the interesting results from ACT and SPT further in the Conclusions 7 in light of the recent profile likelihood results, which will be the topic of Chapters 4 and 5.

2.7 Other proposed solutions to the Hubble tension

EDE presents one example for a possible solution to the Hubble tension but there are numerous other proposed theoretical models, which could resolve or alleviate the tension. Schöneberg *et al.* (2022) compiled a recent and comprehensive list of ‘contenders’ to solve the tension. We will name a few promising examples of early-type solutions in the following. *Dark radiation*, i.e. extra relativistic relics, can raise the indirectly inferred value of H_0 by raising the effective number

of relativistic degrees of freedom N_{eff} , for example self-interacting dark radiation (e.g. Bashinsky and Seljak, 2004; Baumann *et al.*, 2016), Majoron models (e.g. Escudero and Witte, 2021), early mass-varying neutrino dark energy (Gogoi *et al.*, 2021) or the Weiss-Zumino dark-radiation model (e.g. Aloni *et al.*, 2022; Schöneberg and Franco Abellán, 2022), which evade the N_{eff} constraints from the CMB. *Primordial magnetic fields* can raise H_0 by introducing small-scale baryon-density inhomogeneities, which change the time of recombination (e.g. Jedamzik and Pogosian, 2020). *Early modified gravity* theories can for example contain a scalar field, which is non-minimally coupled to gravity, e.g. the model considered in Braglia *et al.* (2021) reduces to the Rock'n'Roll (Agrawal *et al.*, 2019); other examples are gravity theories based on Horndeski gravity (Zumalacarregui, 2020), a time-varying Newton's constant (Ballesteros *et al.*, 2020; Braglia *et al.*, 2020a) or a early gravity transition (Benevento *et al.*, 2022). A *varying electron mass* can shift the time of recombination (similar to the primordial magnetic fields) and as a consequence increase H_0 (e.g. Sekiguchi and Takahashi, 2021).

Chapter 3

Statistics of Cosmological Parameter Inference

This chapter follows closely Workman et al. (2022), their ch. 38, Gross (2018), Verde (2007), and Lista (2016).

Summary: In this chapter, we will sketch the statistical methods that will be used in chapters 4 to 6. We will need methods from both frequentist and Bayesian statistics. We introduce parameter estimators in Sec. 3.1, Bayes' theorem in Sec. 3.2, the treatment of nuisance parameters in Sec. 3.3 and frequentist as well as Bayesian interval construction in Secs. 3.4 and 3.5, respectively.

3.1 Parameter estimators

Suppose we conduct one or several experiments and obtain data, \mathbf{x} , in order to test a *hypothesis*, H . A hypothesis is a proposed explanation for the data, which needs to be testable. The hypothesis can be that the universe can be described by a (cosmological) model with parameters $\boldsymbol{\theta} = (\theta_1, \dots, \theta_N)$. One typically distinguishes between the *null hypothesis*, H_0 , e.g. the Universe is described by the Λ CDM model, and an alternative hypothesis, H_1 , e.g. the Universe is described by Λ CDM and Early Dark Energy (EDE, see Ch. 3)¹. The measurement data, $\mathbf{x} = (x_1, \dots, x_M)$, are considered as random variables, which follow a *probability density function* (p.d.f.), $f(\mathbf{x}|\boldsymbol{\theta})$, for given parameters of the model, $\boldsymbol{\theta}$. For a continuous random variable,

$$P(\mathbf{x} < \mathbf{x}_0 < \mathbf{x} + d\mathbf{x} | H(\boldsymbol{\theta})) = f(\mathbf{x}|\boldsymbol{\theta})d\mathbf{x} \quad (3.1)$$

is the probability that the outcome of the measurement, \mathbf{x}_0 , lies between \mathbf{x} and $\mathbf{x} + d\mathbf{x}$ for given parameters $\boldsymbol{\theta}$. Once we have obtained the data from the experiment, we can compute the probability, P , of the data, \mathbf{x} , for a given hypothesis, H , which is the *likelihood*:

$$\mathcal{L}(\mathbf{x}|\boldsymbol{\theta}) = P(\mathbf{x}|H(\boldsymbol{\theta})). \quad (3.2)$$

The dependence on the data, \mathbf{x} is often dropped, since the likelihood is always computed with respect to a fixed (measured) data set. The likelihood quantifies the agreement of the hypothesis with the data: the larger \mathcal{L} , the better the agreement with the data. Note that the likelihood itself is not a probability distribution since it is always computed for fixed \mathbf{x} . Due to the properties of \mathcal{L} , it is often more convenient to work with the logarithm of the likelihood $\ln(\mathcal{L})$. In the following, we will discuss two *point estimators* for the parameters of the model $\boldsymbol{\theta}$ following Workman *et al.* (2022).

3.1.1 Maximum likelihood estimator

The *maximum likelihood* (ML) estimators $\hat{\boldsymbol{\theta}}$ for $\boldsymbol{\theta}$ are defined as the values that give the maximum of \mathcal{L} or equivalently $\ln \mathcal{L}$:

$$\left. \frac{\partial \ln(\mathcal{L})}{\partial \theta_i} \right|_{\boldsymbol{\theta}=\hat{\boldsymbol{\theta}}} = 0. \quad (3.3)$$

The ML estimator has the important property that it is invariant under a change of parameters $\boldsymbol{\theta}$ to $\boldsymbol{\psi}(\boldsymbol{\theta})$, i.e. the ML estimator $\hat{\boldsymbol{\theta}}$ transforms to $\boldsymbol{\psi}(\hat{\boldsymbol{\theta}})$.

3.1.2 Least squares estimator

The *least squares* (LS) estimator is based on the χ^2 -function:

$$\chi^2(\boldsymbol{\theta}) = \sum_{i,j} [x^i - \mu^i(\boldsymbol{\theta})]^T C_{ij}^{-1} [x^j - \mu^j(\boldsymbol{\theta})], \quad (3.4)$$

¹ H_0 is not the Hubble constant in this chapter.

where $\mathbf{x} = (x_1, \dots, x_M)$ are realizations of the data, e.g. the galaxy power spectrum $P(k)$ in bins of k , and $\boldsymbol{\mu}(\boldsymbol{\theta})$ is a model of the data, e.g. the power spectrum computed with a Boltzmann solver assuming the cosmological parameters $\boldsymbol{\theta}$. C_{ij} is the *covariance matrix*, which contains the *variance* of the data on the diagonal, $\sigma_i = C_{ii}$, and the correlations on the off-diagonal elements. The covariance matrix typically needs to be estimated from the data or simulations. We assume here that the covariance matrix does not depend on the parameters. The LS estimator is defined as the values of $\boldsymbol{\theta}$ that minimize the χ^2 :

$$\left. \frac{\partial \chi^2}{\partial \theta_i} \right|_{\boldsymbol{\theta}=\hat{\boldsymbol{\theta}}} = 0. \quad (3.5)$$

If there are no correlations among the data, i.e. the different x_i are independent, the χ^2 -function simplifies to

$$\chi^2(\boldsymbol{\theta}) = \sum_i \frac{[x_i - \mu_i(\boldsymbol{\theta})]^2}{\sigma_i^2}. \quad (3.6)$$

If the measurements x_i are *Gaussian distributed* and the measurements are independent, the following relation holds between χ^2 and likelihood \mathcal{L} :

$$\chi^2(\boldsymbol{\theta}) = -2 \ln \mathcal{L}(\boldsymbol{\theta}) + \text{const.} \quad (3.7)$$

3.2 Bayes' theorem

While in frequentist statistics probability is only associated with the data, \mathbf{x} , in Bayesian statistics one constructs probability distributions of the parameters, $\boldsymbol{\theta}$, of the model with the help of the *Bayes' theorem*:

$$P(H(\boldsymbol{\theta})|\mathbf{x}) = \frac{P(\mathbf{x}|H(\boldsymbol{\theta})) \cdot P(H(\boldsymbol{\theta}))}{P(\mathbf{x})} = \frac{\mathcal{L}(\mathbf{x}|\boldsymbol{\theta}) \cdot \pi(\boldsymbol{\theta})}{P(\mathbf{x})}, \quad (3.8)$$

where $\mathcal{L}(\mathbf{x}|\boldsymbol{\theta}) = P(\mathbf{x}|H(\boldsymbol{\theta}))$ is the likelihood, $\pi(\boldsymbol{\theta}) = P(H(\boldsymbol{\theta}))$ is the prior, and $P(\mathbf{x})$ is the probability of the data called evidence². All knowledge about the parameters, $\boldsymbol{\theta}$, is encoded in the *posterior*, $P(H|\mathbf{x})$, which corresponds to the probability that the hypothesis, H , is true given the data, \mathbf{x} . One can simply obtain the *degree of belief* or (subjective) probability that $\boldsymbol{\theta}$ lies in a region of parameter space by integrating Eq. (3.8) over this region.

The *prior*, $\pi(\boldsymbol{\theta})$, contains prior information about the distribution of the model parameters, $\boldsymbol{\theta}$. This prior information can come from prior experimental data, e.g. calibration experiments, from simulations, or from theoretical considerations. The choice of $\pi(\boldsymbol{\theta})$, therefore, reflects the analyst's (subjective) degree of belief about the parameters, $\boldsymbol{\theta}$, prior to the experiment. If there is no prior knowledge, which could inform the $\pi(\boldsymbol{\theta})$, a typical choice is a flat prior. However, a

²Since the probability $P(\mathbf{x})$ depends only on the data, \mathbf{x} , it only contributes a constant factor and is not important for all further discussion.

flat prior in the parameters θ , would lead to a non-flat prior in a parametrization $\psi(\theta)$ if ψ is a non-linear function of θ , i.e. the prior – and with that the posterior – is not reparametrization invariant.

3.3 Treatment of nuisance parameters

In cosmological experiments, we are typically interested in constraining cosmological parameters, e.g. the six Λ CDM parameters. However, experimental data most of the time cannot be described fully by the set of cosmological parameters but also instrumental effects, foreground or astrophysical effects need to be taken into account. These effects can introduce additional parameters that have to be determined from a fit to data. These *nuisance parameters*, which one is not immediately interested in but need to be taken into account, will be referred to as ν , as opposed to the parameters of interest, e.g. the cosmological parameters, θ . Of course, also cosmological parameters can be treated as nuisance parameters if one is only interested in a subset of them. As a consequence, the likelihood takes the form $\mathcal{L}(\mathcal{D}|\theta, \nu)$ and the constraining power of the data decreases. We will discuss two common ways to take into account nuisance parameters along the lines of Workman *et al.* (2022).

3.3.1 The profile likelihood

A common way to include nuisance parameters in frequentist statistics is the *profile likelihood*, which is obtained by maximizing the likelihood, $\mathcal{L}(x|\theta, \nu)$, over the nuisance parameters, ν , for fixed parameters of interest, θ :

$$\mathcal{L}_p(x|\theta) := \mathcal{L}(x|\theta, \hat{\nu}(\theta)), \quad (3.9)$$

where $\hat{\nu}(\theta)$ are the values that maximize $\mathcal{L}(x|\theta, \nu)$ for a specific θ , i.e. $\hat{\nu}(\theta)$ is the conditional ML estimate of ν for fixed θ . One says that $\mathcal{L}(x|\theta, \nu)$ is *profiled* over ν . The optimization is typically performed numerically using maximizers/minimizers based on gradient descent or simulated annealing techniques (see Ch. 4).

3.3.2 Marginalization

An alternative to the profile likelihood is the *marginalization*, which is typically used in Bayesian statistics. The marginal posterior is obtained by integrating the posterior, $P(\theta, \nu|x)$, over the nuisance parameters, ν :

$$P_m(\theta|x) := \int P(\theta, \nu|x) d\nu. \quad (3.10)$$

This integration typically cannot be performed analytically and Markov Chain Monte Carlo methods (see Sec. 3.5.1) are applied. Since the posterior is proportional to the prior, $\pi(\theta, \nu)$, the

marginalized posterior takes into account the prior volume of the nuisance parameters, i.e. the marginalization up-weights parameter values θ , which are compatible with a larger range of nuisance parameter, ν .

3.4 Frequentist confidence intervals

In Sec. 3.1 we discussed point estimators, which give an estimate for the ‘best-fit’ parameters. However, in practice in addition to the point estimate one wants to quote an interval that reflects the statistical uncertainty of the measurement. In frequentist statistics, these are referred to as *confidence intervals* and are usually associated with the construction by Neyman (1937), which is further specified by the construction by Feldman and Cousins (1998). In this section, we will assume that the model depends on a single parameter, θ , and the measurement contains a single data point, x , but the results can be extended straightforwardly to the multidimensional case or a case including nuisance parameters by profiling (Sec. 3.3.1).

3.4.1 The Neyman construction

Let’s assume we want to construct a confidence interval for the unknown parameter, θ , by measuring the data, x , which follows the p.d.f. $f(x|\theta)$. The p.d.f. is in general not known analytically and is typically obtained by simulating the expected experimental data for a given parameter θ using *Monte Carlo* techniques (see also Sec. 3.5.1).

To construct the confidence interval by Neyman (1937), we fix the *confidence level* (C.L.), $(1 - \alpha)$, and obtain for a given value of the parameter, θ , a set of possible measurement outcomes $x_1(\theta, \alpha)$ and $x_2(\theta, \alpha)$ such that

$$P(x_1 < x < x_2|\theta) = \int_{x_1}^{x_2} f(x|\theta)dx = 1 - \alpha. \quad (3.11)$$

Typical choices of the C.L. are $\alpha = 0.3173$ corresponding to 68.27% C.L. (typically denoted as 68% C.L. for brevity) and $\alpha = 0.0455$ corresponding to 95.45% C.L. (typically denoted as 95% C.L.).

Repeating the procedure in Eq. (3.11) for a grid of values of the parameter, θ , gives the *confidence belt*, which is illustrated in Fig. 3.1. After measuring a value x_0 in the experiment, one can simply draw a vertical line at $x = x_0$ and the confidence interval for θ at C.L. $(1 - \alpha)$ is defined as the interval $\theta \in [\theta_1, \theta_2]$, for which the line segment $[x_1(\theta, \alpha), x_2(\theta, \alpha)]$ is still intercepted by the line. Eq. (3.11) does not determine the interval $[x_1(\theta, \alpha), x_2(\theta, \alpha)]$ uniquely. Common choices to define the confidence interval uniquely, are to require a central interval, where

$$P(x \leq x_1) = P(x \geq x_2) = \alpha/2, \quad (3.12)$$

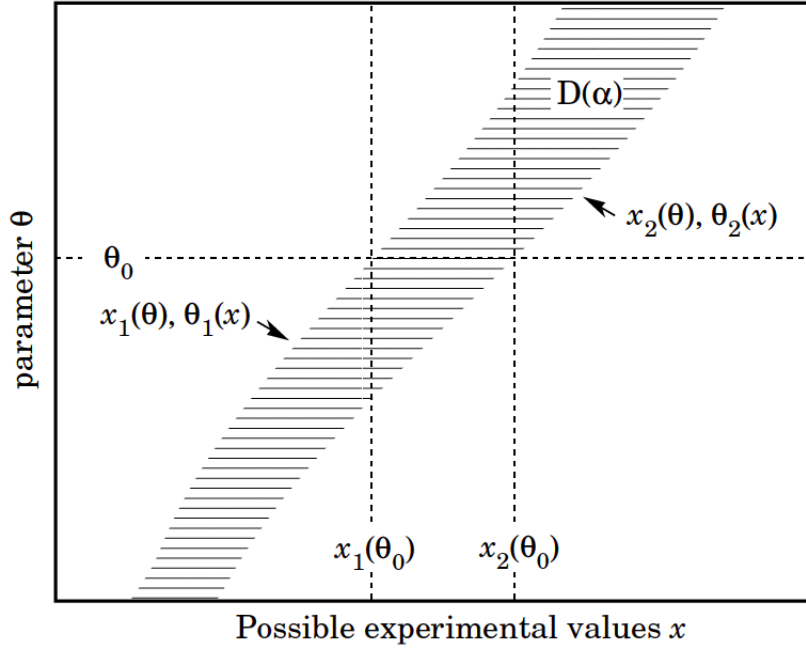


Figure 3.1: Construction of the Neyman confidence belt. For every value of the parameter, θ , a confidence interval, $[x_1(\theta, \alpha), x_2(\theta, \alpha)]$, is constructed via Eq. (3.11). Taken from Workman *et al.* (2022).

or lower/upper limits, where

$$P(x \leq x_{1,2}) = \alpha \quad \text{and} \quad P(x \geq x_{2,1}) = 0. \quad (3.13)$$

If one would repeat the measurement of x a large number of times and for each repetition constructs the confidence interval with C.L. $(1 - \alpha)$ according to above prescription, the such constructed intervals would include the true value of the parameter, θ , a fraction $(1 - \alpha)$ of the experiments. This property is referred to as correct *coverage*. Note that such a ‘probability’ defined by $(1 - \alpha)$ is not meaningful for a fixed confidence interval. To see that this holds, suppose that the true value of θ is θ_0 as indicated in Fig. 3.1. Then, θ_0 lies in $[\theta_1, \theta_2]$ if and only if x lies in $[x_1(\theta_0), x_2(\theta_0)]$ (for $x(\theta)$ being monotonic functions of θ). Hence, it holds that $1 - \alpha = P(x_1(\theta) < x < x_2(\theta)) = P(\theta_2(x) < \theta < \theta_1(x))$.

Gaussian-distributed measurements

We will now consider the special case, where the data parameter, x , follows a Gaussian p.d.f.

$$f(x|\mu, \sigma) = \frac{1}{\sqrt{2\pi\sigma^2}} e^{-\frac{[x-\mu]^2}{2\sigma^2}}, \quad (3.14)$$

where the model is now completely described by the mean, μ , and standard deviation, σ . As a consequence, the construction of the confidence interval simplifies significantly. The integral in

Eq. (3.11) gives:

$$1 - \alpha = \frac{1}{\sqrt{2\pi\sigma^2}} \int_{\mu-\delta}^{\mu+\delta} e^{-\frac{(x-\mu)^2}{2\sigma^2}} = 2\Phi\left(\frac{\delta}{\sigma}\right) - 1, \quad (3.15)$$

where Φ denotes the Gaussian cumulative distribution. δ is the standard deviation in units of σ , e.g. $\delta = 1\sigma$ corresponds to $\alpha = 0.3173$ or $(1 - \alpha) = 0.6827$ and $\delta = 2\sigma$ corresponds to $\alpha = 0.0455$ or $(1 - \alpha) = 0.9545$. Upon performing the experiment and determining x_0 , we can use the relation (3.7) between the likelihood and the χ^2 function for a Gaussian-distributed parameter and obtain

$$\Delta\chi^2 := \chi^2 - \chi_{\min}^2 = -2 \ln \left(\frac{\mathcal{L}(x_0|\mu)}{\mathcal{L}(x_0|\hat{\mu})} \right) = \frac{(x_0 - \mu)^2}{\sigma^2} = \frac{\delta^2}{\sigma^2}, \quad (3.16)$$

where χ_{\min}^2 denotes the minimum of the χ^2 . Hence, in the case of a Gaussian-distributed parameter, we can simply read off the confidence interval for μ by plotting the χ^2 -function and finding the intersection of the curve with $\Delta\chi^2 = \delta^2/\sigma^2$. For example, to obtain the 1σ confidence interval, one determines the intersection of the $\chi^2(x|\mu)$ with $\Delta\chi^2 = 1$, for the 2σ confidence interval with $\Delta\chi^2 = 4$, and so on. The case of a Gaussian p.d.f. simplifies the construction of the confidence interval significantly since the confidence interval can be constructed directly from the data and it is not necessary to determine $f(x|\mu, \sigma)$ from simulations. Even if the likelihood, $\mathcal{L}(x|\mu)$, is non-Gaussian but a reparametrization $y(x)$ exists such that $\mathcal{L}(y|\mu)$ is Gaussian, the simple χ^2 -threshold method can be applied.

Wilks' theorem

Wilks' theorem (Wilks, 1938) states that in the limit of infinite data, the distribution of the test statistic $-\ln[\mathcal{L}(\mathbf{x}_0|\boldsymbol{\theta})/\mathcal{L}(\mathbf{x}_0|\hat{\boldsymbol{\theta}})]$ follows a χ^2 -distribution (3.6). This means that in the limit of a large data set, the approximate formula (3.16) for a Gaussian p.d.f. can be applied, simplifying the confidence interval construction significantly. The intervals obtained with this method are approximate but are often used to quote results since they do not need expensive simulations to estimate the p.d.f. of the data. Cowan *et al.* (2011) extend Wilks' theorem to more than one parameter and give approximate formula for the computation.

Wilks' theorem only applies in the case when the true value of the parameter is far away from the boundary of the parameter space. If this is the case, the Feldman-Cousins prescription needs to be used, which is discussed in the next section.

3.4.2 The Feldman-Cousins prescription

The *Feldman-Cousins prescription* is a special case of the Neyman construction, which shows improved behaviour in the vicinity of a physical boundary, i.e. a boundary of parameter space outside of which the parameter is not defined. We will consider the case where $\theta \geq 0$ (for example

if θ corresponds to a mass or a fraction). Feldman and Cousins (1998) point out that if the analysts of an experiment decide prior to conducting the experiment whether they want to quote an upper limit or a central confidence interval for θ according to Neyman's construction, then the correct coverage is ensured. However, if the analysts make this decision based on the outcome of the experiment, referred to as 'flip-flopping', this can lead to *over-* or *undercoverage*. Undercoverage (overcoverage) refers to confidence intervals, which – upon repetition of the experiment – contain the true parameter less (more) than a fraction $(1 - \alpha)$ of the times. While overcoverage is not as problematic as undercoverage and often regarded as conservatism, undercoverage is regarded as a serious flaw.

To ensure the correct coverage, Feldman and Cousins (1998) suggest an alternative to the central confidence interval (Eq. 3.12) and upper/lower limit (Eq. 3.13). To uniquely define the intervals $[x_1, x_2]$, they suggest an ordering principle based on the likelihood ratio:

$$R(x|\theta) = \frac{f(x|\theta)}{f(x|\hat{\theta})}, \quad (3.17)$$

where $f(x|\theta)$ is the p.d.f. of the data, x , which typically needs to be inferred from simulations and $\hat{\theta}$ is the ML estimate for θ , i.e. the value of θ that maximizes $\mathcal{L}(x|\theta)$ for the hypothetically observed value x (see Sec. 3.1.1). For every value of θ , the interval $[x_1(\theta, \alpha), x_2(\theta, \alpha)]$ at C.L. $(1 - \alpha)$ is defined such that

$$\int_{x_1}^{x_2} f(x|\theta)dx = 1 - \alpha \quad \text{and} \quad R(x_1|\theta) = R(x_2|\theta). \quad (3.18)$$

The ordering principle based on the likelihood ratio R in Eq. (3.18) defines the Neyman confidence belt uniquely. It transitions smoothly from a central confidence interval (Eq. 3.12) for $\theta \gg 0$ to an upper confidence interval (Eq. 3.13) for $\theta \gtrsim 0$. Once the Neyman confidence belt is constructed, one can read off the confidence interval $[\theta_1, \theta_2]$ for the measured x_0 as in Sec. 3.4.1.

Gaussian-distributed measurements with boundary at the origin

For a Gaussian p.d.f. (3.14), the denominator in Eq. (3.17) simplifies significantly. Since $\hat{\mu} = x$ for $x \geq 0$ and $\hat{\mu} = 0$ for $x < 0$,

$$f(x|\hat{\mu}, \sigma) = \begin{cases} \frac{1}{\sqrt{2\pi\sigma^2}} & \text{for } x \geq 0, \\ \frac{1}{\sqrt{2\pi\sigma^2}} e^{x^2/(2\sigma^2)} & \text{for } x < 0. \end{cases} \quad (3.19)$$

Therefore, the likelihood ratio (3.17) becomes

$$R(x|\mu) = \begin{cases} e^{-(x-\mu)^2/2} & \text{for } x \geq 0, \\ e^{x\mu - \mu^2/2} & \text{for } x < 0. \end{cases} \quad (3.20)$$

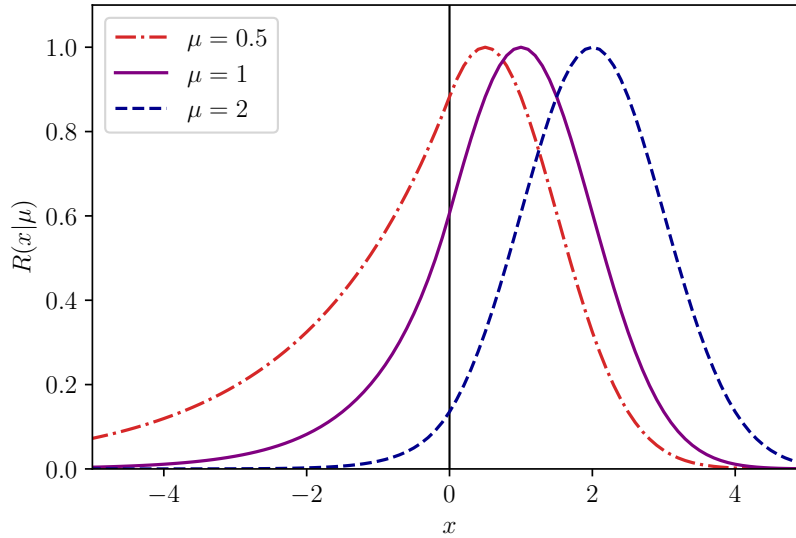


Figure 3.2: Likelihood ratio $R(x|\mu)$ as defined in Eq. (3.20) for different choices of the mean, μ , in units of the standard deviation, σ , i.e. $\sigma = 1$.

The likelihood ratio for the Gaussian case is shown in Fig. 3.2 for $\sigma = 1$ and different choices of μ . $R(x|\mu)$ peaks at $x = \mu$ and gets more asymmetric around the peak the closer μ approaches zero.

For a given C.L. $(1-\alpha)$, mean, μ , and standard deviation, σ , the Feldman-Cousins prescription for the confidence belt in Eq. (3.18) can be solved numerically. For the Gaussian case, Eq. (3.18) becomes:

$$\int_{x_1}^{x_2} f(x|\mu, \sigma) dx = 1 - \alpha \quad \text{and} \quad R(x_1|\mu) = R(x_2|\mu). \quad (3.21)$$

In practice, μ and σ need to be obtained from (Monte-Carlo) simulations of the data. In the limit of a large data set, Wilks' theorem (Wilks, 1938, see Sec. 3.4.1) is often applied as an approximate method to obtain an estimate for μ and σ , i.e. $\mu = x_0$ and σ can be obtained from Eq. (3.16).

With μ and σ determined, the p.d.f. $f(x|\mu, \sigma)$ is fixed and the set of two Eqs. (3.21) can be solved numerically for $x_1(\mu)$ and $x_2(\mu)$. The interval $[x_1(\mu), x_2(\mu)]$ for a grid of values in μ gives the Neyman confidence belt. Fig. 3.3 shows the Neyman confidence belt in units of σ (i.e. $\sigma = 1$) for two different C.L.s. The confidence belt smoothly transforms from a central interval at high values of x to an upper limit at low values of x while ensuring the correct coverage of the interval.

After measuring a value x_0 , the confidence interval for μ can be obtained by inverting the functions $\mu(x_1)$ and $\mu(x_2)$ to find the interval $[\mu_1, \mu_2]$. The resulting confidence intervals are shown in Tab. 3.1 for different measurements, x_0 (c.f. Tab. X in Feldman and Cousins, 1998).

Table 3.1: Confidence intervals for the mean, μ , of a Gaussian p.d.f. constructed with the Feldman-Cousins prescription as a function of the measured mean, x_0 , for 68.27% C.L. and 95.45% C.L. in units of σ (i.e. $\sigma = 1$).

x_0	68.27% C.L.	95.45% C.L.	x_0	68.27% C.L.	95.45% C.L.
-1.5	[0.01, 0.12]	[0.00, 0.84]	0.8	[0.15, 1.80]	[0.00, 2.80]
-1.4	[0.01, 0.15]	[0.00, 0.89]	0.9	[0.00, 1.90]	[0.00, 2.90]
-1.3	[0.01, 0.17]	[0.00, 0.95]	1.0	[0.24, 2.00]	[0.00, 3.00]
-1.2	[0.01, 0.20]	[0.00, 1.01]	1.1	[0.30, 2.10]	[0.00, 3.10]
-1.1	[0.01, 0.23]	[0.00, 1.07]	1.2	[0.35, 2.20]	[0.00, 3.20]
-1.0	[0.01, 0.27]	[0.00, 1.14]	1.3	[0.42, 2.30]	[0.00, 3.30]
-0.9	[0.01, 0.32]	[0.00, 1.21]	1.4	[0.49, 2.40]	[0.00, 3.40]
-0.8	[0.01, 0.37]	[0.00, 1.29]	1.5	[0.56, 2.50]	[0.00, 3.50]
-0.7	[0.01, 0.43]	[0.00, 1.36]	1.6	[0.64, 2.60]	[0.00, 3.60]
-0.6	[0.01, 0.49]	[0.00, 1.45]	1.7	[0.72, 2.70]	[0.01, 3.70]
-0.5	[0.01, 0.56]	[0.00, 1.53]	1.8	[0.81, 2.80]	[0.11, 3.80]
-0.4	[0.01, 0.64]	[0.00, 1.62]	1.9	[0.90, 2.90]	[0.21, 3.90]
-0.3	[0.01, 0.72]	[0.00, 1.71]	2.0	[1.00, 3.00]	[0.31, 4.00]
-0.2	[0.01, 0.81]	[0.00, 1.81]	2.1	[1.10, 3.10]	[0.41, 4.10]
-0.1	[0.01, 0.90]	[0.00, 1.90]	2.2	[1.20, 3.20]	[0.50, 4.20]
0.0	[0.01, 1.00]	[0.00, 2.00]	2.3	[1.30, 3.30]	[0.58, 4.30]
0.1	[0.01, 1.10]	[0.00, 2.10]	2.4	[1.40, 3.40]	[0.66, 4.40]
0.2	[0.01, 1.20]	[0.00, 2.20]	2.5	[1.50, 3.50]	[0.74, 4.50]
0.3	[0.01, 1.30]	[0.00, 2.30]	2.6	[1.60, 3.60]	[0.81, 4.60]
0.4	[0.01, 1.40]	[0.00, 2.40]	2.7	[1.70, 3.70]	[0.89, 4.70]
0.5	[0.03, 1.50]	[0.00, 2.50]	2.8	[1.80, 3.80]	[0.96, 4.80]
0.6	[0.00, 1.60]	[0.00, 2.60]	2.9	[1.90, 3.90]	[1.04, 4.90]
0.7	[0.11, 1.70]	[0.00, 2.70]	3.0	[2.00, 4.00]	[1.12, 5.00]

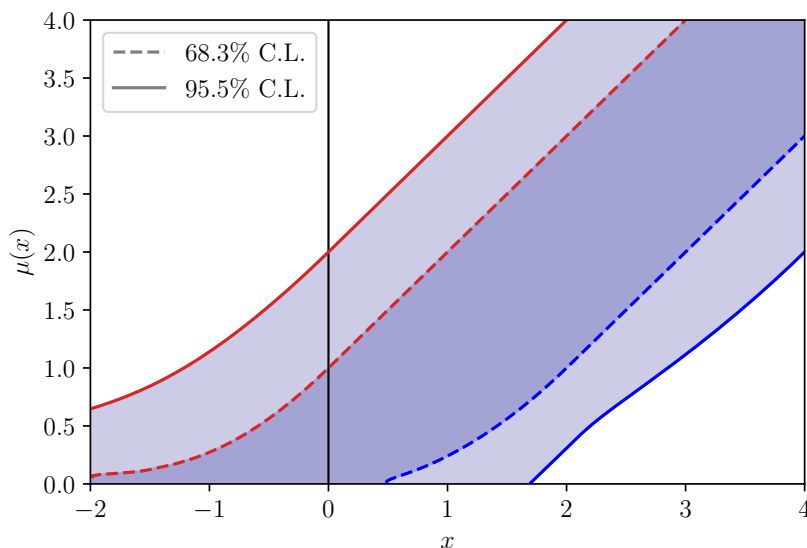


Figure 3.3: Neyman confidence belt constructed with the Feldman-Cousins method for a Gaussian p.d.f. (Eq. 3.21) with mean, μ , in units of standard deviation, σ , at 68.27% C.L. (dashed line) and 95.45% C.L. (solid line). The shaded area between $x_1(\mu)$ (red) and $x_2(\mu)$ (blue) gives the confidence belt.

Frequentist confidence intervals are rarely used to quote results in cosmology. For an (incomplete) list of examples of profile-likelihood analyses in cosmology see Hamann (2012); Hannestad (2000); Yèche *et al.* (2006); Ade *et al.* (2014b); Henrot-Versillé *et al.* (2016); Campeti *et al.* (2022); Campeti and Komatsu (2022); Hadzhiyska *et al.* (2023). Results on cosmological parameters are typically reported as Bayesian credible intervals, which are described in the next section.

3.5 Bayesian credible intervals

Bayesian confidence intervals or *credible intervals*, $[\theta_1, \theta_2]$, at a confidence level $(1 - \alpha)$ give the degree of belief that the true value of the parameter θ lies within the interval with a probability of $(1 - \alpha)$. The credible interval, $[\theta_1, \theta_2]$, can be obtained by integration over the posterior, which is related to the likelihood via Bayes theorem (3.8). In the simple one-dimensional case, the credible interval is given by

$$1 - \alpha = \int_{\theta_1}^{\theta_2} P(\theta|x) d\theta. \quad (3.22)$$

or in the multidimensional case for some volume V :

$$1 - \alpha = \int_V P(\boldsymbol{\theta}|x) d\boldsymbol{\theta}. \quad (3.23)$$

Similar to the frequentist confidence interval, common choices for the credible interval are central intervals or upper/lower limits. The integral in Eq. (3.23) does not have an analytic solution in general and is typically solved using Monte Carlo methods, which will be discussed in the next section following Verde (2007).

3.5.1 Markov Chain Monte Carlo

Monte-Carlo sampling is a brute-force way of sampling the parameter space, i.e. calculating the posterior in Eq. (3.23) for random parameter combinations in order to construct the parameter credible intervals. In order to get an accurate estimate of the posterior, one needs to compute the likelihood sufficiently often, which makes this method computationally very expensive, especially when many parameters are involved. A refinement of this method is the so-called Markov Chain Monte Carlo (MCMC). Instead of sampling the parameter space uniformly at random, the MCMC focuses on the most interesting regions of the parameter space, i.e. regions with non-negligible values of the likelihood.

A simple example of an MCMC algorithm is the *Metropolis-Hastings algorithm* (Metropolis *et al.*, 1953; Hastings, 1970). It samples the multi-dimensional parameter space with fixed step size, s , in a Markov chain according to the following prescription:

1. The current position in parameter space is ϑ_n with likelihood $\mathcal{L}(\mathbf{x}|\vartheta_n)$, where \mathbf{x} is the measured data.
2. Propose a move with random direction \mathbf{e}_n and fixed step size, s .
3. Compute the likelihood, $\mathcal{L}(\mathbf{x}|\vartheta_n + s\mathbf{e}_n)$:
 - (a) If $\mathcal{L}(\mathbf{x}|\vartheta_n + s\mathbf{e}_n) > \mathcal{L}(\mathbf{x}|\vartheta_n)$, then accept the step and $\vartheta_{n+1} = \vartheta_n + s\mathbf{e}_n$.
 - (b) If $\mathcal{L}(\mathbf{x}|\vartheta_n + s\mathbf{e}_n) \leq \mathcal{L}(\mathbf{x}|\vartheta_n)$, then draw a random number from a uniform distribution $a \in [0, 1]$: If $\mathcal{L}(\mathbf{x}|\vartheta_n + s\mathbf{e}_n) > a \cdot \mathcal{L}(\mathbf{x}|\vartheta_n)$, then accept the proposal and $\vartheta_{n+1} = \vartheta_n + s\mathbf{e}_n$, otherwise reject proposal and $\vartheta_{n+1} = \vartheta_n$.

There are several free choices that need to be tuned in that algorithm, e.g. the step size, s , and the start values of the chains. To sufficiently sample the parameter space one runs several chains (about 4-10) with many steps ($10^4 - 10^6$) and discards the first fraction of steps, the so-called *burn-in*.

The chains are said to *converge* when they spend a sufficiently long time close to one set of parameters, which is likely close to the mean of the parameters. Apart from convergence, also a good *mixing* of the chains is important, i.e. a good exploration of the likelihood surface. A commonly used convergence and mixing criterion is the *Gelman-Rubin criterion*. For M chains with N steps each after burn-in, the Gelman-Rubin ratio is defined as:

$$R = \frac{\frac{N-1}{N}W + B \left(1 + \frac{1}{M}\right)}{W}, \quad (3.24)$$

which is a fraction of the variance within the chains defined as

$$W = \frac{1}{M(N-1)} \sum_{m=1}^M \sum_{n=1}^N (\boldsymbol{\vartheta}_n^{(m)} - \bar{\boldsymbol{\vartheta}}^{(m)})^2 \quad (3.25)$$

and the variance between the chains defined as

$$B = \frac{1}{M-1} \sum_{m=1}^M (\bar{\boldsymbol{\vartheta}}^{(m)} - \bar{\boldsymbol{\vartheta}})^2. \quad (3.26)$$

where

$$\bar{\boldsymbol{\vartheta}}^{(m)} = \frac{1}{N} \sum_{n=1}^N \boldsymbol{\vartheta}_n^{(m)} \quad \text{and} \quad \bar{\boldsymbol{\vartheta}} = \frac{1}{NM} \sum_{m=1}^M \sum_{n=1}^N \boldsymbol{\vartheta}_n^{(m)} \quad (3.27)$$

are the mean of the m -th chain and the mean of all chains, respectively. A common choice of the convergence criterion is to require $R - 1 < 0.1$ for all sampled parameters, but much stricter $R - 1$ are also often used. After the chains have converged, the posterior can be computed as a function of the step counts in each cell in parameter space. The results are typically quoted in the form ‘mean $\pm 1\sigma$ ’ and illustrated as contour plots. Since the MCMC does not sample the parameter space very finely, the estimate for the best-fitting parameters is typically poor.

Chapter 4

New Constraint on Early Dark Energy using the Profile Likelihood

The content of this chapter has been published as Herold, Ferreira, and Komatsu (2022).

Abstract: A dark energy-like component in the early Universe, known as early dark energy (EDE), is a proposed solution to the Hubble tension. Currently, there is no consensus in the literature as to whether EDE can simultaneously solve the Hubble tension and provide an adequate fit to the data from the cosmic microwave background (CMB) and large-scale structure of the Universe. In this work, we deconstruct the current constraints from the *Planck* CMB and the full-shape clustering data of the Baryon Oscillation Spectroscopic Survey (BOSS) to understand the origin of different conclusions in the literature. We use two different analyses, a grid sampling and a profile likelihood, to investigate whether the current constraints suffer from volume effects upon marginalization and are biased towards some values of the EDE fraction, f_{EDE} . We find that the f_{EDE} allowed by the data strongly depends on the particular choice of the other parameters of the model and that several choices of these parameters prefer larger values of f_{EDE} than in the Markov Chain Monte Carlo analysis. This suggests that volume effects are the reason behind the disagreement in the literature. Motivated by this, we use a profile likelihood to analyze the EDE model and compute a confidence interval for f_{EDE} , finding $f_{\text{EDE}} = 0.072 \pm 0.036$ (68% C.L.). Our approach gives a confidence interval that is not subject to volume effects and provides a powerful tool to understand whether EDE is a possible solution to the Hubble tension.

4.1 Introduction

Measurements of the Hubble constant, H_0 , the present-day expansion rate of the Universe, obtained with different techniques show a discrepancy known as the ‘‘Hubble tension’’ (Bernal *et al.*, 2016). Indirect measurements, which depend on the assumption of a cosmological model, yield systematically lower values of H_0 than direct measurements, which do not or only weakly depend on the assumption of a cosmological model.

The most significant tension is seen between the (indirect) inference of H_0 from the cosmic microwave background (CMB) data of the *Planck* mission assuming a flat Λ Cold Dark Matter (Λ CDM) cosmological model, $H_0 = 67.37 \pm 0.54$ km/s/Mpc (Aghanim *et al.*, 2020b), and the (direct) local inference from Cepheid-calibrated Type Ia supernovae of the SHOES project, $H_0 = 73.04 \pm 1.04$ km/s/Mpc (Riess *et al.*, 2022). The statistical significance of the tension is 5σ . Throughout this chapter, we quote uncertainties at the 68 % confidence level (C.L.), unless noted otherwise.

This tension could hint at new physics beyond the flat Λ CDM model. One of the proposed models to alleviate the tension is early dark energy (EDE, Poulin *et al.*, 2018, 2019; Smith *et al.*, 2020). In this model, the Λ CDM cosmology is extended to include a dark energy-like component in the pre-recombination era, which reduces the size of the sound horizon and increases H_0 (Bernal *et al.*, 2016). EDE is typically parameterized by three parameters: the initial value of the EDE field (θ_i), its maximum fractional energy density (f_{EDE}) and the critical redshift (z_c) at which this maximum fraction is reached.

EDE was shown to reduce the tension between the values of H_0 (Poulin *et al.*, 2019; Smith *et al.*, 2020) inferred from the CMB data of *Planck* (Aghanim *et al.*, 2016), the baryon acoustic oscillation (BAO) and the redshift-space distortion data of the Baryon Oscillation Spectroscopic Survey (BOSS; Alam *et al.*, 2017), the BAO measurements from the 6-degree Field Galaxy Survey (6dFGS; Beutler *et al.*, 2011) and Sloan Digital Sky Survey Main Galaxy Sample (SDSS MGS; Ross *et al.*, 2015), the Pantheon supernova sample (Scolnic *et al.*, 2022), and the direct measurement by the SHOES collaboration (Riess *et al.*, 2019). They find $f_{\text{EDE}} = 0.107^{+0.035}_{-0.030}$, which gives $H_0 = 71.49 \pm 1.20$ km/s/Mpc.

However, it was pointed out in Hill *et al.* (2020) that introducing EDE leads to a higher amplitude of matter density fluctuations parametrized by Ω_m and σ_8 , worsening the so-called σ_8 -tension. They showed that including further large-scale structure (LSS) probes such as Dark Energy Survey (DES; Abbott *et al.*, 2018b), Kilo-Degree Survey (KiDS-VIKING; Hildebrandt *et al.*, 2020) and Hyper Suprime-Cam (HSC; Hikage *et al.*, 2019), which are particularly sensitive to Ω_m and σ_8 , weakens the evidence for EDE. When including all probes but H_0 from SHOES, their analysis yields an upper limit of $f_{\text{EDE}} < 0.06$ at 95% C.L. A similar constraint of $f_{\text{EDE}} < 0.072$ at 95% C.L. (with $f_{\text{EDE}} = 0.025^{+0.006}_{-0.025}$) is obtained when employing the full shape of the galaxy power spectrum combined with the BAO data of BOSS Data Release 12 (DR 12) galaxies along with the *Planck* data (Ivanov *et al.*, 2020a). Concurrently, a similar analysis from D’Amico *et al.* (2021b) found $f_{\text{EDE}} < 0.08$ at 95% C.L. for the same data set and additionally

including the Pantheon supernova sample. These three papers conclude that EDE does not solve the Hubble tension.

In the analyses of Hill *et al.* (2020), Ivanov *et al.* (2020a), and D’Amico *et al.* (2021b), all three EDE parameters $\{f_{\text{EDE}}, \theta_i, z_c\}$ are varied, which is referred to as the “3-parameter model.” Smith *et al.* (2021) argued that the reason for the small preferred value of f_{EDE} found by them is due to volume effects upon marginalization, and proposed alternative approaches.¹ In particular, they found $f_{\text{EDE}} = 0.072 \pm 0.034$ for the same data set as in Ivanov *et al.* (2020a), when fixing two EDE parameters $\{\theta_i, z_c\}$, which is referred to as the “1-parameter model.” Within the 1-parameter model, they observe that including LSS data decreases the evidence for EDE similar to the 3-parameter model; they relate this tighter constraint on EDE to the lower clustering amplitude preferred by LSS data compared to CMB data. The 1-parameter model was already explored earlier in Niedermann and Sloth (2020) in the context of new EDE.

Currently there is no agreement in the community as to whether EDE can simultaneously solve the Hubble tension and fit all available data sets. A new chapter in this discussion was presented recently: Two groups (Hill *et al.*, 2022; Poulin *et al.*, 2021) reported independently on a $2 - 3\sigma$ preference for EDE when analyzing the model using the CMB data of the Atacama Cosmology Telescope (ACT; Choi *et al.*, 2020). South Pole Telescope data (Dutcher *et al.*, 2021) is consistent with both ACT and *Planck* results (La Posta *et al.*, 2022).

One question that remains open is: What is the reason behind this disagreement? The root of this seems to lie in the Markov Chain Monte Carlo (MCMC) sampling of the three parameters of the EDE model. For $f_{\text{EDE}} = 0$, the EDE model is degenerate with Λ CDM for any choice of θ_i and z_c . Therefore, the parameter volume for $f_{\text{EDE}} = 0$ is larger than for every $f_{\text{EDE}} > 0$. This can lead to a preference for $f_{\text{EDE}} = 0$ in the marginalized posterior, affecting the inferred amount of EDE allowed by the data. On the other hand, fixing some parameters of the model, as for the 1-parameter model, is an incomplete analysis, as stated in Smith *et al.* (2021); the results might depend on the particular choice of the parameters.

In this chapter, we deconstruct the current constraints on the EDE model from the CMB and BOSS full-shape clustering data. Our goal is to understand where the disagreement in the literature comes from and to check if volume effects are indeed present. In particular, we answer the following questions: Is the 3-parameter model affected by the two unconstrained parameters θ_i and z_c or by volume effects? Do the results of the 1-parameter model depend on the particular choice of θ_i and z_c and how well can the results be generalized to the full 3-parameter model? How would the constraints on f_{EDE} change if those effects were eliminated?

To this end, we perform two analyses: a grid sampling and a profile likelihood. With the grid sampling, we explore the parameter space of $\{\theta_i, z_c\}$ by fixing them to a wide range of values and performing the 1-parameter analysis. This analysis shows that higher values of f_{EDE} are consistent with the data, which suggests that the 3-parameter MCMC analysis is affected by volume effects, and that there is a strong dependence of f_{EDE} on the particular choice of $\{\theta_i, z_c\}$.

¹An exploration of volume effects with an averaging method can be found in the appendix of Ivanov *et al.* (2020a).

This makes it difficult to generalize the results of the 1-parameter model. To confirm the presence of volume effects, we perform a frequentist-statistic analysis using a profile likelihood. We find that a considerably larger f_{EDE} is preferred by the data compared to the Bayesian MCMC analysis, confirming that volume effects affect the 3-parameter analysis.

The rest of this chapter is organized as follows. In Section 4.2, we describe the EDE model. In Section 4.3, we deconstruct the current constraints using the grid and the profile likelihood. In Section 4.4, we construct a new confidence interval using the profile likelihood. We discuss the results and conclude in Section 4.5.

4.2 The EDE model

The idea behind early-time solutions to the Hubble tension is to reduce the sound horizon and hence increase the inferred value of H_0 (Bernal *et al.*, 2016). The sound horizon,

$$r_s = \int_{z_*}^{\infty} c_s(z) dz / H(z),$$

where z_* is the redshift of the last scattering surface, $c_s(z)$ the sound speed in the baryon-photon plasma, and $H(z)$ the expansion rate of the Universe, is dominated by contributions near the lower bound of the integral.

EDE (Kamionkowski *et al.*, 2014; Karwal and Kamionkowski, 2016; Caldwell and Devulder, 2018) is an extra component added to the energy density budget near z_* , which increases $H(z)$ and lowers r_s . This can be achieved by a pseudo scalar field, ϕ , which obeys the following requirements: (i) it starts becoming relevant at matter-radiation equality; (ii) it behaves like dark energy at early times; and (iii) its energy density dilutes faster than the matter density after z_* . To model this behavior, the canonical EDE model is given by the potential (Poulin *et al.*, 2018):

$$V(\phi) = V_0 [1 - \cos(\phi/f)]^n, \quad (4.1)$$

where $V_0 = m^2 f^2$, m is the mass of ϕ , and f is the spontaneous symmetry breaking scale.

The parameters of the model can be re-written in terms of the phenomenological parameters $\{f_{\text{EDE}}, \theta_i, z_c, n\}$, where f_{EDE} is the maximum fraction of EDE at the critical redshift z_c , and θ_i is the initial value of the dimensionless field, $\theta \equiv \phi/f$. A larger value of f_{EDE} leads to a higher H_0 . To solve the Hubble tension, it was predicted that $f_{\text{EDE}} \simeq 0.1$ would be necessary (Knox and Millea, 2020).

The EDE field ϕ in a cosmological background with the potential given in Eq. (4.1) behaves like dark energy initially, with the field essentially frozen. Once $H(z)$ becomes smaller than the effective mass $m_{\text{eff}} = d^2V(\phi)/d\phi^2$, ϕ starts decaying and oscillating at the bottom of the potential with an effective, time-averaged equation of state parameter of $\langle w \rangle = (n-1)/(n+1)$. Here, we

choose $n = 3$ as in the previous analyses, which was shown to dilute sufficiently fast to satisfy the requirement (iii) (Poulin *et al.*, 2018; Smith *et al.*, 2020).

4.3 Deconstructing the current constraints on the EDE model

4.3.1 Data and methodology

For our analysis, we use a similar setup as in Ivanov *et al.* (2020a). We combine the following publicly available extensions of the Einstein–Boltzmann solver CLASS (Lesgourgues, 2011; Blas *et al.*, 2011):² CLASS_EDE (Hill *et al.*, 2020), which evolves the EDE field as a pseudo scalar field up to linear order in perturbations; and CLASS-PT (Chudaykin *et al.*, 2020), which is based on the Effective Field Theory (EFT) of LSS (Baumann *et al.*, 2012; Carrasco *et al.*, 2012) and allows to model the galaxy power spectrum up to mildly nonlinear scales. We perform an MCMC inference with MontePython (Brinckmann and Lesgourgues, 2019), using the Metropolis–Hastings algorithm (Metropolis *et al.*, 1953; Hastings, 1970).

Our data set consists of the *Planck* 2018 TT+TE+EE+low ℓ +lensing likelihoods (Aghanim *et al.*, 2020b) along with the BOSS DR 12 full-shape likelihood based on the EFT of LSS presented in Ivanov *et al.* (2020b); D’Amico *et al.* (2020). Note that this is a slightly different data set than in Ivanov *et al.* (2020a) and Smith *et al.* (2021), who also included the BOSS (reconstructed) BAO likelihood. We have checked that including the reconstructed BAO data in addition does not lead to a large change of our conclusions. Recently, there has been an update on the BOSS window function from Beutler and McDonald (2021) that might impact the conclusions in previous analysis cited here. To compare with the published constraints, we do not use the new window functions.

We sample the Λ CDM parameters $\omega_b, \omega_{\text{CDM}}, \theta_s, A_s, n_s, \tau_{\text{reio}}$ assuming flat priors, along with the *Planck* and EFT nuisance parameters. In Section 4.3.2, we assume $f_{\text{EDE}} \in [0.001, 0.5]$, in Sections 4.3.3, 4.4, we assume $\theta_i \in [0.1, 3.1]$ and $\log(z_c) \in [3, 4.3]$. Following the convention of the *Planck* collaboration (Aghanim *et al.*, 2020b), we model the neutrino sector by two massless and one massive neutrino species with $m_\nu = 0.06$ eV.

4.3.2 Grid Sampling

In this section, we perform our first analysis³ to study how much the conclusions of Smith *et al.* (2021) drawn from the 1-parameter model depend on the particular choice of $\theta_i = 2.775$ and

²The code used for this analysis is publicly available at https://github.com/LauraHerold/CLASS-PT_EDE.

³See Sec. 4.6.1 in the supplementary material for some preliminary studies using MCMC techniques.

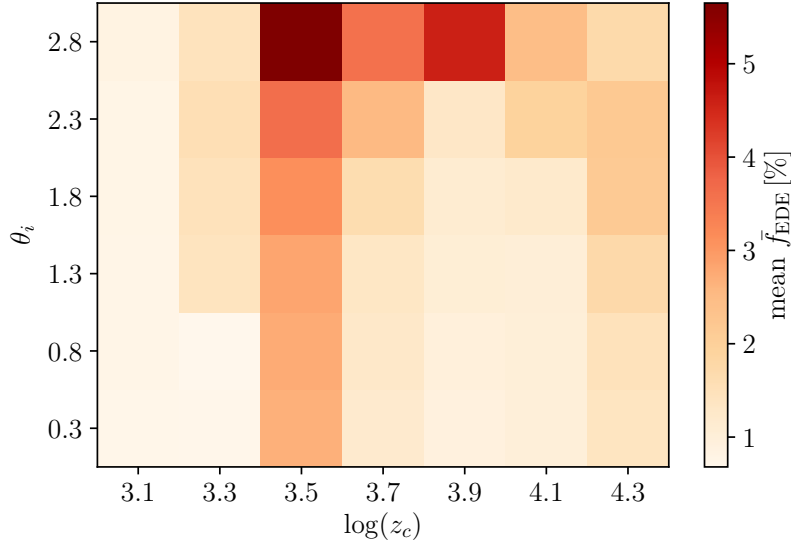


Figure 4.1: Mean values of \bar{f}_{EDE} for different fixed values of θ_i and $\log(z_c)$. Every value in this 6×7 grid is determined by a full MCMC analysis.

$\log(z_c) = 3.569$. An exploration of the effect of θ_i , z_c on cosmological observables can be found in Smith *et al.* (2020); Poulin *et al.* (2018); Lin *et al.* (2019).

The potential problem encountered in the MCMC exploration of the 3-parameter model is a preference for small f_{EDE} due to volume effects upon marginalization over θ_i and z_c . We investigate this problem as follows. To explore the dependence of the f_{EDE} constraints on θ_i and z_c , we run several MCMC inferences, where we keep θ_i and z_c fixed to different values and vary only f_{EDE} . We choose six values in the typical prior range of $\theta_i \in [0.1, 3.1]$ and seven values in the typical prior range of $\log(z_c) \in [3, 4.3]$:

$$\begin{aligned}\theta_i &= \{0.3, 0.8, 1.3, 1.8, 2.3, 2.8\}, \\ \log(z_c) &= \{3.1, 3.3, 3.5, 3.7, 3.9, 4.1, 4.3\}.\end{aligned}$$

Throughout this chapter “log” denotes the logarithm with base 10. This gives a 6×7 grid of MCMC analyses. For each MCMC, we infer the mean fraction of EDE \bar{f}_{EDE} depending on the choice of θ_i and z_c . We run every MCMC until the Gelman-Rubin convergence criterion $R - 1 < 0.1$ is reached. Our results are summarized in Fig. 4.1.

We find that \bar{f}_{EDE} strongly depends on the particular choice of θ_i and $\log(z_c)$. There are choices of θ_i and $\log(z_c)$ that allow for higher f_{EDE} . For example, $\theta_i = 2.8$ and $\log(z_c) = 3.5$ (which is close to the values chosen by Smith *et al.* (2021): $\theta_i = 2.775$, $\log(z_c) = 3.569$), allows for particularly high $f_{\text{EDE}} = 0.057^{+0.027}_{-0.034}$, the highest found in the grid. The authors point out that this choice of $\{\theta_i, z_c\}$ is reasonable since it is obtained from the best-fit cosmology to *Planck* data. However, for $\theta_i = 1.8$ and $\log(z_c) = 3.7$ (which is similar to the mean values found in

Ivanov *et al.* (2020a): $\theta_i = 2.023$, $\log(z_c) = 3.71$), we find $f_{\text{EDE}} = 0.017_{-0.016}^{+0.004}$. This shows that the particular choice of θ_i and $\log(z_c)$ made in Smith *et al.* (2021) is the reason for a higher f_{EDE} than found in Ivanov *et al.* (2020a). We point out that the best fit and mean values quoted in Ivanov *et al.* (2020a) (best-fit values: $\theta_i = 2.734$, $\log(z_c) = 3.52$) correspond to choices of θ_i and $\log(z_c)$ that allow for high and low values of f_{EDE} , respectively.

We also explore the dependence of the best-fit f_{EDE} and the $\Delta\chi^2$ as a function of θ_i and z_c in the supplementary material 4.6.2, finding a similar pattern as in Fig. 4.1. We show that the choice of $\theta_i = 2.8$ and $\log(z_c) = 3.5$, which gives the highest mean and best fit of f_{EDE} , has the smallest χ^2 .

As the constraint on f_{EDE} depends strongly on the particular choice of $\{\theta_i, z_c\}$, the analysis of the 1-parameter model presented in Smith *et al.* (2021) might have been biased. Our result also shows that, if $\{\theta_i, z_c\}$ cannot be constrained, as in the MCMC analysis of the 3-parameter model (Ivanov *et al.*, 2020a), it might lead to misleading constraints on f_{EDE} .

Our grid method is not plagued by volume effects since there is no larger prior volume at $f_{\text{EDE}} = 0$ compared to $f_{\text{EDE}} > 0$ when θ_i and $\log(z_c)$ are fixed. This course-grained exploration of the $\{\theta_i, z_c\}$ parameter space made with the grid shows that higher values of f_{EDE} are allowed for a considerable part of the parameter space and present a good fit to the data. This indicates that volume effects might be present in the 3-parameter MCMC analysis, and that, when this effect is eliminated, the preference for smaller f_{EDE} in the posterior is weakened. Motivated by this, in the next section we perform a frequentist analysis using profile likelihoods, which does not suffer from volume effects.

4.3.3 Profile likelihood

Comparison of the results obtained from Bayesian and frequentist analyses is useful for checking if priors or marginalization affect the results (Cousins, 1995). A profile likelihood is a standard tool in frequentists' statistics. To construct a profile likelihood, one fixes the parameter of interest, i.e. in our case f_{EDE} , to different values and maximizes the likelihood \mathcal{L} (or minimizes $\chi^2 = -2 \ln \mathcal{L}$) with respect to all the other parameters of the model, i.e. all ΛCDM parameters, θ_i and z_c , as well as all the nuisance parameters, for every choice of the parameter of interest (f_{EDE}). The $\Delta\chi^2$ as a function of the parameter of interest is the profile likelihood (see, e.g. Ade *et al.*, 2014b, for an application to the *Planck* data).

For the minimization, we adopt the method used in Schöneberg *et al.* (2022). For every fixed value of f_{EDE} , we first run a long MCMC (with at least 10^4 accepted steps) until the Gelman-Rubin criterion $R - 1 < 0.25$ is reached. This yields a reasonable estimate for the best-fit values and covariance of all the other parameters. Second, we run three small chains with successively decreasing step size (decreasing temperature) and enhanced sensitivity to the likelihood difference. This is done with a slightly modified Metropolis–Hastings algorithm as described in Schöneberg *et al.* (2022). Since they found that in the context of EDE and other solutions to the Hubble ten-

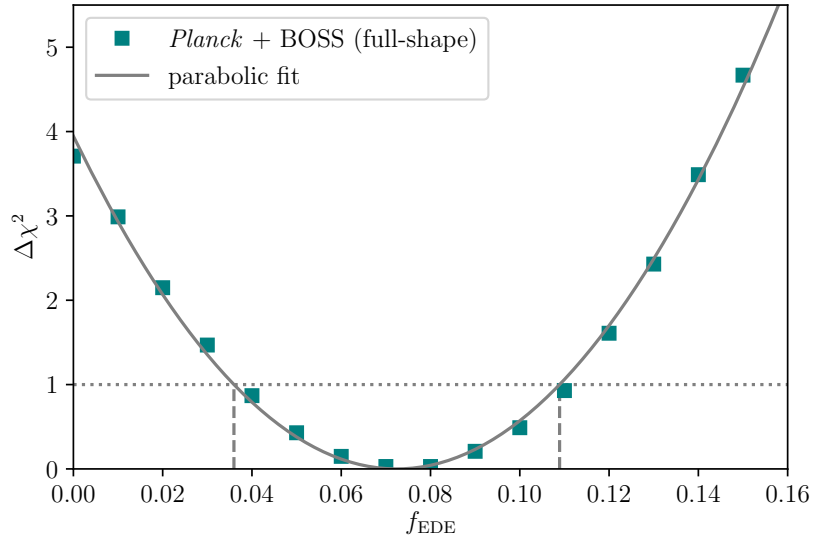


Figure 4.2: Profile likelihood of the fraction of EDE f_{EDE} from the *Planck* CMB and the BOSS full-shape galaxy clustering data. We show $\Delta\chi^2 = -2 \ln(\mathcal{L}/\mathcal{L}_{\text{max}})$, where \mathcal{L}_{max} is the maximum likelihood, (green markers) and a parabola fit (grey line). The confidence interval is constructed using the Feldman–Cousins prescription Feldman and Cousins (1998) (vertical dashed lines). It is indistinguishable from the interval constructed from the intersection of the parabola with $\Delta\chi^2 = 1$ (horizontal dotted line).

sion, this method was less likely to get stuck in local minima than algorithms based on gradient descent such as MIGRAD (James and Roos, 1975), we adopted the same approach.

The results of the minimization are shown as the markers in Fig. 4.2. For a parameter following a Gaussian distribution, one would expect a parabola, which is a good fit for $f_{\text{EDE}} < 0.15$ (grey line). The minimum of the curve is the minimum $\chi^2(f_{\text{EDE}})$, and shows the best-fit value for f_{EDE} . Already from the profile likelihood, one can see that our best-fit value lies near the upper bound $f_{\text{EDE}} < 0.072$ (95% C.L.) of Ivanov *et al.* (2020a). This is a strong indication that the MCMC analysis of the 3-parameter model is plagued by volume effects. The profile likelihood does not suffer from volume effects, since the minimum $\chi^2(f_{\text{EDE}})$ is the same as the maximum likelihood estimate.

We report the best-fit values of all the parameters for $f_{\text{EDE}} = 0, 0.07$ and 0.11 in the supplementary material 4.6.3. We found that the best-fit values of $\{\theta_i, z_c\}$ are approximately constant for all fixed values of f_{EDE} and fluctuate within a few percent around $\log(z_c) = 3.56$ and $\theta_i = 2.75$. Note that these values are very close to the ones adopted in the 1-parameter model in Smith *et al.* (2021).

4.4 Constructing Confidence Intervals: Profile likelihood

To construct confidence intervals from the profile likelihood shown in Fig. 4.2, we use the prescription introduced by Feldman and Cousins (1998), which is suitable for a parameter with a physical boundary like f_{EDE} , which has to lie between 0 and 1. The Feldman–Cousins prescription is based on the likelihood ratio

$$R(x) = \frac{\mathcal{L}(x|\mu)}{\mathcal{L}(x|\mu_{\text{best}})}, \quad (4.2)$$

where x is the observable or measured value (it can take on all possible values for f_{EDE}), μ is the true value of f_{EDE} (which will be read off at the minimum of the parabola), and μ_{best} is the physically allowed value μ for which for a given x the likelihood $\mathcal{L}(x|\mu)$ is maximized; since $\mu_{\text{best}} > 0$, it is $\mu_{\text{best}} = x$ for $x \geq 0$ and $\mu_{\text{best}} = 0$ for $x < 0$. The confidence interval $[x_1, x_2]$ is chosen such that $R(x_1) = R(x_2)$ and

$$\int_{x_1}^{x_2} \mathcal{L}(x|\mu) dx = \alpha, \quad (4.3)$$

where α is the confidence level, e.g. $\alpha = 0.6827$ for 68.27% C.L. To shorten the notation, we denote 68.27% C.L. as 68% C.L. in the remainder of the chapter. For a given μ , the integral is solved numerically and tabulated by Feldman and Cousins (1998). The Feldman–Cousins prescription unambiguously determines whether one parameter should be quoted as an upper/lower limit or as a central confidence interval. Here, we find a central confidence interval at the 68% C.L. By reading off μ at the minimum of the parabola shown in Fig. 4.2, we find $f_{\text{EDE}} = 0.072 \pm 0.036$ ($f_{\text{EDE}} = 0.072^{+0.071}_{-0.060}$ at 95% C.L.).

The upper and lower bounds of the 68% confidence interval are shown in Fig. 4.2, as the vertical dashed lines. They coincide with the confidence intervals constructed by the Neyman prescription (interval between parabola points that intersect with $\Delta\chi^2 = 1$, Neyman, 1937), which is only valid far away from a physical boundary.

4.5 Discussion and conclusion

In this chapter, we used the grid sampling and profile likelihood methods to understand the difference in the constraints on the EDE model reported in the literature (Ivanov *et al.*, 2020a; D’Amico *et al.*, 2021b; Smith *et al.*, 2021), using the *Planck* CMB and the BOSS full-shape galaxy clustering data. With the grid sampling, we showed that the inferred mean and best-fit values of f_{EDE} depend strongly on the values of $\{\theta_i, z_c\}$. This finding is relevant, since the posterior distributions in the full 3-parameter model shown in Ivanov *et al.* (2020a) (their Fig. 5) indicate that θ_i and particularly z_c are poorly constrained by the *Planck* and BOSS data. Also, depending on the particular choice of $\{\theta_i, z_c\}$ made in the 1-parameter model, one could draw different conclusions

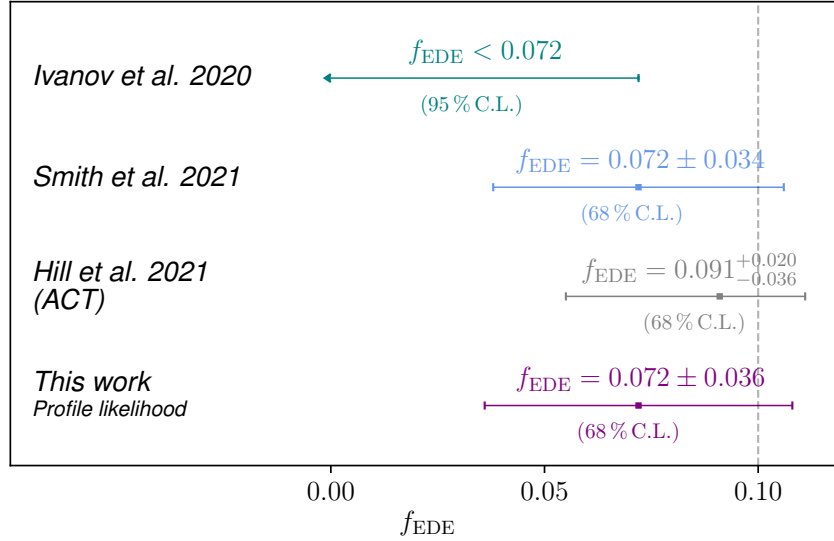


Figure 4.3: Summary of the current constraints on f_{EDE} from the *Planck* CMB and the BOSS full-shape galaxy clustering data by different methods: Ivanov *et al.* (2020a) with an MCMC inference of the 3-parameter model in green (95% C.L.), Smith *et al.* (2021) with an MCMC inference within the 1-parameter model in blue (68% C.L.), and our results obtained with the Feldman–Cousins prescription based on the profile likelihood in purple (68% C.L.). For comparison, we show the recent ACT results in grey (Hill *et al.*, 2022) (68% C.L.). The vertical grey dashed line marks $f_{\text{EDE}} = 0.1$.

about the amount of EDE allowed by the data. The choice made in Smith *et al.* (2021) is an example of a choice that allows for high value of f_{EDE} and therefore a larger effect on H_0 . However, even for the choice $\theta_i = 2.8$ and $\log(z_c) = 3.5$, which gives the highest value of f_{EDE} in our grid method, we find $H_0 = 69.52^{+0.95}_{-1.21}$ km/s/Mpc, which only partially alleviates the Hubble tension.

Based on the hints of the grid analysis, we constructed the profile likelihood for f_{EDE} , which is not subject to volume effects upon marginalization in the MCMC chain. Using the Feldman–Cousins prescription, we constructed the confidence interval, finding $f_{\text{EDE}} = 0.072 \pm 0.036$, providing a new and robust constraint on the EDE model.

In Fig. 4.3, we compare the confidence interval from this work based on the profile likelihood to previous work. For reference, we mark $f_{\text{EDE}} = 0.1$. Our best-fit value, $f_{\text{EDE}} = 0.072$, is at the 95%-confidence upper limit found in Ivanov *et al.* (2020a), which is $f_{\text{EDE}} < 0.072$. This shows that there is an effect in the MCMC analysis that drives the constraint on f_{EDE} closer to zero. The most plausible explanation is volume effects upon marginalization due to the large prior volume in θ_i and z_c when $f_{\text{EDE}} \rightarrow 0$. On the other hand, our best-fit value and the 68% C.L. are similar to those found in Smith *et al.* (2021) with the same central value and only slightly larger confidence interval. Nevertheless, their result was obtained within the 1-parameter model, which has a strong dependence on the particular choice of θ_i and z_c as shown in Section 4.3.2, and cannot be used to

draw conclusions about the full 3-parameter model.

We suggest that the profile likelihood is a more suitable method to analyze the EDE model, and determine f_{EDE} . The confidence intervals obtained through this method do not suffer from volume effects or a reduced parameter space.

4.6 Supplementary material

4.6.1 Preliminary studies using MCMC techniques

As a first step to explore the influence of prior volume effects and the dependence of the results on all parameters of the EDE model, we ran MCMC with MontePython analyses with certain parameters fixed using `getdist` to create the plots (Lewis, 2019). Fig. 4.4 shows the posteriors of different 1-parameter models, corresponding to different positions in the grid of fixed z_c and θ_i values (Fig. 4.1). We find that the inferred values of f_{EDE} and other cosmological parameters like H_0 , σ_8 and ω_c depend strongly on the fixed values of z_c and θ_i . The largest values of f_{EDE} are preferred for $\log(z_c) = 3.5$ and $\theta_i = 2.8$.

Fig. 4.5 shows the posteriors of a ‘2-parameter model’ with f_{EDE} fixed to different values between 0.01 and 0.1 while z_c and θ_i are free to vary. As expected, the higher the fixed value of f_{EDE} , the larger the inferred H_0 , ω_c , σ_8 , and n_s . Moreover, the larger the fixed value of f_{EDE} the stronger the constraints on z_c and θ_i . This illustrates how the prior volume in z_c and θ_i increases when f_{EDE} approaches zero.

4.6.2 Best fit and $\Delta\chi^2$ of grid analysis

The results of the grid analysis, showing the dependence of the best-fit f_{EDE} and the $\Delta\chi^2$ as a function of θ_i and z_c , can be seen in Fig. 4.6.

4.6.3 Best-fit values of the parameters for different cosmologies

In Table 4.1, we show the best-fit parameters obtained with the minimization described in Section 4.3.3 for the Λ CDM cosmology and for EDE cosmologies with fixed f_{EDE} . The first 8 parameters in the table are varied in the MCMC, the last 6 parameters are derived parameters. At the bottom, we quote the minimum χ^2 . The cosmology with fixed $f_{\text{EDE}} = 0.07$ is close to the best fit computed from the minimum of the parabola fit, $f_{\text{EDE}} = 0.11$ is at the higher end of the 68% confidence interval.

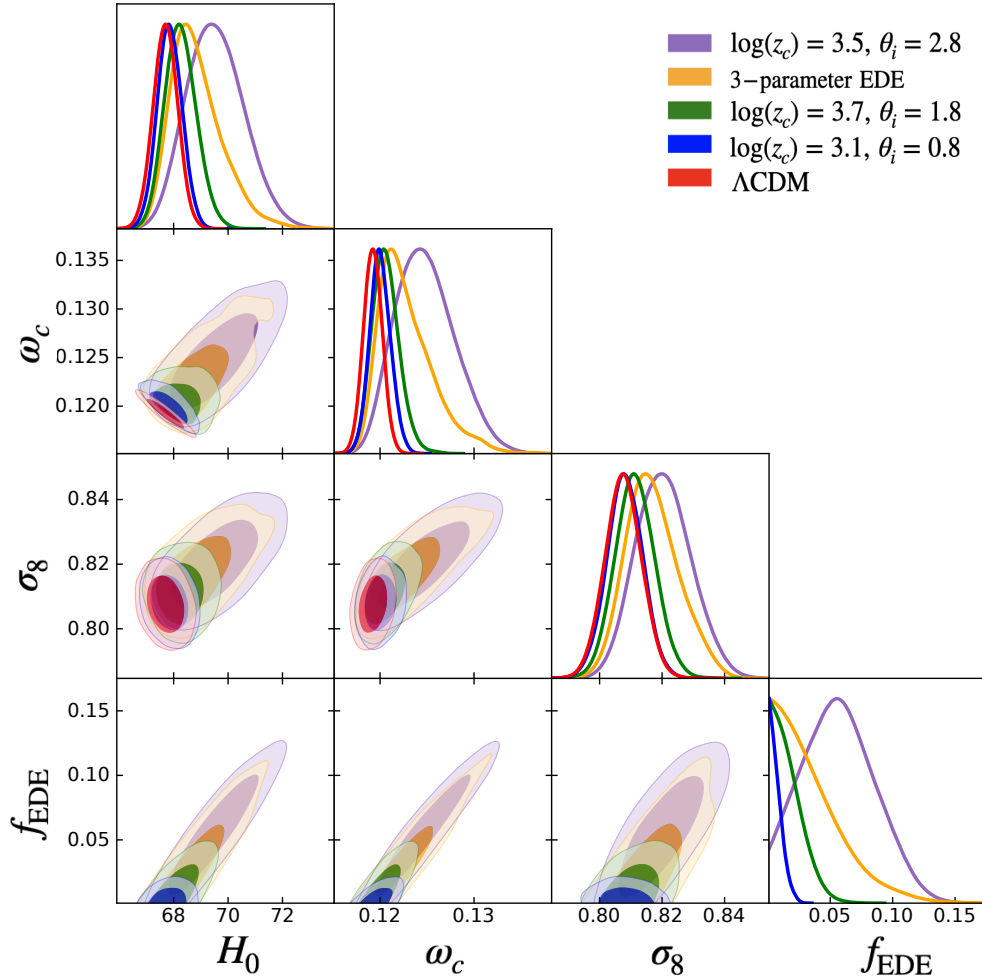


Figure 4.4: Posteriors for 1-parameter EDE models with different choices of the fixed values of z_c and θ_i as indicated in the legend. For comparison, we show the full 3-parameter EDE model (yellow) and the Λ CDM model. The 1-parameter EDE model with $\log(z_c) = 3.5$ and $\theta_i = 2.8$ shows the largest preferred values of f_{EDE} .

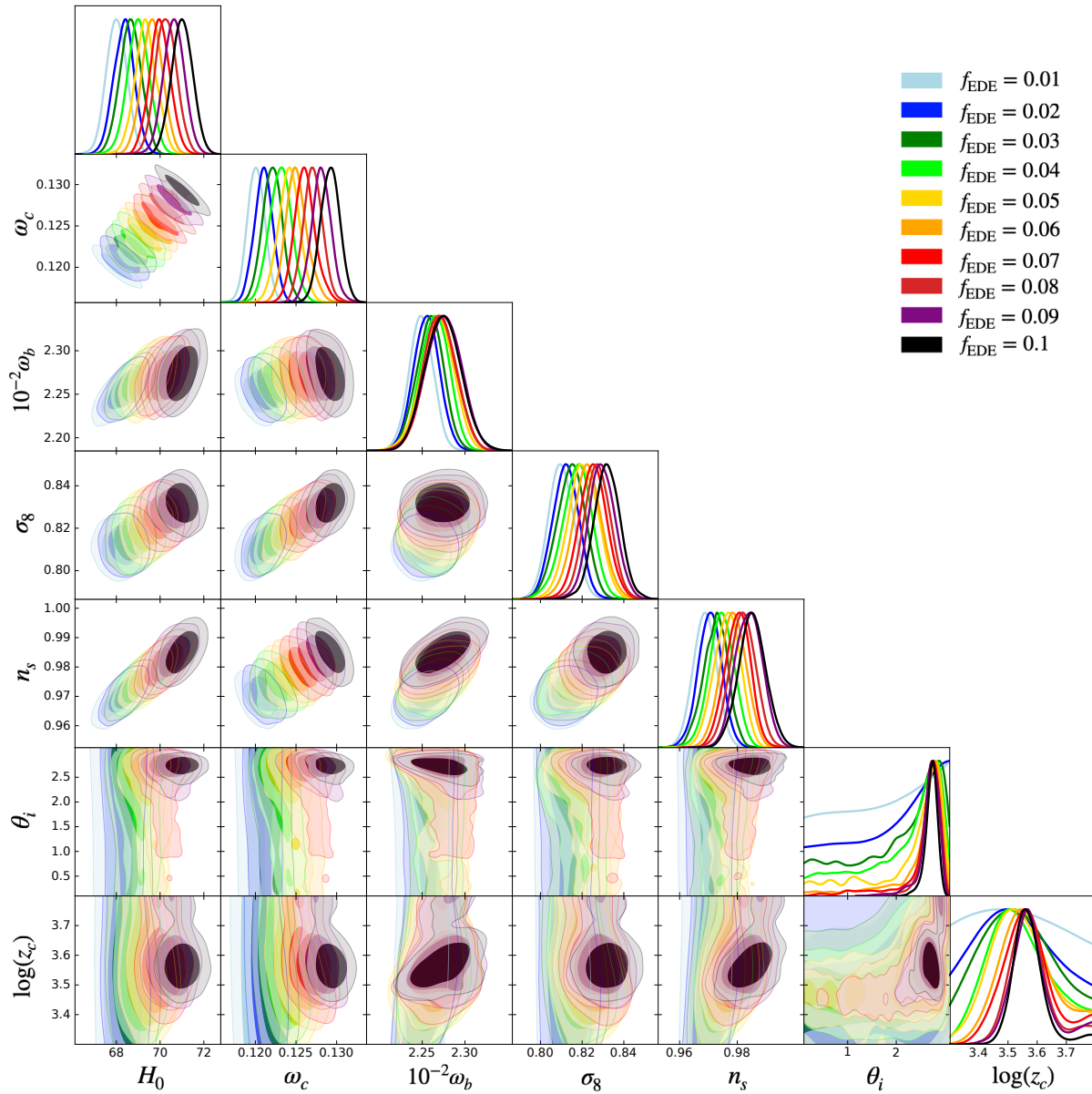


Figure 4.5: MCMC posteriors with f_{EDE} fixed to different values between 0.01 and 0.1.

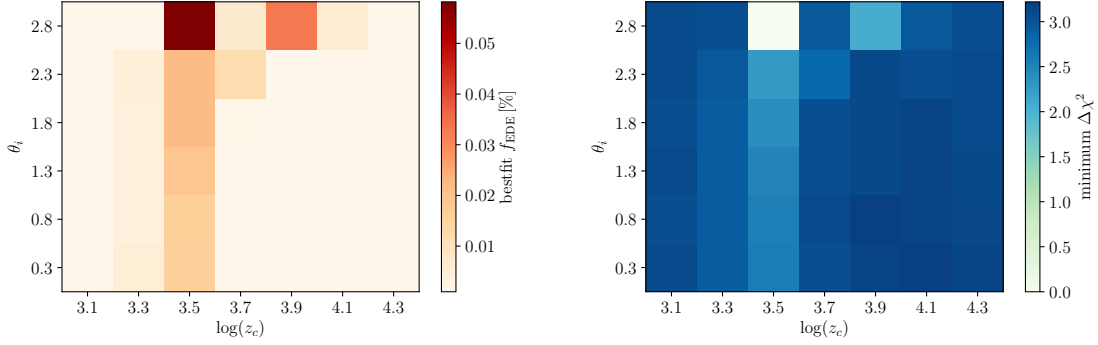


Figure 4.6: Best-fit values of f_{EDE} (left) and $\Delta\chi^2$ (right) for different fixed values of θ_i and $\log(z_c)$. Every value in this 6×7 grid is obtained with the minimization procedure described in Section 4.3.3.

Table 4.1: Best-fit parameters for different cosmologies.

Parameter	best-fit ΛCDM	best-fit $f_{\text{EDE}} = 0.07$	best-fit $f_{\text{EDE}} = 0.11$
$100 \omega_b$	2.245	2.259	2.270
ω_{cdm}	0.1191	0.1260	0.1304
$100 * \theta_s$	1.042	1.042	1.041
$\ln(10^{10} A_s)$	3.044	3.056	3.064
n_s	0.9681	0.9794	0.9872
τ_{reio}	0.0548	0.0549	0.0553
$\log(z_c)$	–	3.55	3.56
θ_i	–	2.76	2.77
z_{reio}	7.701	7.827	7.924
Ω_m	0.3093	0.3046	0.3012
Y_{He}	0.2454	0.2479	0.2480
H_0 [km/s/Mpc]	67.80	70.00	71.45
$10^{+9} A_s$	2.099	2.125	2.141
σ_8	0.808	0.825	0.836
min. χ^2	3237.4	3233.7	3234.6

Acknowledgements

We thank Paolo Campeti, Elisabeth Krause, Evan McDonough, Marta Monelli, Oliver Philcox, Fabian Schmidt, Sherry Suyu, and Sam Witte for useful discussions and suggestions. We also thank the organizers and participants of the Munich Institute for Astro- and Particle Physics (MI-APP) workshop “Accelerating Universe 2.0” for useful discussions about this project during the workshop. This work was supported in part by JSPS KAKENHI Grant No. JP20H05850 and JP20H05859, and the Deutsche Forschungsgemeinschaft (DFG, German Research Foundation) under Germany’s Excellence Strategy - EXC-2094 - 390783311. The Kavli IPMU is supported by World Premier International Research Center Initiative (WPI), MEXT, Japan.

Chapter 5

Resolving the Hubble tension with Early Dark Energy

The contents of this chapter are under review and online available as Herold and Ferreira (2022).

Abstract: Early dark energy (EDE) offers a solution to the so-called Hubble tension. In Ch. 5, it was shown that the constraints on EDE using Markov Chain Monte Carlo are affected by prior volume effects. The goal of this chapter is to present constraints on the fraction of EDE, f_{EDE} , and the Hubble parameter, H_0 , which are not subject to prior volume effects. We conduct a frequentist profile likelihood analysis considering *Planck* cosmic microwave background, BOSS full-shape galaxy clustering, DES weak lensing, and SHOES supernova data. Contrary to previous findings, we find that H_0 for the EDE model is in statistical agreement with the SHOES direct measurement at $< 1.7 \sigma$ for all data sets. For our baseline data set (*Planck* + BOSS), we obtain $f_{\text{EDE}} = 0.087 \pm 0.037$ and $H_0 = 70.57 \pm 1.36$ km/s/Mpc at 68% confidence limit. We conclude that EDE is a viable solution to the Hubble tension.

5.1 Introduction

The increasing precision of cosmological measurements revealed a discrepancy known as the Hubble tension (see Abdalla *et al.*, 2022, for a review). The Hubble tension refers to the difference between direct measurements of H_0 and indirect measurements given a cosmological model. This tension reaches 5σ between the values obtained from the cosmic microwave background (CMB) data from *Planck* for the Λ Cold Dark Matter (Λ CDM) model (Aghanim *et al.*, 2020b), and from the Cepheid-calibrated Type Ia supernovae of the SH0ES project (Riess *et al.*, 2022).

While systematics are considered as a possible cause for the tension, growing interest has been given to the possibility that this tension points to new physics beyond the Λ CDM model. Among the most well studied proposed solutions to address this tension is the early dark energy (EDE) model (Poulin *et al.*, 2019, 2018; Smith *et al.*, 2020), which introduces a new dark-energy component acting in the early Universe.

This model was shown to successfully reduce the tension in H_0 (Knox and Millea, 2020; Schöneberg *et al.*, 2022) when analyzed with *Planck* CMB, Baryon Acoustic Oscillation, Pantheon supernova sample and data from SH0ES (Poulin *et al.*, 2019; Smith *et al.*, 2020). Later it was pointed out in Hill *et al.* (2020); Ivanov *et al.* (2020a); D’Amico *et al.* (2021b) that excluding the SH0ES measurement and including large-scale structure (LSS) probes like galaxy clustering and weak lensing leads to a tight upper limit on the amount of EDE, giving a value of H_0 compatible with the one from Λ CDM and not being able to solve the Hubble tension. Additionally, it was shown that the so-called S_8 -tension, a tension in the amplitude of matter clustering, is worsened for the EDE model (Hill *et al.*, 2020; D’Amico *et al.*, 2021b; Secco *et al.*, 2022).

However, it was shown in Herold *et al.* (2022), previously hinted in Niedermann and Sloth (2020); Smith *et al.* (2020); Murgia *et al.* (2021); Smith *et al.* (2021) and later confirmed in Gómez-Valent (2022), that the previous analyses of the EDE model using standard Bayesian Markov Chain Monte Carlo (MCMC) methods suffer from marginalization or prior volume effects that can bias the posteriors.

Prior volume effects are common effects in MCMC analyses that appear if the posterior is strongly influenced by the prior volume. In the case of the EDE model, the parameter structure of the model leads to large volume differences: When f_{EDE} approaches zero, the model reduces to Λ CDM; in this limit, the other parameters of the EDE model are unconstrained, which leads to an enhanced prior volume for Λ CDM and which can drive the posterior towards low fractions of EDE, f_{EDE} , upon marginalization (Smith *et al.*, 2020).

In view of these effects, it was suggested in Herold *et al.* (2022) to use a frequentist profile likelihood. The profile likelihood and the Bayesian MCMC are complementary statistical tools since they address different statistical questions: While MCMC localizes large volumes in parameter space that fit the data well, the profile likelihood is based only on the minimum χ^2 , i.e. the best fit to the data, regardless of the size of the parameter volume. Therefore, the profile likelihood is reparametrization invariant Hogg *et al.* (2013) and, most importantly, is not influenced

by prior volume effects.

A profile likelihood of the EDE fraction, f_{EDE} , resulted in a $f_{\text{EDE}} = 0.072 \pm 0.036$ (Herold *et al.*, 2022) for *Planck* data (Aghanim *et al.*, 2020b) and Baryon Oscillation Spectroscopic Survey (BOSS) full-shape likelihood (Ivanov *et al.*, 2020b; D’Amico *et al.*, 2021b), which is considerably higher than the MCMC result for the same data set. A similar analysis with free neutrino mass was performed in (Reeves *et al.*, 2023), with the goal of reducing S_8 , finding a similar constraint (see Hamann, 2012; Ade *et al.*, 2014b; Campeti *et al.*, 2022; Campeti and Komatsu, 2022, for application to other cases).

The goal of this chapter is to provide robust constraints in the value of H_0 for the EDE model. We will assess the level of compatibility of the model-dependent H_0 constraints for the EDE model with the SH0ES direct measurement, revealing whether the EDE model can address the Hubble tension.

5.2 Early Dark Energy

The EDE model contains a new component in the energy density of the Universe that behaves like dark energy right after matter-radiation equality, but that dilutes away after recombination. The inclusion of this extra energy component decreases the sound horizon at the last scattering surface, which leads to an increase in H_0 .

EDE (Kamionkowski *et al.*, 2014; Karwal and Kamionkowski, 2016; Caldwell and Devulder, 2018) is the name given to a class of models satisfying the above dynamics (for some examples see Schöneberg *et al.*, 2022). In this work, we use the canonical EDE model (Poulin *et al.*, 2018) which is described by a pseudoscalar field with the potential $V(\phi) = V_0 [1 - \cos(\phi/f)]^n$, where $V_0 = m^2 f^2$, m and f are the explicit and spontaneous symmetry breaking scales, respectively. Based on previous works (Poulin *et al.*, 2018; Smith *et al.*, 2020), we study here the case of $n = 3$, which satisfies the condition that the energy density of EDE dilutes faster than the one for matter.

One can relate the parameters of this model to the phenomenological parameters f_{EDE} and z_c , where f_{EDE} is the maximum fraction of EDE at the critical redshift z_c . This field has a fixed initial value ϕ_i , and becomes dynamical near z_c . These parameters together with the initial dimensionless value of the field $\theta_i \equiv \phi_i/f$, fully describe the EDE model. This phenomenological description is instrumental in making it clear that a higher f_{EDE} indicates a higher H_0 ; it was shown that $f_{\text{EDE}} \sim 0.1$ is necessary to restore concordance in H_0 (Bernal *et al.*, 2016; Knox and Millea, 2020).

5.3 Analysis Methods

5.3.1 Data and modeling

To model the EDE dynamics, we use the public EDE_CLASS_PT code¹ an extension of the Einstein–Boltzmann solver CLASS (Lesgourgues, 2011; Blas *et al.*, 2011), based on CLASS_EDE (Hill *et al.*, 2020) and CLASS-PT (Chudaykin *et al.*, 2020), a code based on the Effective Field Theory (EFT) of LSS (Alam *et al.*, 2017; Baumann *et al.*, 2012; Carrasco *et al.*, 2012) that allows to model the galaxy power spectrum up to mildly nonlinear scales.

We consider the following data sets: *Planck* 2018 TT, TE, EE, low ℓ , lensing (Aghanim *et al.*, 2020b, referred to as *Planck*); the BOSS Data Release 12 (Alam *et al.*, 2017) full-shape power spectrum with a maximum wavenumber, $k_{\max} = 0.25 h/\text{Mpc}$, using a consistent window-function normalization, which we implement along the lines of Beutler and McDonald (2021) and which corrects an inconsistency present before (referred to as BOSS); a Gaussian likelihood centered on the clustering amplitude of matter, $S_8 = \sigma_8 \sqrt{\Omega_m/0.3} = 0.776 \pm 0.017$, measured by the Dark Energy Survey Year 3 analysis (Abbott *et al.*, 2018b, referred to as DES)²; and a Gaussian likelihood centered on $H_0 = 73.04 \pm 1.04$ measured by SH0ES (Riess *et al.*, 2022, referred to as SH0ES).

We sample the ΛCDM parameters $\{\omega_b, \omega_{\text{cdm}}, \theta_s, A_s, n_s, \tau_{\text{reio}}\}$, the EDE parameters $\{f_{\text{EDE}}, \log(z_c), \theta_i\}$, along with the *Planck* and EFT nuisance parameters. Following the convention of the *Planck* collaboration (Aghanim *et al.*, 2020b), we model the neutrino sector by two massless and one massive neutrino species with $m_\nu = 0.06 \text{ eV}$.

5.3.2 Statistical inference: MCMC and profile likelihood

We perform both a Bayesian MCMC and a frequentist profile likelihood analysis using MontePython (Brinckmann and Lesgourgues, 2019) with the Metropolis–Hastings algorithm (Metropolis *et al.*, 1953; Hastings, 1970). We assume the same priors as Philcox and Ivanov (2022) on the EFT nuisance parameters, and the same priors as Hill *et al.* (2020) on the EDE parameters. We require the Gelman-Rubin convergence criterion $R - 1 < 0.05$.

Following the methodology in our previous works (Herold *et al.*, 2022; Reeves *et al.*, 2023), we construct a profile likelihood by fixing the parameter of interest to different values and minimizing $\chi^2 = -2 \ln \mathcal{L}$ with respect to all other parameters of the model, where \mathcal{L} denotes the likelihood. The $\Delta\chi^2$ as a function of the parameter of interest is the profile likelihood. For the minimization, we adopt a simulated annealing approach based on the method used by Schöneberg *et al.* (2022) (see also Hannestad, 2000). As in our previous work (Herold *et al.*, 2022), we con-

¹https://github.com/Michalychforever/EDE_class_pt

²Using a Gaussian likelihood is an approximation but it was tested in Hill *et al.* (2020) for DES Y1 that the difference to the full likelihood is small for the EDE model.

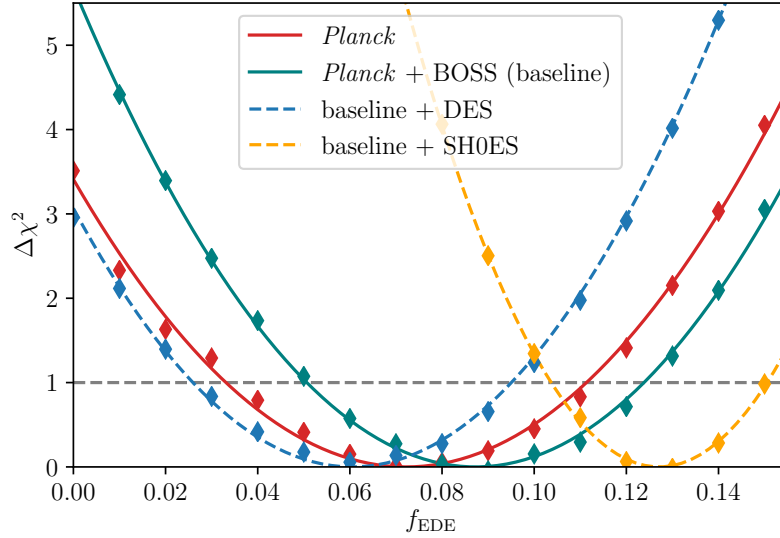


Figure 5.1: Profile likelihoods (markers) for the maximum fraction of EDE, f_{EDE} , for different data sets. The intersection of the parabola fit (lines) with $\Delta\chi^2 = 1$ (horizontal dashed line) gives the 1σ confidence interval in the approximate Neyman construction.

Data set	$\chi^2(\Lambda\text{CDM})$	$\chi^2(\text{EDE})$	$\Delta\chi^2$	ΔAIC
<i>Planck</i>	2774.24	2770.72	-3.52	+2.48
<i>Planck+BOSS (base)</i>	3045.65	3039.98	-5.67	+0.33
Baseline + DES	3052.06	3049.13	-2.93	+3.07
Baseline + SH0ES	3068.44	3042.08	-26.36	-20.36

Table 5.1: The χ^2 values of the ΛCDM and best-fit EDE models, the difference $\Delta\chi^2 = \chi^2(\text{EDE}) - \chi^2(\Lambda\text{CDM})$, the Akaike information criterion (AIC, Akaike, 1974).

struct a confidence interval from the profile likelihood following the prescription by Feldman and Cousins (1998), which extends the procedure by Neyman (1937) and is also valid at a physical boundary. We quote confidence intervals obtained from profile likelihoods (MCMC) as best fit (mean) $\pm 1\sigma$.

5.4 Results and discussion

Fig. 5.1 and Fig. 5.2 present the final result of our profile likelihood analysis for f_{EDE} and H_0 for different datasets, with final confidence intervals summarized in Fig. 5.3 and Table 5.1.

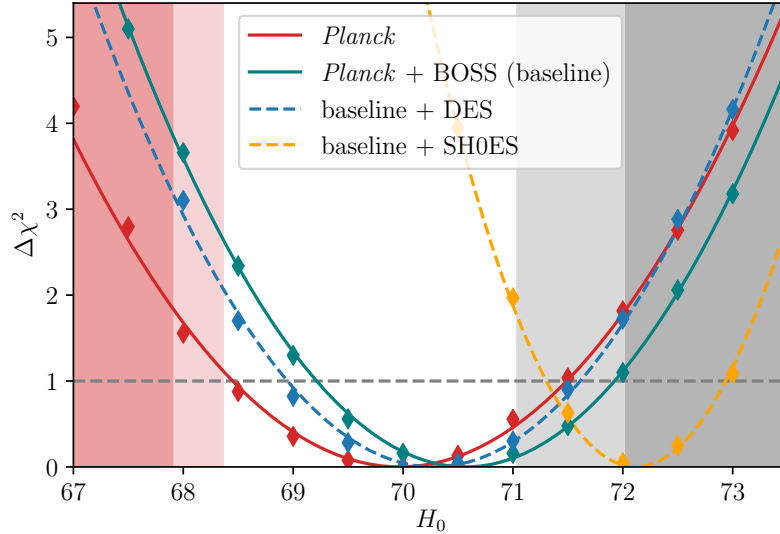


Figure 5.2: Profile likelihoods for the Hubble parameter, H_0 , for different data sets. The red vertical region corresponds to the 1σ and 2σ contours for H_0 from *Planck* 2018 for Λ CDM, while the grey region corresponds to the 1σ and 2σ contours for the direct measurement by SH0ES.

Data set	f_{EDE}	H_0 (consistency w. SH0ES)
<i>Planck</i>	0.072 ± 0.039	69.97 ± 1.52 (1.7σ)
<i>Planck</i> +BOSS (base)	0.087 ± 0.037	70.57 ± 1.36 (1.4σ)
Baseline + DES	$0.061^{+0.035}_{-0.034}$	70.28 ± 1.33 (1.6σ)
Baseline + SH0ES	0.127 ± 0.023	72.12 ± 0.82 (0.69σ)

Table 5.2: Constraints on f_{EDE} and H_0 , and the compatibility with the SH0ES measurement in units of σ for the different data sets considered in this work.

5.4.1 *Planck* + BOSS full-shape analysis (baseline)

Our baseline data set consists of *Planck* CMB and BOSS galaxy clustering data (solid teal lines in Figs. 5.1, 5.2). The confidence intervals obtained from the profile likelihood are:

$$f_{\text{EDE}} = 0.087 \pm 0.037, \quad H_0 = 70.57 \pm 1.36 \text{ km/s/Mpc}. \quad (5.1)$$

To assess parameter consistency, we report the one-dimensional difference between the best fits of the two measurements divided by the quadrature sum of the 1σ errors. We find that H_0 obtained from the baseline data set within the EDE model is consistent with SH0ES at 1.4σ .

Compared to Λ CDM, the goodness of fit to the data improves by $\Delta\chi^2 = -5.67$ for the EDE model with $f_{\text{EDE}} = 0.09$ (see Table 5.1)³. To assess whether the data prefers EDE with extra

³We cite χ^2 and best-fit parameters for the EDE cosmology with fixed f_{EDE} that is closest to the global minimum

parameters over Λ CDM, we compute the Akaike information criterion (AIC, Burnham and Anderson, 2002), which penalizes additional parameters and is defined as $\Delta\text{AIC} = \Delta\chi^2 + 2\Delta N$, where ΔN is the number of additional parameters of the extended model (for EDE: $\Delta N = 3$). We find $\Delta\text{AIC} = +0.33$, i.e. a not statistically significant preference for Λ CDM over EDE.

For direct comparison, we run an MCMC analysis for the same data set and find a tight upper limit $f_{\text{EDE}} < 0.072$ (at 95% confidence), and $H_0 = 68.55_{-1.06}^{+0.62}$ km/s/Mpc, which is in tension with SH0ES at 3.7σ . As pointed out previously Herold *et al.* (2022), the difference to the profile likelihood result can be explained by prior volume effects affecting the results of the MCMC results.

The constraints on f_{EDE} and H_0 found here are slightly higher than those from a profile likelihood analysis with the previously widely used BOSS likelihood using an inconsistent normalization ($f_{\text{EDE}} = 0.072 \pm 0.036$, Herold *et al.*, 2022). The consistent window-function normalization leads to higher values of S_8 . Since S_8 is increased in EDE cosmologies compared to Λ CDM, a higher S_8 allows for more EDE. This is in agreement with Simon *et al.* (2023), who use MCMC to constrain EDE and find a weaker upper limit on f_{EDE} with the consistent window-function normalization as compared to the inconsistent normalization.

With the profile likelihood analysis, we also find shifts in other cosmological parameters compared to Λ CDM: the best-fit n_s increases from 0.968 (Λ CDM) to 0.983 (best-fit EDE cosmology, $f_{\text{EDE}} = 0.09$), and ω_{cdm} from 0.120 (Λ CDM) to 0.129 ($f_{\text{EDE}} = 0.09$), which can be understood as a compensation of an enhanced early Sachs-Wolfe effect in EDE cosmologies (Ivanov *et al.*, 2020a; Vagnozzi, 2021). The most notable change is in S_8 , which increases from 0.828 (Λ CDM) to 0.840 ($f_{\text{EDE}} = 0.09$), worsening the so-called S_8 -tension with weak-lensing experiments (Di Valentino and Bridle, 2018; Nunes and Vagnozzi, 2021).

5.4.2 Baseline + DES

Since EDE cosmologies feature higher S_8 (Smith *et al.*, 2020; Hill *et al.*, 2020; Secco *et al.*, 2022), including weak lensing measurements into the analysis is an important test for EDE. In this section, we include a Gaussian likelihood from DES⁴ with $S_8 = 0.776 \pm 0.017$ along with the baseline data set (blue dashed lines in Figs. 5.1, 5.2). The profile likelihood analysis yields:

$$f_{\text{EDE}} = 0.061_{-0.034}^{+0.035}, \quad H_0 = 70.28 \pm 1.33 \text{ km/s/Mpc}. \quad (5.2)$$

As expected, we find smaller f_{EDE} and H_0 than those from the baseline data set, but H_0 is still consistent with SH0ES at 1.6σ . The improvement of the fit compared to Λ CDM, $\Delta\chi^2 = -2.93$, is smaller than for the baseline result. The worsening can be attributed mainly to the contribution

(minimum of the profile likelihood). The error of this approximation is negligible compared to the 1σ statistical uncertainty and can only lead to an *underestimation* of the improvement of fit for EDE.

⁴We did not include likelihoods for HSC (Hikage *et al.*, 2019) and KiDS (Asgari *et al.*, 2021) simultaneously since there is non-negligible cross-correlation between the data sets. Using a combined weak-lensing likelihood would be an important further check.

from the S_8 likelihood. The best-fit S_8 for Λ CDM, $S_8 = 0.812$, and the best-fit EDE model $f_{\text{EDE}} = 0.06$, $S_8 = 0.817$, are comparable but both are higher than the DES measurement, $S_8 = 0.776$. The AIC shows a mild preference for Λ CDM over EDE, $\Delta\text{AIC} = +3.07$.

The trend of a decreasing f_{EDE} and H_0 when including an S_8 likelihood is similar as in previous MCMC analyses (Smith *et al.*, 2020; Hill *et al.*, 2020; Secco *et al.*, 2022) but the effect in the profile likelihood is less pronounced since it is not overlaid by prior volume effects. While the MCMC results suggest that EDE is not able to solve the H_0 tension, the profile-likelihood result for H_0 from the baseline + DES data set is in statistical agreement with the SH0ES measurement.

5.4.3 Baseline + SH0ES

Given that the value of H_0 for the EDE baseline data set is consistent with the SH0ES measurement at 1.4σ , it is sensible to combine both data sets. A profile-likelihood analysis of the baseline data set with a Gaussian likelihood centered on the measurement by the SH0ES experiment, $H_0 = 73.04 \pm 1.04$ (yellow dashed lines in Figs. 5.1, 5.2) yields:

$$f_{\text{EDE}} = 0.127 \pm 0.023, \quad H_0 = 72.12 \pm 0.82 \text{ km/s/Mpc.} \quad (5.3)$$

This constraint of H_0 is consistent with SH0ES at 0.69σ . We find an improvement of fit of the EDE model compared to Λ CDM by $\Delta\chi^2 = -26.36$, where the main contribution to the $\Delta\chi^2$ comes from the SH0ES- H_0 likelihood, $\Delta\chi_{\text{SH0ES}}^2 = -18.47$. The AIC shows a strong preference for the EDE model over Λ CDM, $\Delta\text{AIC} = -20.36$. The profile likelihood constraints are consistent with previous MCMC constraints including SH0ES data (Smith *et al.*, 2020; Hill *et al.*, 2020; D’Amico *et al.*, 2021b; Murgia *et al.*, 2021)⁵ at $< 1\sigma$.

The constraints of H_0 and f_{EDE} within the EDE model for the baseline + SH0ES data set are consistent with the constraints for all other data sets considered here at $< 1.3\sigma$ and $< 1.6\sigma$, respectively.

5.4.4 Planck-only constraint and comparison to ACT

Lastly, we probe the constraining power of the *Planck* CMB data alone. We find

$$f_{\text{EDE}} = 0.072 \pm 0.039, \quad H_0 = 69.97 \pm 1.52 \text{ km/s/Mpc.} \quad (5.4)$$

The H_0 constraint is consistent with SH0ES at 1.7σ . We find an improvement of fit of $\Delta\chi^2 = -3.52$. This improvement is dominated by the *Planck* high- ℓ likelihood with $\Delta\chi_{\text{high-}\ell}^2 = -2.90$. The AIC shows a mild preference of Λ CDM over EDE, $\Delta\text{AIC} = +2.48$.

⁵With the exception of the result from D’Amico *et al.* (2021b) for Planck+BAO+SnIa(Pantheon)+BOSS full-shape power spectrum+SH0ES, which is consistent with our result at $\sim 2\sigma$.

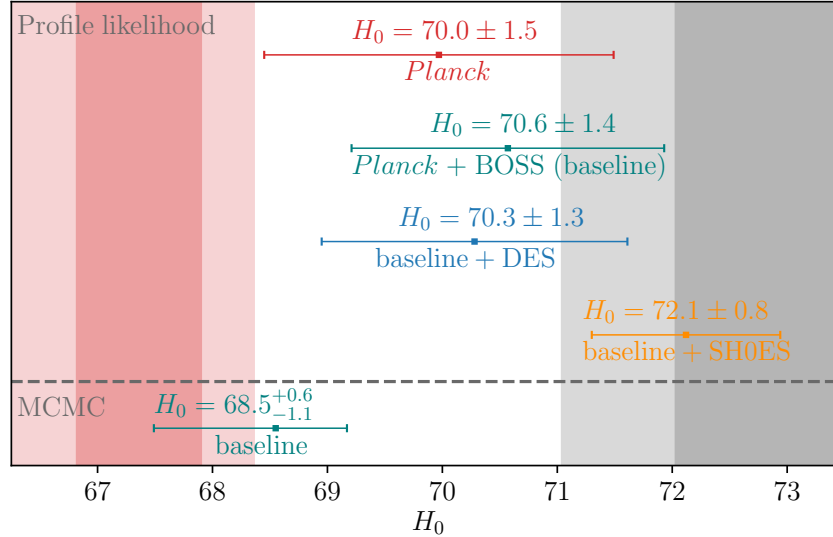


Figure 5.3: Constraints of H_0 within the EDE model for different data sets. The top four errorbars show constraints from the profile likelihood, whereas the bottom errorbar shows the constraint from MCMC. For comparison, the red shaded area corresponds to the 1σ and 2σ constraint from *Planck* (Aghanim *et al.*, 2020b) assuming Λ CDM and the grey shaded area to the 1σ and 2σ constraint from SH0ES (Riess *et al.*, 2022).

The relatively high f_{EDE} preferred by *Planck* in the profile likelihood analysis is interesting in light of the preference for f_{EDE} in an MCMC analysis of Atacama Cosmology Telescope (ACT) CMB data (Choi *et al.*, 2020). The profile likelihood constraints of f_{EDE} from *Planck* are consistent at $< 1\sigma$ with MCMC constraints from ACT ($f_{\text{EDE}} = 0.091^{+0.020}_{-0.036}$ for the baseline data set in Hill *et al.* (2022), see also Smith *et al.* (2022); La Posta *et al.* (2022)). The difference between the results from *Planck* and ACT from MCMC analyses is likely due to prior volume effects in the MCMC analysis for *Planck*. The strong preference for the EDE model over Λ CDM that was found for ACT (Hill *et al.*, 2022) seems to indicate that the constraints from this data set are less affected by prior volume effects.

5.5 Conclusion

In this chapter, we obtained constraints on the value of H_0 for the EDE model, which are not subject to prior volume effects, using a frequentist profile likelihood and assessed the viability of EDE as a solution to the Hubble tension.

It was previously concluded from MCMC analyses that EDE is not able to resolve the H_0 tension and simultaneously fit different cosmological data. We find a similar result from the MCMC analysis of our baseline data set (bottom errorbar in Fig. 5.3). As was previously shown

in Herold *et al.* (2022), MCMC analyses of the EDE model are affected by marginalization or prior volume effects. Therefore, we used the profile likelihood to obtain confidence intervals for H_0 (Fig 5.3) and to assess consistency with other measurements and the resolution of the tension.

We assessed whether the data prefers EDE over Λ CDM using the AIC, which takes into account that the EDE model has three additional parameters compared to Λ CDM. The AIC shows a mild preference for Λ CDM for the baseline data set, the baseline + DES and the Planck-only data sets. Only when adding SH0ES, there is a clear preference for the EDE model over Λ CDM. Therefore, EDE presents a good fit to CMB and LSS even when penalizing the additional parameters of EDE.

Our baseline data set yields $H_0 = 70.57 \pm 1.36$ km/s/Mpc, which is consistent with SH0ES at 1.4σ . This value is considerably higher than the MCMC result, reinforcing the evidence for prior volume effects in the Bayesian analysis. Adding a likelihood centered on the S_8 measurement from DES decreases f_{EDE} with respect to the baseline data set, translating into a mild decrease in H_0 . This is expected since EDE cosmologies show a positive correlation of S_8 with f_{EDE} and H_0 (Secco *et al.*, 2022). However, this decrease is much smaller than the one found in previous MCMC analysis. The H_0 for baseline + DES is consistent with the SH0ES value at 1.6σ . Hence, even for the most constraining data combination for EDE considered here, we find an agreement with SH0ES. Given that the value of H_0 for the baseline data set is consistent with the SH0ES measurement, we can combine both data sets. As expected from previous analyses, including SH0ES to the baseline data set results in an even higher H_0 than for the baseline data set. This is consistent with the SH0ES measurement at 0.69σ . Finally, we find that the H_0 constraint from *Planck* data alone is compatible with SH0ES, and interestingly also in agreement with previous works performing an MCMC analysis with ACT data. Considering the relative χ^2 contributions for all likelihoods considered in this work, we find that (apart from SH0ES), the *Planck* high- ℓ likelihood dominates the improvement of fit compared to all other data sets. We present an exploration of parameter correlations and an extended table of our results in the supplementary material Sec. 5.6.

For all data combinations, the H_0 value obtained with the profile likelihood analysis is consistent with the measurement from SH0ES at $\leq 1.7\sigma$. Therefore, the values of H_0 for the EDE model are in agreement with SH0ES. We conclude that the EDE model provides a resolution of the Hubble tension.

5.6 Supplementary material

5.6.1 Parameter correlations

One can use the data obtained from the profile likelihood to explore correlations between the parameter of interest, here f_{EDE} , and the other cosmological parameters. In Fig. 5.4, we show the best-fit $\log(z_c)$ (left) and θ_i (right) as a function of the fixed value of f_{EDE} for different data

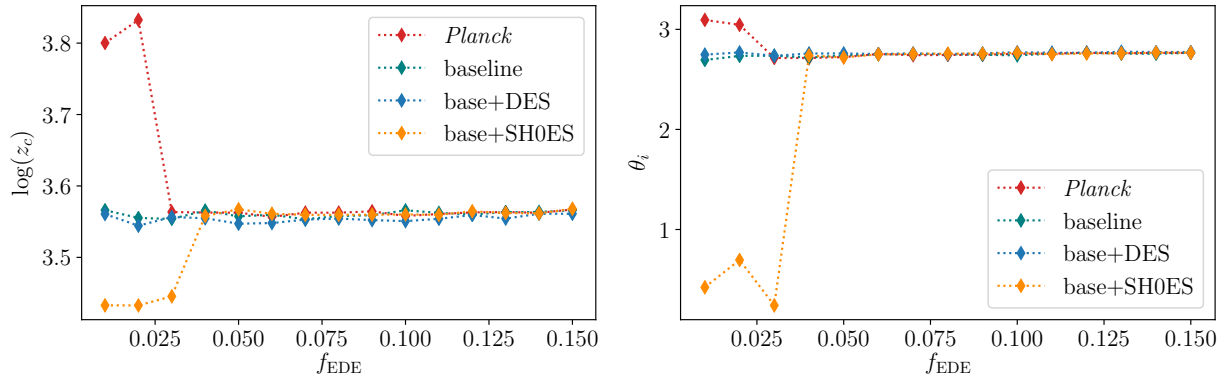


Figure 5.4: Best-fit values of $\log(z_c)$ (left) and θ_i (right) as a function of the fixed value of f_{EDE} for different data sets as indicated in the legend.

sets. We find that the best-fit values for both parameters are constant within a few percent apart for small values of f_{EDE} , where both parameters are not well constrained.

5.6.2 Best-fit parameters and χ^2 contributions

In Tab. 5.6.2, we show the best-fit parameters for *Planck*+ BOSS full-shape data (baseline, BL), BL + a Gaussian likelihood centered on $S_8 = \sigma_8 \sqrt{\Omega_m}/0.3 = 0.776 \pm 0.017$ (DES, Abbott *et al.*, 2018a), BL + a Gaussian likelihood centered on $H_0 = 73.04 \pm 1.04$ (SH0ES, Riess *et al.*, 2022) and *Planck*-only data. In the bottom part of the table we show the contributions in $\chi^2 = -2 \log(\mathcal{L})$ from the different data sets. Since for the profile likelihood, we ran minimizations with f_{EDE} fixed to values between 0 and 0.15 (and all other parameters free), we show the cosmology that is closest to the global best fit (c.f. 5.2).

We additionally ran four minimizations, with all parameters free (including f_{EDE}) to obtain the global best-fit cosmology for the baseline and baseline + SH0ES data sets. The best-fitting parameters are shown in Tab. 5.6.2.

Acknowledgements

We thank Eiichiro Komatsu for valuable discussions and comments on the draft. We also thank Steen Hannestad, Colin Hill, Emil Holm, Yosuke Kobayashi, Alex Reeves, Théo Simon, Thomas Tram, Sam Witte, and Pierre Zhang for useful discussions and suggestions. LH would like to thank Kavli IPMU for the hospitality where part of this work was conducted. The Kavli IPMU is supported by World Premier International Research Center Initiative (WPI), MEXT, Japan.

Data	baseline (BL)		BL+DES		BL+SH0ES		Planck	
Model	Λ CDM	EDE _{0.09}	Λ CDM	EDE _{0.06}	Λ CDM	EDE _{0.13}	Λ CDM	EDE _{0.07}
Best-fit parameters								
100 ω_b	2.243	2.266	2.251	2.267	2.261	2.276	2.239	2.259
ω_{cdm}	0.1196	0.1285	0.1184	0.1239	0.1177	0.1328	0.12	0.1268
100 * θ_s	1.042	1.041	1.042	1.042	1.042	1.041	1.042	1.041
$\ln 10^{10} A_s$	3.047	3.063	3.041	3.05	3.056	3.068	3.045	3.058
n_s	0.9679	0.9833	0.9707	0.9802	0.9731	0.9916	0.9665	0.9789
τ_{reio}	0.0556	0.0563	0.0537	0.0542	0.0616	0.0555	0.0543	0.0549
$\log_{10} z_c$	—	3.559	—	3.548	—	3.562	—	3.563
$\theta_{\text{i,scf}}$	—	2.747	—	2.754	—	2.761	—	2.742
z_{reio}	7.803	7.994	7.579	7.695	8.324	7.974	7.685	7.834
Ω_m	0.3122	0.3046	0.305	0.299	0.3006	0.2997	0.315	0.3088
Y_{He}	0.2479	0.248	0.2479	0.248	0.2479	0.248	0.2478	0.2479
H_0	67.6	70.59	68.13	70.16	68.49	72.2	67.39	69.7
$10^{+9} A_s$	2.106	2.139	2.092	2.113	2.124	2.15	2.101	2.128
σ_8	0.8115	0.8332	0.8054	0.8183	0.8097	0.8424	0.8119	0.8284
S_8	0.828	0.840	0.812	0.817	0.811	0.842	0.832	0.840
χ^2 contributions								
BOSS NGC z_3	61.55	60.18	61.53	60.66	61.64	59.66	—	—
BOSS SGC z_3	64.31	64.25	64.74	64.78	65.04	64.28	—	—
BOSS NGC z_1	69.88	70.01	69.77	70.06	69.78	70.35	—	—
BOSS SGC z_1	75.91	75.11	75.58	75.04	75.44	74.72	—	—
<i>Planck</i> high- ℓ	2345.94	2342.85	2348.50	2345.74	2348.67	2345.14	2346.18	2343.28
<i>Pl.</i> low- ℓ EE	396.28	396.35	395.87	395.91	397.70	396.16	396.03	396.11
<i>Pl.</i> low- ℓ TT	22.92	21.52	22.35	21.56	22.20	20.97	23.14	21.90
<i>Planck</i> lensing	8.85	9.71	9.22	9.58	8.86	10.14	8.89	9.43
S_8 (DES)	—	—	4.51	5.80	—	—	—	—
H_0 (SH0ES)	—	—	—	—	19.12	0.65	—	—
Total χ^2	3045.65	3039.98	3052.06	3049.13	3068.44	3042.08	2774.24	2770.72

Table 5.3: Best-fit parameters (top half) and χ^2 contributions (bottom half of the table) for the Λ CDM and EDE models. For each of the four data sets considered in this work, we show the EDE model with fixed f_{EDE} closest to the global best fit indicated by the index EDE _{f_{EDE}} .

Param	BL	BL+SHOES
$100 \omega_b$	2.265	2.278
ω_{cdm}	0.1282	0.1324
$100 * \theta_s$	1.041	1.041
$\ln 10^{10} A_s$	3.063	3.071
n_s	0.9831	0.9917
τ_{reio}	0.05626	0.05682
f_{EDE}	0.08717	0.1271
$\log_{10} z_c$	3.56	3.563
$\theta_{\text{i,scf}}$	2.749	2.768
z_{reio}	7.992	8.101
Ω_{m}	0.3052	0.2993
Y_{He}	0.248	0.248
H_0	70.46	72.15
$10^{+9} A_s$	2.139	2.155
σ_8	0.8328	0.8427
S_8	0.840	0.850

Table 5.4: Global best-fit parameters (with f_{EDE} free) for the baseline data (BL) and the baseline + SHOES (BL+SHOES) data set

Chapter 6

Cosmological Concordance with Early Dark Energy and Massive Neutrinos?

*Parts of this chapter have been published as
Reeves, Herold, Vagnozzi, Sherwin, and Ferreira (2023).*

Abstract: The early dark energy (EDE) solution to the Hubble tension comes at the cost of an increased clustering amplitude, argued to worsen the fit to galaxy clustering data. We explore whether freeing the total neutrino mass, M_ν , which can suppress small-scale power, can improve EDE's fit to galaxy clustering. Using *Planck* Cosmic Microwave Background and BOSS galaxy clustering data, a Bayesian analysis shows that freeing M_ν does not increase the inferred EDE fraction f_{EDE} , and there is no evidence for non-zero M_ν . A frequentist analysis reveals a correlation between M_ν and the EDE fraction, f_{EDE} , which keeps H_0 fixed as M_ν increases, and supports earlier evidence of prior volume effects impacting the Bayesian constraints. We find that the baseline EDE model with $M_\nu = 0.06 \text{ eV}$ provides the overall best fit. Compared to this, a model with $M_\nu = 0.24 \text{ eV}$ maintains the same $H_0[\text{km/s/Mpc}]=(70.08, 70.11, \text{ respectively})$ whilst decreasing $S_8=(0.837, 0.826)$ to below the ΛCDM value, but worsening the fit significantly, hence providing no clear evidence that an increased M_ν can alleviate the clustering issue in EDE. We find that these results are driven not by the clustering amplitude, but by background shifts in the BAO scale.

6.1 Introduction

The Hubble tension is a disagreement between independent measurements of the Hubble constant H_0 (Di Valentino *et al.*, 2021; Perivolaropoulos and Skara, 2022; Abdalla *et al.*, 2022). One proposed solution to this tension is early dark energy (EDE), a model which introduces a pre-recombination dark energy (DE)-like component that boosts the expansion rate in order to reduce the sound horizon and decays quickly after (Karwal and Kamionkowski, 2016; Poulin *et al.*, 2018). Although EDE was shown to alleviate the H_0 tension and present a good fit to cosmic microwave background (CMB), weak lensing (WL) and large-scale structure (LSS) data (Poulin *et al.*, 2019; Smith *et al.*, 2020, 2021; Murgia *et al.*, 2021; Herold *et al.*, 2022), parameter shifts in high- f_{EDE} cosmologies lead to an increase in the clustering amplitude, σ_8 , and the related parameter S_8 , worsening the “ S_8 discrepancy” (Di Valentino and Bridle, 2018; Hill *et al.*, 2020; Ivanov *et al.*, 2020a; D’Amico *et al.*, 2021b; Nunes and Vagnozzi, 2021).

In this work, we study the influence of massive neutrinos on EDE, motivated by their free-streaming nature, whose associated power suppression might counteract the EDE-induced enhancement and provide a better fit to LSS data. We find no clear benefits for EDE resulting from massive neutrinos, neither in a Bayesian nor frequentist setting. We investigate prior volume effects, and physical effects driving our parameter constraints, which overall motivate further studies of EDE cosmologies with massive neutrinos.

6.2 EDE and massive neutrinos

The simplest EDE model consists of an ultra-light scalar field initially displaced from the minimum of its potential and frozen by Hubble friction, behaving as a DE component and boosting the pre-recombination expansion rate. Once the Hubble rate drops below its effective mass, the field becomes dynamical, rolls down and oscillates around the minimum of its potential. The ‘canonical’ EDE model is assumed to consist of a pseudoscalar (axion-like) field with the following potential:

$$V(\phi) = m^2 f^2 \left[1 - \cos\left(\frac{\phi}{f}\right) \right]^n, \quad (6.1)$$

where m and f are the EDE ‘mass’ and decay constant, respectively. With this choice of potential, EDE later decays as a fluid with effective equation of state $\langle w_\phi \rangle = (n - 1)/(n + 1)$.

The fundamental particle-physics parameters m and f can be traded for the phenomenological parameters f_{EDE} and z_c : at redshift z_c , EDE’s fractional contribution to the energy density is maximal and equal to $f_{\text{EDE}} = \rho_{\text{EDE}}/3M_{\text{Pl}}^2 H(z_c)^2$, where ρ_{EDE} is EDE’s energy density, M_{Pl} is the *Planck* mass, and $H(z)$ is the Hubble rate. The physics of the EDE model is then governed by four parameters: f_{EDE} , z_c , n , and the initial misalignment angle, $\theta_i = \phi_i/f$, with ϕ_i the initial field value. For simplicity we set $n = 3$, corresponding to the best-fit value reported by Poulin

et al. (2019). Increasing f_{EDE} reduces r_{drag} , the sound horizon at the drag epoch, and solving the Hubble tension requires $f_{\text{EDE}} \gtrsim 0.1$.

To compensate for the EDE-induced enhancement of the early integrated Sachs-Wolfe (eISW) effect and preserve the fit to the CMB (Vagnozzi, 2021), EDE's success comes at the cost of an increase in the dark matter (DM) density $\omega_c = \Omega_c h^2$. This boosts the matter power spectrum and raises $S_8 = \sigma_8(\Omega_m/0.3)^{0.5}$, worsening the S_8 discrepancy present within Λ CDM. EDE was thus argued to be disfavored by WL and galaxy clustering data (Hill *et al.*, 2020), although Murgia *et al.* (2021), Smith *et al.* (2021), Herold *et al.* (2022), and Gómez-Valent (2022) argued that this is in part due to prior volume effects.

A possible remedy is to add extra components absorbing the excess power (e.g. Allali *et al.*, 2021; Ye *et al.*, 2023; Clark *et al.*, 2021). Massive neutrinos are a natural candidate in this sense as oscillation experiments show that at least two neutrino mass eigenstates are massive. In this chapter, we include the neutrino mass sum, M_ν , as a free parameter rather than fixing it to the minimum allowed value of 0.06 eV as in the baseline EDE model. Due to their free-streaming nature, massive neutrinos suppress small-scale power (Lesgourgues and Pastor, 2006). Note that models connecting EDE to neutrinos and predicting high M_ν have been studied (Sakstein and Trodden, 2020; Carrillo González *et al.*, 2021), alongside the role of neutrino physics in relation to cosmic tensions (Ilić *et al.*, 2019; Das *et al.*, 2022; Di Valentino and Melchiorri, 2022; Sakr *et al.*, 2022; Chudaykin *et al.*, 2022).

Adding M_ν as a free parameter within Λ CDM induces well-known parameter degeneracies at the CMB level: a negative M_ν - H_0 correlation related to the geometrical degeneracy, and a positive M_ν - ω_c correlation connected to the CMB lensing amplitude (Vagnozzi *et al.*, 2018; Roy Choudhury and Hannestad, 2020). BAO data partially help in breaking these degeneracies (especially the M_ν - H_0 degeneracy). At fixed acoustic scale θ_s , increasing M_ν reduces the BAO angular scale $\theta_{\text{BAO}} = r_{\text{drag}}/D_V(z_{\text{eff}})$ (Hou *et al.*, 2014; Archidiacono *et al.*, 2017; Boyle and Komatsu, 2018), with $D_V(z_{\text{eff}})$ the volume-averaged distance at the effective redshift z_{eff} .

6.3 Datasets and methodology

We use *Planck* 2018 CMB temperature, polarization, and lensing measurements, combining the Plik TTTEEE, lowl, lowE, and lensing likelihoods (Aghanim *et al.*, 2020a). We add the joint pre-reconstruction full-shape plus post-reconstruction BAO likelihood for the BOSS DR12 galaxies (see Ivanov *et al.*, 2020b; Philcox *et al.*, 2020).¹ The cross-covariance between full-shape and BAO is fully taken into account in the likelihood. The full-shape measurements include both the monopole and quadrupole moments. We do not include a distance ladder H_0 prior to not bias H_0 towards high values (see also Efstathiou, 2021).

¹Note that in this chapter, we do not use the updated window-function treatment (Beutler and McDonald, 2021) as in Ch. 5. We do not expect a big impact on our constraints, which are driven by the BAO scale.

We consider a 3-parameter EDE+ M_ν (10 parameters in total) model where, besides the 6 Λ CDM parameters, M_ν and 3 EDE parameters (f_{EDE} , $\log_{10} z_c$, and θ_i , fixing $n = 3$) are varied. The neutrino mass spectrum is modelled following the degenerate approximation, sufficiently accurate for the precision of current data (Vagnozzi *et al.*, 2017; Giusarma *et al.*, 2018; Roy Choudhury and Hannestad, 2020; Archidiacono *et al.*, 2020; Tanseri *et al.*, 2022). For comparison, we also consider 3 related models: 3-parameter EDE with fixed $M_\nu = 0.06$ eV (9 parameters in total), Λ CDM+ M_ν ($f_{\text{EDE}} = 0$, 7 parameters in total), and the standard 6-parameter Λ CDM model.

Theoretical predictions are computed using the EDE-CLASS-PT Boltzmann solver², itself a merger of CLASS_EDE (Hill *et al.*, 2020) and CLASS-PT (Philcox *et al.*, 2020), themselves both extensions to the Boltzmann solver CLASS (Blas *et al.*, 2011). The underlying galaxy power spectrum model is based on the Effective Field Theory (EFT, Baumann *et al.*, 2012) of LSS, which is the most general, symmetry-driven model for the mildly non-linear clustering of biased tracers of the LSS, accounting for the complex and poorly-known details of short-scale physics which are integrated out.

We follow two analysis methods. We begin with a standard Bayesian analysis, adopting Markov Chain Monte Carlo (MCMC) methods and using the MontePython MCMC sampler (Audren *et al.*, 2013; Brinckmann and Lesgourgues, 2019). We impose the same (flat) priors on the EDE parameters as in Hill *et al.* (2020), whereas for the EFT of LSS nuisance parameters we follow Philcox *et al.* (2020). Following the conclusions of Herold *et al.* (2022); Herold and Ferreira (2022), and the analysis in Ade *et al.* (2014b) for varying neutrino mass sum, we then perform a profile-likelihood analysis in M_ν : for a given (fixed) value of M_ν , after minimizing the χ^2 with respect to all other parameters, the profile likelihood is given by $\Delta\chi^2(M_\nu)$. We follow the minimization method of Schöneberg *et al.* (2022), referred to as S21, running a series of MCMCs with decreased temperature and enhanced sensitivity to likelihood differences. We checked that this method out-performs the gradient descent-based Migrad algorithm (James and Roos, 1975).

6.4 Markov Chain Monte Carlo analysis

In Fig. 6.1, we show the EDE posterior obtained from a Bayesian MCMC analysis of *Planck* CMB and BOSS full-shape clustering data³ while varying M_ν (red, green) and fixing it to $M_\nu = 0.06$ eV (yellow, blue). The contours for all parameters do not change significantly when varying or fixing M_ν . Only in the case with *Planck*-only data, the H_0 and σ_8 constraints widen slightly for the case with M_ν as a free parameter (although not in the H_0 -tension-resolving direction). We show the posteriors for different data-set combinations in the supplementary material 6.7.1.

Since prior-volume effects could influence the results of the full 3-parameter EDE model, we

²https://github.com/Michalychforever/EDE_class_pt

³Note that we do not include the reconstructed BAO information here. For posteriors including the BAO scale, see Reeves *et al.* (2023).

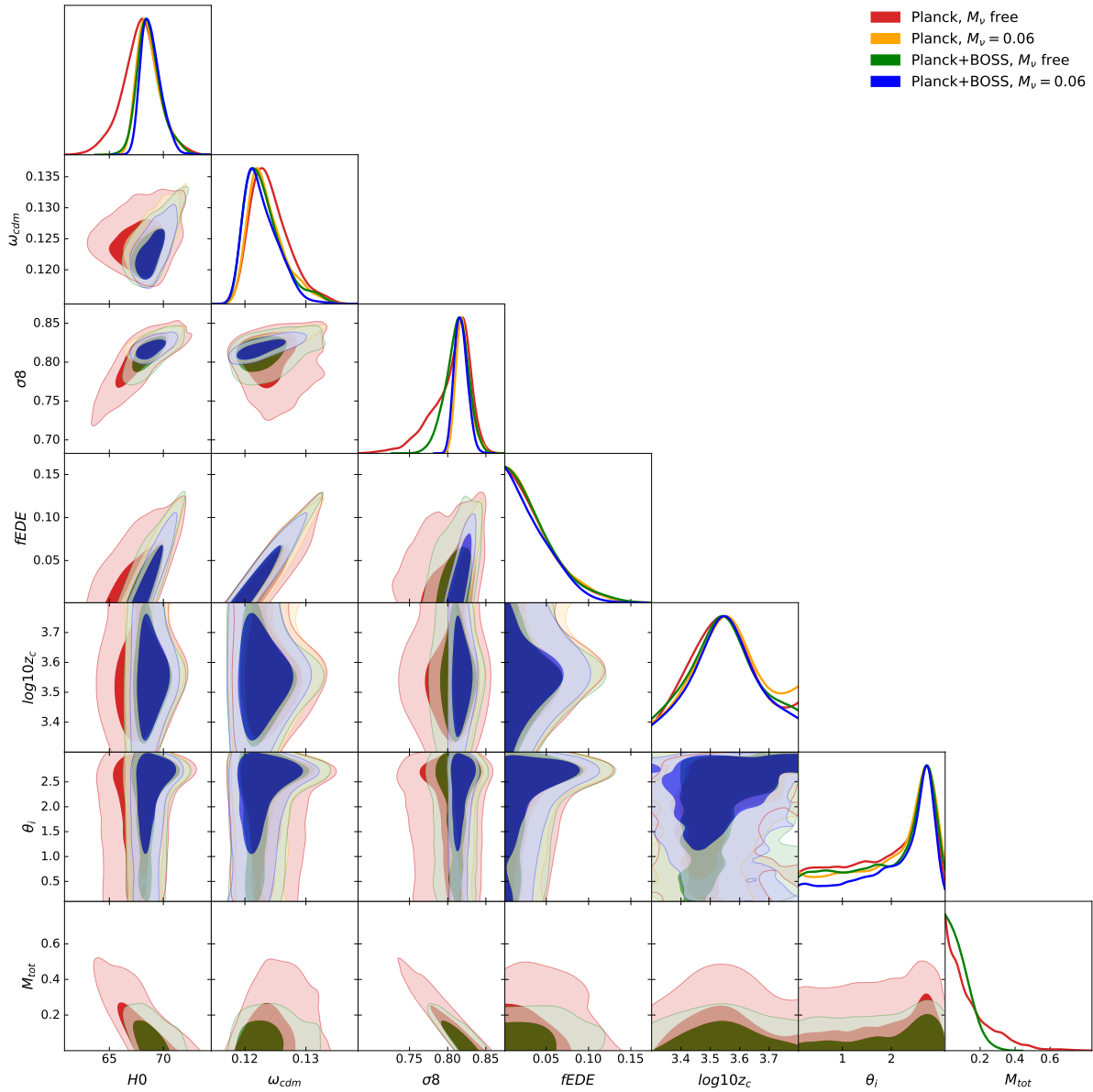


Figure 6.1: MCMC posteriors of the full 3-parameter EDE model for *Planck*-only and *Planck*+BOSS full-shape data. Varying the sum of neutrino masses, M_ν (red, green), has little impact on the constraints compared to fixing $M_\nu = 0.06$ eV (yellow, blue).

follow the methodology in Smith *et al.* (2021) and fix $\log_{10}(z_c) = 3.569$ and $\theta_i = 2.775$ (this corresponds to their best-fitting parameters to *Planck*-only data). This ‘1-parameter model’ (see also Sec. 2.6) is shown in Fig. 6.2 for M_ν free (red, green) and $M_\nu = 0.06$ eV fixed (yellow, blue). As was already noted in Smith *et al.* (2021), the 1-parameter model is only suitable to check for qualitative trends since fixing two parameters of the model is not a full Bayesian analysis. Nevertheless, it already gives insight into possible degeneracies between cosmological parameters that open up due to varying f_{EDE} and M_ν . We monitor convergence with the Gelman-Rubin criterion (Gelman and Rubin, 1992) and take $R - 1 < 0.05$ as a limit.⁴

Within the 1-parameter model, the 68% confidence level (C.L.) for the *Planck* and BOSS (in parentheses, *Planck*-only) data set on the fraction of EDE are $f_{\text{EDE}} = 0.077_{-0.035}^{+0.038}$ ($f_{\text{EDE}} = 0.076_{-0.039}^{+0.039}$) when varying M_ν . For both data sets, the constraints do not change significantly with M_ν fixed: $f_{\text{EDE}} = 0.075_{-0.037}^{+0.033}$ ($f_{\text{EDE}} = 0.077_{-0.04}^{+0.037}$). For the *Planck*-only data set, varying M_ν broadens the error bar on $\sigma_8 = 0.832_{-0.037}^{+0.059}$ towards lower values compared to fixing M_ν , which gives $\sigma_8 = 0.881_{-0.025}^{+0.022}$, therefore, leading to a better agreement with direct measurements of σ_8 from WL experiments, e.g. DES ($\sigma_8 = 0.733_{-0.049}^{+0.039}$, Abbott *et al.*, 2022). When adding BOSS full-shape data, the mean shifts to lower values and the error bars broaden when varying M_ν , $\sigma_8 = 0.818_{-0.014}^{+0.018}$, compared to fixing M_ν , $\sigma_8 = 0.826_{-0.012}^{+0.0095}$. The results from the 1-parameter model hint to a possible degeneracy between M_ν and σ_8 . To further explore this degeneracy, we employ the frequentist profile likelihood in the next section.

6.5 Profile likelihood analysis

We perform a profile-likelihood analysis, fixing M_ν to seven values between 0.06 eV and 0.3 eV and dissecting each likelihood’s contribution to the total χ^2 . Technical details concerning the convergence of the profile-likelihood analysis are given in the supplementary material 6.7.3. We aim to identify *a*) which data set(s) prevent high M_ν values, and *b*) whether prior volume effects are playing a role. Smith *et al.* (2020), Herold *et al.* (2022), and Gómez-Valent (2022) argued that prior volume effects play a key role with EDE, as in the $f_{\text{EDE}} \rightarrow 0$ limit Λ CDM is recovered, so the likelihood is approximately flat in the θ_i and z_c directions. This leads to a larger prior volume in the low- f_{EDE} region, resulting in a preference for small f_{EDE} upon marginalization. The profile likelihood is not impacted by these prior volume effects.

Our profile-likelihood analysis results are shown in Fig. 6.3 and Tab. 6.1. We find that the baseline EDE model ($M_\nu = 0.06$ eV) with $f_{\text{EDE}} = 0.077$ fits the data best. This has a $\Delta\chi^2 = -5.6$ compared to the baseline Λ CDM model although we have introduced three extra parameters (when fixing M_ν). The best-fit f_{EDE} for this model is significantly higher than the mean value expected from the Bayesian results for the baseline model with $M_\nu = 0.06$ eV, hence we reconfirm the results of Herold *et al.* (2022) that prior volume effects could have an impact on the Bayesian constraints of the baseline EDE model. However, even without prior volume effects, the profile-

⁴Note that not all parameters of the full 3-parameter MCMC shown in Fig. 6.1 satisfy this criterion.

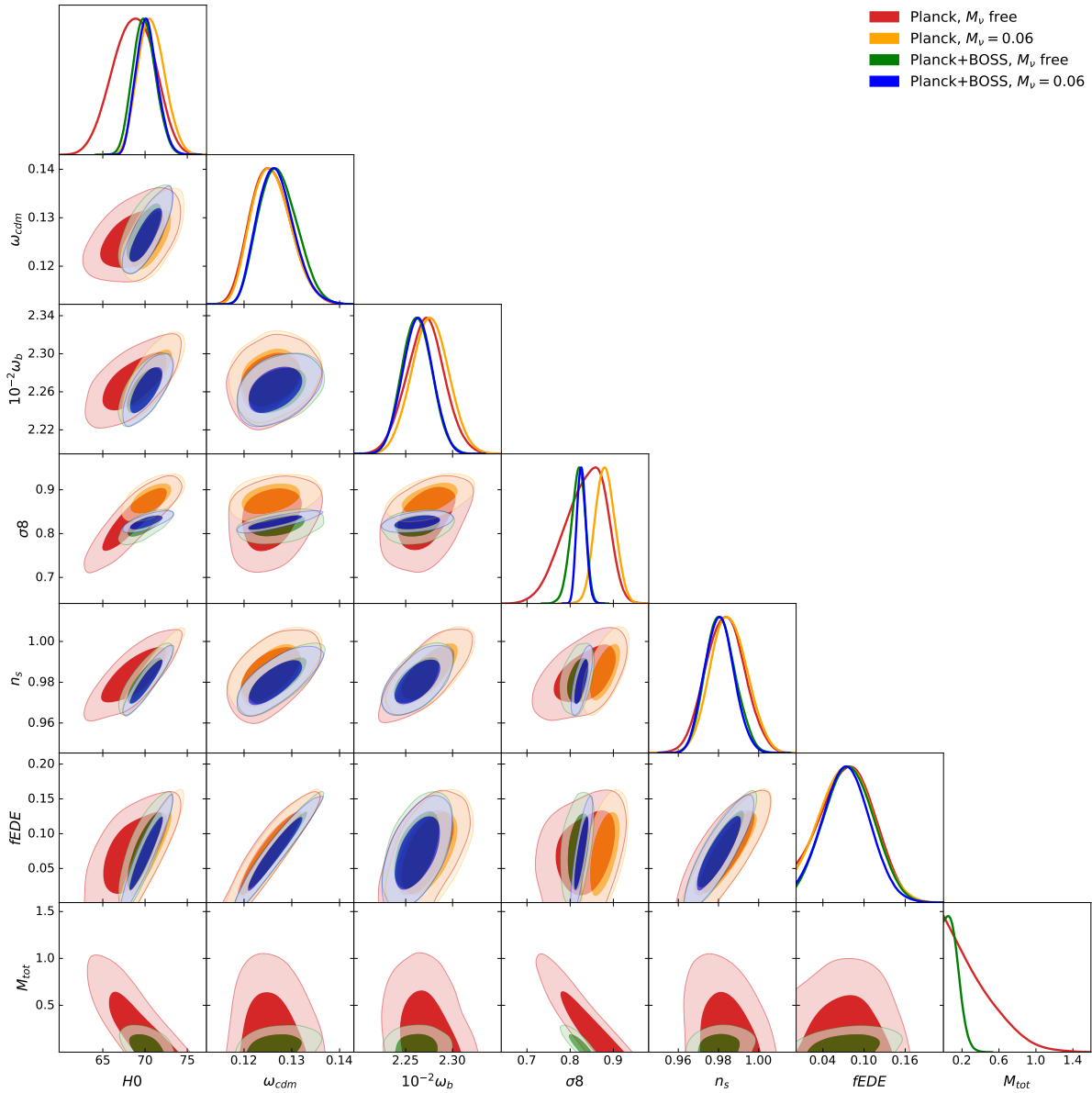


Figure 6.2: MCMC posteriors of the 1-parameter EDE model, with z_c, θ_i fixed. The constraints on σ_8 loosen when varying M_ν (red, green) compared to fixing $M_\nu = 0.06$ eV (yellow, blue). Although fixing two parameters of the model helps to mitigate prior volume effects, it is not a full Bayesian analysis and is only suitable to infer qualitative trends.

		Best-fit χ^2 contributions							
\mathcal{L}	Model	$\Lambda\text{CDM}_{0.06}$	EDE _{0.06}	EDE _{0.09}	EDE _{0.12}	EDE _{0.15}	EDE _{0.18}	EDE _{0.24}	EDE _{0.3}
BOSS (BAO+FS)		297.2	295.3	295.4	295.5	295.9	296.5	298.2	301.9
<i>Planck</i> TTTEEE		2345.5	2342.6	2343.2	2343.7	2345.1	2345.5	2347.2	2348.3
<i>Planck</i> lowE		396.3	396.1	396.4	396.8	396.5	397.0	397.3	397.7
<i>Planck</i> lowl		23.2	21.9	21.7	21.5	21.3	21.2	21.1	21.1
<i>Planck</i> lensing		8.8	9.47	9.34	9.18	9.15	9.07	9.01	9.07
Total χ^2 (S21)		3071.0	3065.4	3065.9	3066.7	3067.9	3069.3	3072.9	3078.1
		Best-fit parameters							
H_0 [km/s/Mpc]		67.59	70.08	69.96	69.97	70.12	70.12	70.11	69.42
σ_8		0.811	0.828	0.824	0.820	0.814	0.811	0.802	0.787
Ω_m		0.312	0.306	0.309	0.311	0.312	0.315	0.319	0.325
S_8		0.827	0.837	0.836	0.834	0.831	0.831	0.826	0.819
ω_c		0.120	0.127	0.128	0.128	0.129	0.130	0.131	0.130
f_{EDE}		–	0.077	0.082	0.089	0.099	0.107	0.117	0.117

Table 6.1: *Upper half*: breakdown of the best-fit χ^2 contributions from BOSS (BAO + full-shape, FS) and each *Planck* likelihood and the total best-fit χ^2 , within different models (“EDE_{*x*}” indicates an EDE model with fixed $M_\nu = x$ eV). *Lower half*: best-fit values of H_0 , σ_8 , Ω_m , S_8 , ω_c and f_{EDE} within each model.

likelihood analysis shows no evidence for a higher M_ν in the EDE model. Lowering S_8 to the ΛCDM level within EDE requires about $M_\nu \sim 0.24$ eV ($S_8 = 0.826$, $f_{\text{EDE}} = 0.117$). This comes at the cost of a substantially worse fit quality ($\Delta\chi^2 = 7.5$).

The profile likelihood in M_ν , broken down into the χ^2 contributions from the individual datasets in our analysis is shown in the blue and purple lines in Fig. 6.3 (top). We find that the fit to both the *Planck* TTTEEE + lensing and the BOSS data worsens as M_ν is increased. For the *Planck* data the strong constraining power on M_ν is expected (Aghanim *et al.* (2020b) for ΛCDM). More interestingly, the fit to the BOSS dataset also degrades monotonically with M_ν : this suggests that the benefits of increased M_ν in the EDE scenario in terms of a reduction in clustering amplitude are being outweighed by an increasing mismatch to the geometric features of the full-shape spectrum. We find that most of the effect of EDE-induced parameter shifts and M_ν on the full-shape clustering amplitude is re-absorbed by nuisance parameter shifts, as pointed out in Ivanov *et al.* (2020a) within baseline EDE (see also supplementary material 6.7.2). The remaining differences in the galaxy power spectrum multipoles are due to a mismatch in the location of the BAO wiggles. Hence, the derived constraints on the EDE+ M_ν model are mostly driven by shifts in the BAO scale θ_{BAO} , rather than the M_ν -driven small-scale power suppression. In Fig. 6.4 we show how the fit to the BAO scale gradually worsens as M_ν increases, reflecting the increasing trend in the BOSS likelihood χ^2 .

We show the correlations of H_0 , S_8 , and f_{EDE} with the fixed value of M_ν in Fig. 6.3 (bottom).

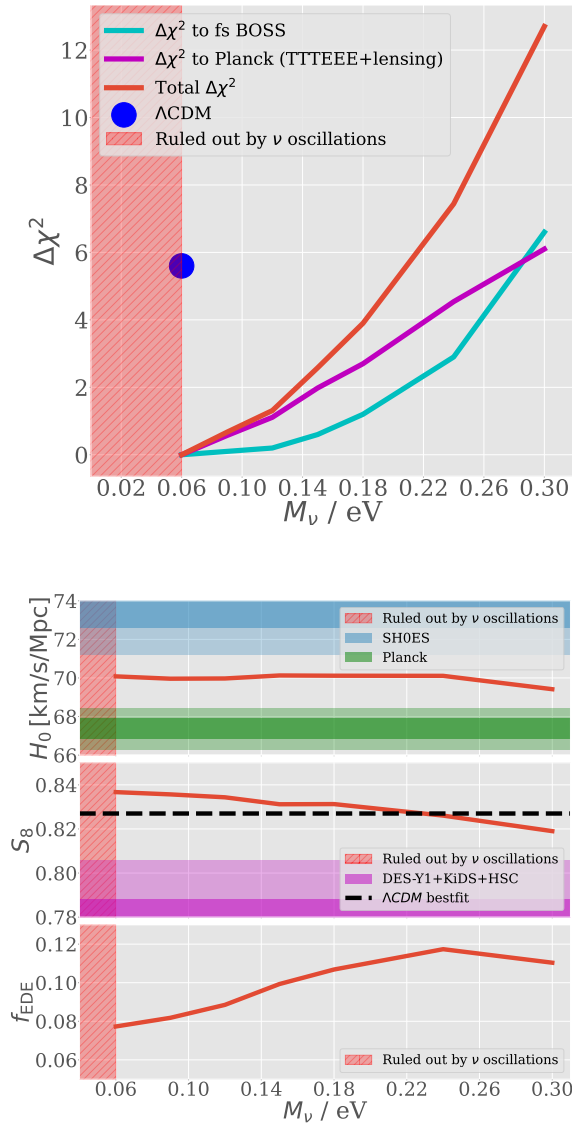


Figure 6.3: *Top*: χ^2 contributions as a function of M_ν within the EDE model. The purple and blue lines respectively show the χ^2 contribution from the *Planck* and BOSS likelihoods and the red line is the total χ^2 , given by the sum of the two. The blue dot represents the best-fit Λ CDM model, given the same combination of data. The red shaded region encompasses values of M_ν which are ruled out by oscillation experiments. *Bottom*: Variation in the best-fit values of selected cosmological parameters as a function of M_ν . The red shaded region encompasses values of M_ν that are ruled out by oscillation experiments. The blue and green bands indicate respectively the value of H_0 inferred from *Planck* assuming the Λ CDM model (Aghanim *et al.*, 2020b), and the SH0ES local distance ladder value (Riess *et al.*, 2022). The purple band is an inverse-variance-weighted combination of DES-Y1+KiDS+HSC S_8 measurements as in Hill *et al.* (2020), whilst the black dashed line is the best-fit value of S_8 from a fit to the same datasets assuming Λ CDM.

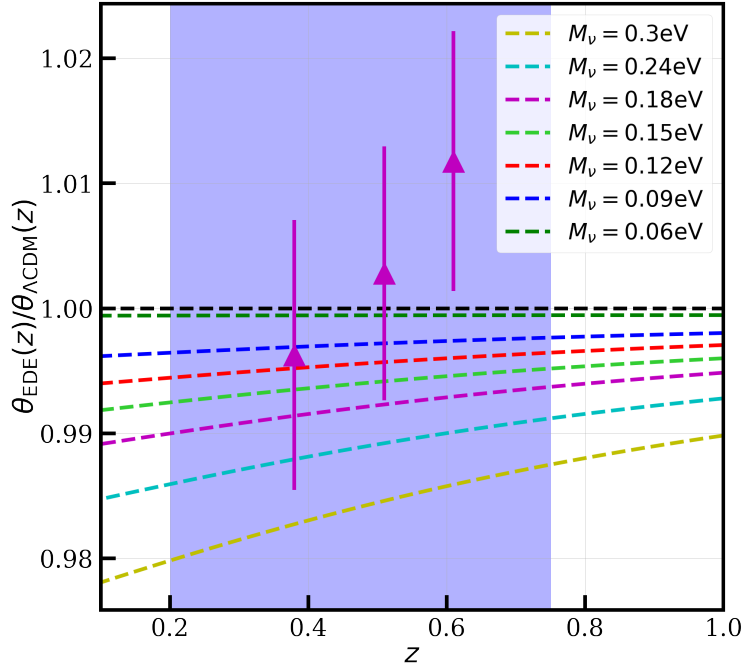


Figure 6.4: BAO angular scale within EDE at fixed values of M_ν relative to the ΛCDM predictions (all parameters fixed to their *Planck*+BOSS best fits). Purple triangles denote the BOSS DR12 consensus isotropic BAO measurements (Alam *et al.*, 2017).

As expected, we find that S_8 decreases with increasing M_ν since neutrino free-streaming is able to suppress clustering. We also find a positive correlation between M_ν and f_{EDE} , which can be understood by the effect of M_ν and f_{EDE} on the BAO scale, θ_{BAO} : if θ_s and $\omega_b + \omega_c$ is assumed to be fixed, increasing M_ν leads to a decrease of H_0 and consequently a decrease of θ_{BAO} at $z \lesssim 1$ (Hou *et al.*, 2014; Archidiacono *et al.*, 2017). Increasing f_{EDE} on the other hand, leads to an increase of r_{drag} and with that an increase in H_0 , which together results in a decrease of $D_V(z_{\text{eff}})$ increasing θ_{BAO} . Hence, increasing f_{EDE} can partly compensate for the M_ν -induced decrease of θ_{BAO} . This compensation is not perfect and θ_{BAO} still decreases while increasing M_ν . However, the extent to which f_{EDE} can be increased is limited by the increase in ω_c (compensating the eISW boost). As a result, the best-fit H_0 barely shifts when M_ν is raised.

For $M_\nu \gtrsim 0.18 \text{ eV}$ the χ^2 increases more steeply, mostly driven by the BOSS likelihood due to the gradually worsened BAO scale fit. However, H_0 remains stable within 1% across the whole M_ν range, due to two competing effects: while increasing f_{EDE} pulls H_0 upwards, increasing M_ν lowers it due to the geometrical degeneracy.

6.6 Conclusions

It is well known that introducing EDE in order to resolve the H_0 tension worsens the “ S_8 tension”. This chapter re-examines this issue in light of an extension including massive neutrinos, driven by the possibility of their small-scale power suppression counteracting the EDE-induced excess power, which leads to the increase in S_8 .

A standard Bayesian analysis of CMB and galaxy clustering data shows that freeing M_ν does not increase the inferred f_{EDE} , and has no effect on EDE’s standings relative to the H_0 and S_8 tensions. A frequentist profile-likelihood analysis also finds no clear benefits for EDE resulting from a higher M_ν , as the best fit is achieved within baseline EDE ($M_\nu = 0.06$ eV), but supports earlier claims of prior volume effects playing a key role in these Bayesian constraints using BOSS data (Smith *et al.*, 2021; Herold *et al.*, 2022; Gómez-Valent, 2022). Values of M_ν lowering S_8 to the Λ CDM level are not preferred statistically; a model with $M_\nu = 0.24$ eV worsens the fit by $\Delta\chi^2 = 7.5$ in comparison to baseline EDE. We find a correlation between f_{EDE} and M_ν , along with the expected negative M_ν - S_8 correlation.

Our M_ν limits are driven not by the full-shape clustering amplitude (re-absorbed by nuisance parameters), but by shifts in the BAO scale, θ_{BAO} . As the clustering amplitude plays a minor role, our analysis is not very sensitive to the benefits of the M_ν -driven power suppression. One possible avenue for further work would be to explore the inclusion of WL data or WL-derived priors which, without freeing M_ν , appear to slightly decrease the value of f_{EDE} and consequently H_0 (Herold and Ferreira, 2022); it will be interesting to study whether freeing M_ν can improve the consistency of EDE with WL measurements.

In the coming years, β -decay experiments will aim for a model-independent kinematical neutrino mass detection which, combined with future cosmological probes (Ade *et al.*, 2019; Abitbol *et al.*, 2019), will set the stage for further tests of EDE and massive neutrinos.

6.7 Supplementary material

6.7.1 MCMC for different data set combinations

In Figs. 6.5 and 6.6, we show the posteriors of the full 3-parameter MCMC model for different data-set combinations. For this analysis, we use *Planck* CMB temperature, polarization and CMB lensing (Aghanim *et al.*, 2020b), the BAO and the redshift-space distortion data from BOSS (Alam *et al.*, 2017), the BAO measurements from the 6-degree Field Galaxy Survey (6dFGS; Beutler *et al.*, 2011) and Sloan Digital Sky Survey Main Galaxy Sample (SDSS MGS; Ross *et al.*, 2015), the Pantheon supernova sample (SNIa, Scolnic *et al.*, 2022), and the direct measurement by the SHOES collaboration (Riess *et al.*, 2019). Additionally, we use data from the WL survey DES (Abbott *et al.*, 2018b).

Similar to the posteriors of the full 3-parameter EDE model using *Planck* and BOSS full-shape data in Fig. 6.1, we find almost no difference between the constraints on the cosmological parameters when M_ν is free (solid lines) or fixed to $M_\nu = 0.06$ eV (dashed lines) for all data sets we considered. Fig. 6.6 resembles Fig. 1 in Hill *et al.* (2020) but with varying M_ν (dashed lines).

6.7.2 Shifts in nuisance parameters

To illustrate the parameter shifts in the nuisance parameters, we plot in Fig. 6.7 the minimization chains, which are chains with iteratively decreasing step size and enhanced sensitivity to the likelihood difference (Schöneberg *et al.*, 2022). Hence, the smoothed contours in Fig. 6.7 are **not** posteriors but are only a qualitative indication of the position of the best-fitting nuisance parameters. We find that fixing M_ν to different values leads to up to 10% shifts in the nuisance parameters, which include three bias parameters (b_1, b_2, b_{G_2}), two counterterms (c_0, c_2) and shot noise (P_{shot}).

6.7.3 Details about the convergence of the profile-likelihood analysis for cosmologies with EDE and neutrinos

In Ch. 6, we compute profile likelihoods in M_ν with all EDE parameters $\{f_{\text{EDE}}, z_c, \theta_i\}$ and all Λ CDM parameters free, while in Ch. 4 and Ch. 5, we computed profile likelihoods in f_{EDE} with only two EDE parameters $\{z_c, \theta_i\}$ and all Λ CDM parameters free. Due to the additional free parameter, M_ν , the minimization procedure in Ch. 6 led to longer convergence times and more problems with local minima. Since the minimization procedure is based on the running of MCMC chains (Schöneberg *et al.*, 2022), the minimization can be affected by the larger prior volume in $f_{\text{EDE}} \approx 0$ similar to the MCMC inference: due to the larger prior volume at smaller values of f_{EDE} , the minimization chains spend more time around $f_{\text{EDE}} \approx 0$ and are less likely to find the global minimum of χ^2 if it lies at $f_{\text{EDE}} \gg 0$ and stay in a local minimum instead. One can mitigate this effect by running several minimizations with different starting positions and covariance matrices⁵ In the following, we describe how we ran four iterations of minimizations in order to mitigate the problem of local minima.

Run 1

The first iteration (referred to as **run 1**) is based on the covariance obtained from seven full MCMC analysis (until $R - 1 < 0.3$, Gelman and Rubin, 1992) with the sum of neutrino masses fixed to $M_\nu[\text{eV}] = \{0.06, 0.09, 0.12, 0.15, 0.18, 0.24, 0.3\}$. For each minimization with fixed value of M_ν , we run with the respective covariance and best fit from the MCMC. For the MCMC, we

⁵The covariance matrix determines the relative step sizes in the different parameter directions.

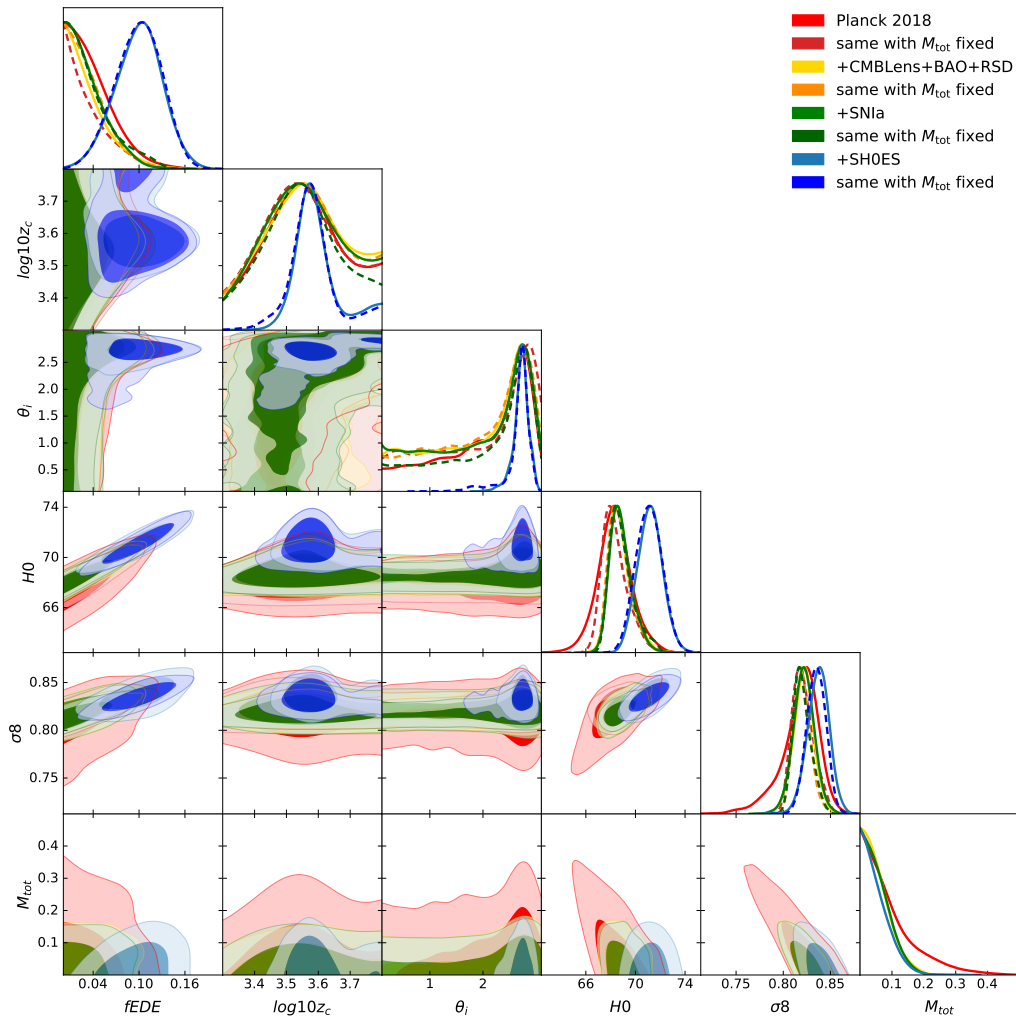


Figure 6.5: MCMC posteriors of the full 3-parameter EDE model for *Planck* CMB, CMB lensing, BAO, RSD, Pantheon SNIa and the SH0ES direct H_0 measurement. We explore the impact of varying the sum of neutrino masses, M_ν (solid lines), compared to fixing $M_\nu = 0.06$ eV (dashed lines), and find little impact on the cosmological constraints. Note that the MCMC posteriors can be influenced by prior volume effects.

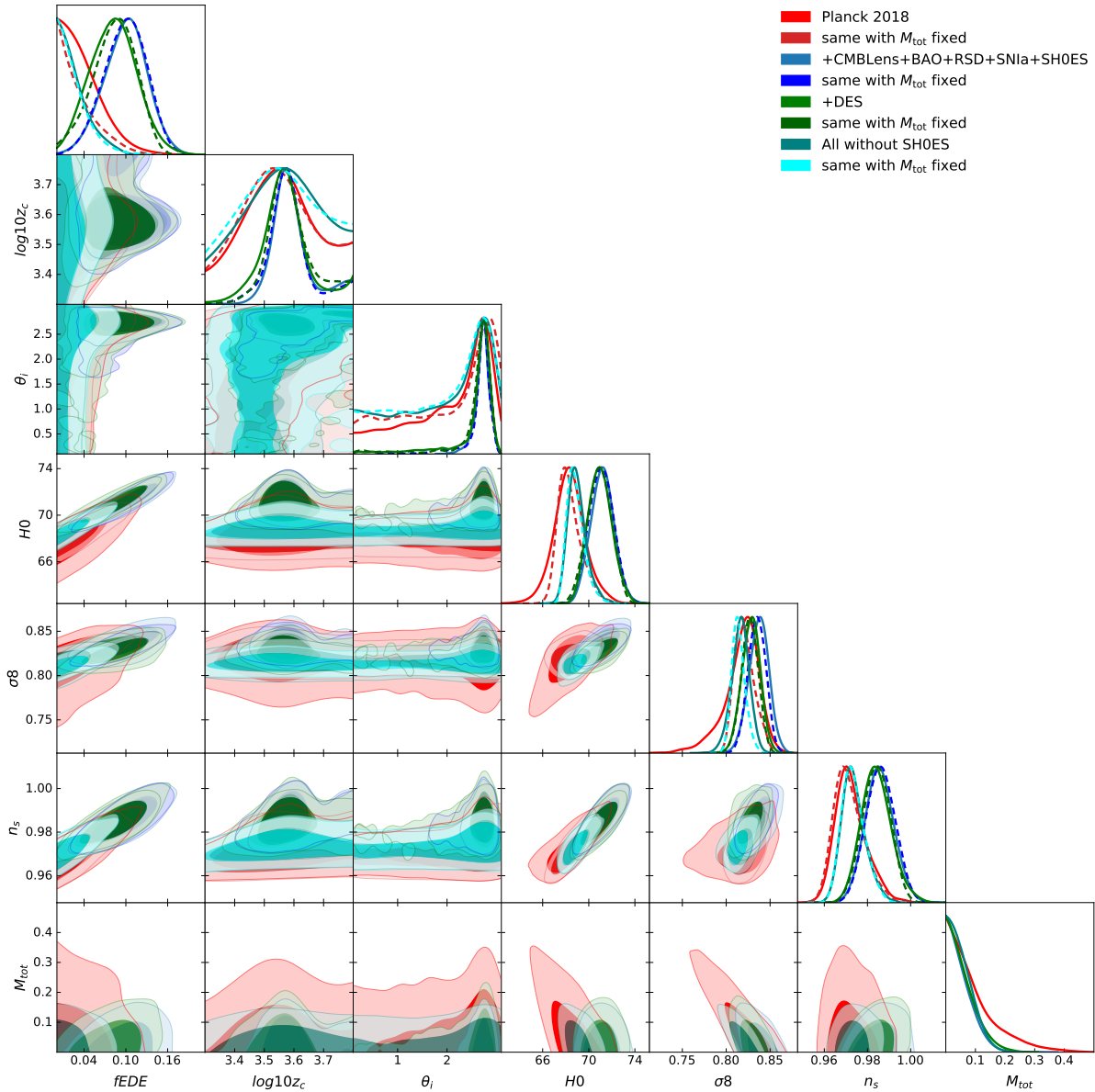


Figure 6.6: MCMC posteriors of the full 3-parameter EDE model for *Planck* CMB, CMB lensing, BAO, RSD, DES, Pantheon SNIa and the SHOES direct H_0 measurement. We explore the impact of varying the sum of neutrino masses, M_ν (solid lines), compared to fixing $M_\nu = 0.06 \text{ eV}$ (dashed lines), and find little impact on the cosmological constraints.

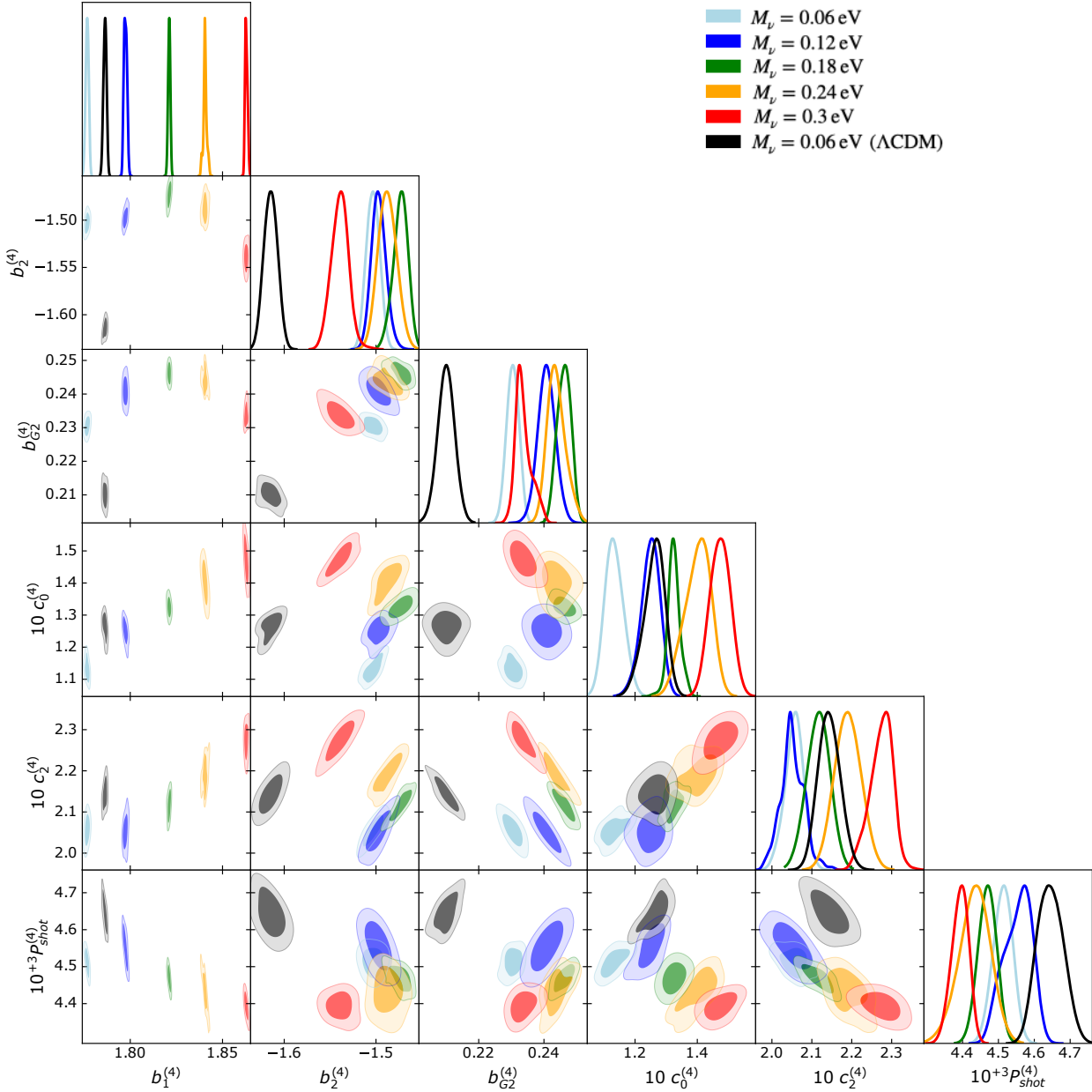


Figure 6.7: Smoothed minimization chains of the full 3-parameter EDE model for *Planck* and BOSS BAO + full-shape for different M_ν (solid lines). Note that these are not posteriors but solely for illustrating the shifts in the approximate best-fit values of the EFT-of-LSS nuisance parameters.

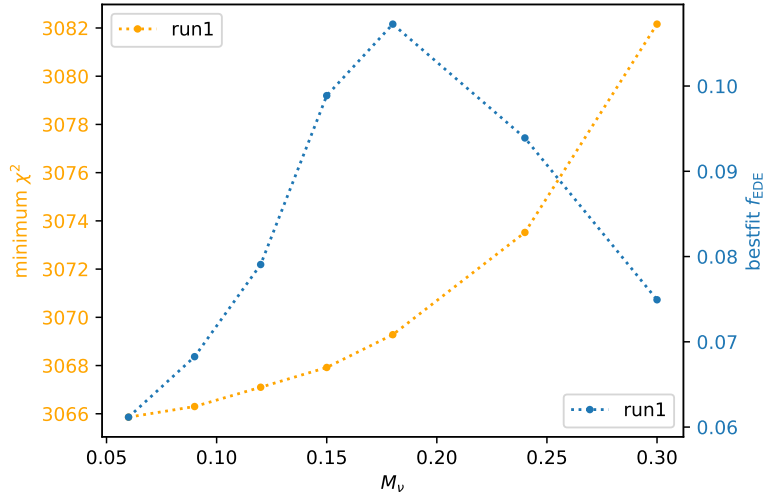


Figure 6.8: Profile likelihood in M_ν for **run 1** (orange, left axis) and the corresponding best-fit f_{EDE} for each M_ν (blue, right axis).

compute the theory model with the code from Herold *et al.* (2022)⁶, which combines the two extension of CLASS (Lesgourgues and Pastor, 2006): CLASS-PT (Chudaykin *et al.*, 2020) and CLASS_EDE (Hill *et al.*, 2020), while for the minimization, we use EDE_class_pt (Ivanov *et al.*, 2020a)⁷. We show the profile likelihood, i.e. minimum χ^2 as a function of M_ν , obtained from **run 1** in Fig. 6.8.

We find that the profile likelihood (orange, left axis) follows a smooth parabola. However, the corresponding best-fit values of f_{EDE} as a function of the fixed values of M_ν peaks at $M_\nu = 0.18$ and decreases for $M_\nu > 0.18$. Note also that the first data point ($M_\nu = 0.06$ eV) corresponds to the case that we explored in Ch. 4, where we found $f_{\text{EDE}} = 0.072$ for *Planck* + BOSS full-shape and $f_{\text{EDE}} = 0.077$ for *Planck* + BOSS full-shape+BAO, whereas here with the minimization of the full 3-parameter model we find only $f_{\text{EDE}} = 0.061$. These two observations indicate that the minimization could be stuck in a local minimum.

Run 2 and run 3

In order to check whether **run 1** did find the global minimum of χ^2 for all fixed values of M_ν , we run two further iterations of minimizations. From now on, we use EDE_class_pt (Ivanov *et al.*, 2020a) for the MCMC to compute the covariance and for the minimizations. For **run 2**, we used an intermediate estimate of the covariance (after only one or two days of running the MCMC), whereas for **run 3**, we used the final covariance (with at least 10,000 steps and $R - 1 < 0.3$, taking > 5 days). Hence, naively **run 3** should be the run with the best convergence so far. Both

⁶https://github.com/LauraHerold/CLASS-PT_EDE

⁷https://github.com/Michalychforever/EDE_class_pt

min. χ^2	0.06	0.09	0.12	0.15	0.18	0.24	0.3
run1	3065.86	3066.30	3067.10	3067.92	3069.28	3073.52	3082.16
run2	3065.46	3066.04	3066.80	-	3071.30	3073.16	3079.12
run3	3065.50	3066.00	3066.80	3068.02	3071.00	3072.94	3078.18
run4	3065.40	3065.88	3066.70	3067.90	3069.28	3072.90	3077.92

Table 6.2: Minimum χ^2 for **run 1** to **4** for M_ν fixed to 0.06-0.3 eV. The minimum among **run 1** to **3** is shown in boldface.

runs along with **run 1** and **4** are shown in Fig. 6.9. We find that **run 2** and **run 3** are evidently stuck in local minima for $M_\nu = 0.18$ but they out-perform **run 1** for $M_\nu = 0.3$. We show the values of minimum χ^2 for **run 1** to **4** in Tab. 6.2. Note that **run 2** finds for $M_\nu = 0.06$ eV a best-fit $f_{\text{EDE}} = 0.077$, which agrees with the result obtained in Ch. 4; this confirms that **run 1** was stuck in a local minimum for $M_\nu = 0.06$ eV.

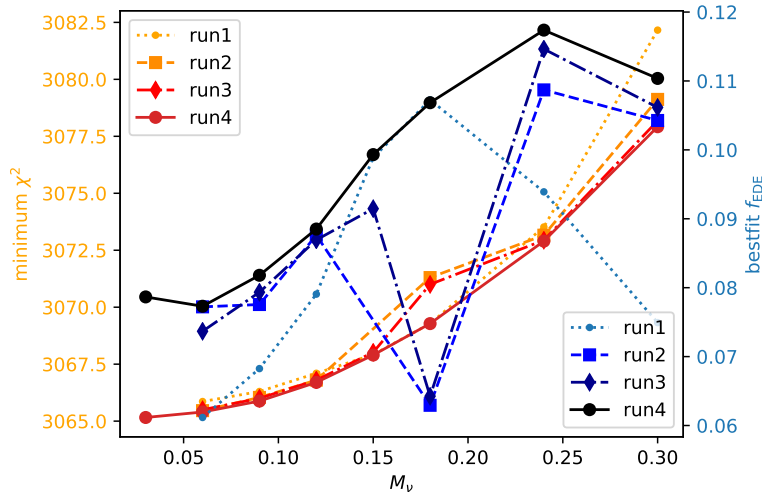


Figure 6.9: Profile likelihood in M_ν for **run 1, 2, 3, 4** (red-orange colors, left axis) and the corresponding best-fit f_{EDE} for each M_ν (blue colors, right axis).

Run 4

To verify the minima found before, we started a fourth iteration, which uses the full covariance based on the theory model `EDE_class_pt` (Ivanov *et al.*, 2020a) but starts at the best-fit positions marked in bold face in Tab. 6.2. The results of **run 4** are shown in Fig. 6.9 (dark, solid lines). **Run 4** outperforms all runs, which is expected since we started from the best-fit cosmologies found before. The minimum χ^2 is shown in the fourth row of Tab. 6.2.

Fig. 6.10 shows the final profile-likelihood results (orange, left axis) used in Sec. 6.5 with a parabola fit (grey). The corresponding best-fit values of f_{EDE} (blue, right axis) still show a decrease at $M_\nu = 0.3$. This could be caused by a local minimum but does not influence the main conclusions in Ch. 6.

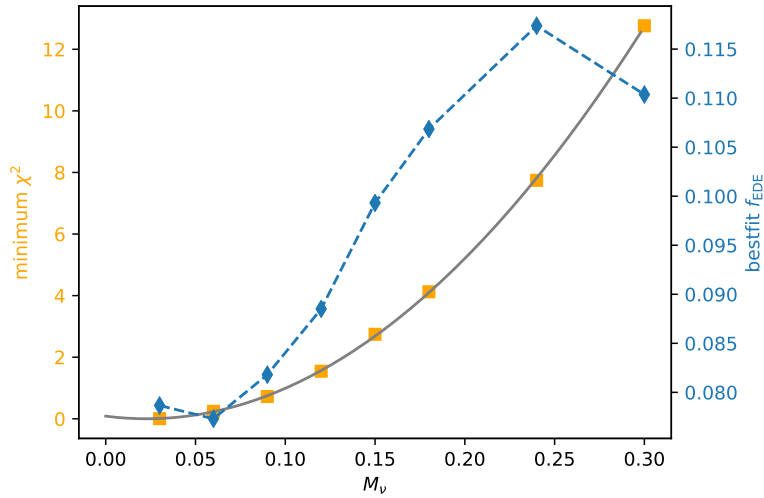


Figure 6.10: Final profile likelihood in M_ν based on **run 4** (orange colors, axis) and the corresponding best-fit f_{EDE} for each M_ν (blue, right axis). We show a parabola fit to the profile likelihood (solid, grey line). By running four iterations, we could mitigate the effect of local minima and obtain a smooth estimate of the profile likelihood.

Acknowledgements

We thank George Efstathiou, Colin Hill, Eiichiro Komatsu and Oliver Philcox for many useful discussions. S.V. was partially supported by the Isaac Newton Trust and the Kavli Foundation through a Newton-Kavli Fellowship, and by a grant from the Foundation Blanceflor Boncompagni Ludovisi, née Bildt. B.D.S. is supported by the European Research Council (Grant agreement No. 851274) and an STFC Ernest Rutherford Fellowship. The Kavli IPMU is supported by World Premier International Research Center Initiative (WPI), MEXT, Japan.

Chapter 7

Conclusions and Outlook

In this thesis, we used both frequentist and Bayesian methods to answer the question whether Early Dark Energy (EDE) can simultaneously resolve the Hubble tension and present a good fit to cosmic microwave background (CMB) and large-scale structure (LSS) data. We find that the results from Bayesian Markov Chain Monte Carlo (MCMC) analyses are affected by prior volume effects, which lead to a preference for small fractions of EDE, disfavoring EDE as a solution to the Hubble tension (Ch. 4). Using a profile-likelihood analysis, we find that models with tension-resolving amounts of EDE present a good fit to *Planck* CMB, Baryon Oscillation Spectroscopic Survey (BOSS) full-shape galaxy clustering data and Dark Energy Survey (DES) weak lensing data (included as a Gaussian likelihood on the clustering amplitude, S_8). For all data sets considered in this thesis, we find that the tension with the SH0ES direct measurement of the Hubble constant is reduced below 1.7σ (Ch. 5). Further, we consider an extension of the EDE model that includes the sum of neutrino masses, M_ν , as a free parameter, in order to assess whether a higher M_ν can help to reduce the S_8 tension. A profile-likelihood analysis in M_ν revealed a positive correlation between M_ν and the fraction of EDE, which enables a lower S_8 while resolving the Hubble tension. However, values of M_ν that sufficiently suppress S_8 are disfavored by *Planck* and BOSS data (Ch. 6).

The results in this thesis demonstrate the complementarity of Bayesian credible intervals from MCMC and frequentist confidence intervals from the profile likelihood. Of course, no method is superior but both methods address different questions and give complementary answers: While Bayesian credible intervals include prior knowledge and localize bulk volumes in parameter space that fit the data well, the frequentist confidence intervals do not include prior knowledge and are based only on the maximum likelihood estimate, regardless of the size of the parameter volume. Therefore, both methods have different shortcomings: While the Bayesian credible intervals can be subject to prior volume effects, the frequentist confidence intervals can be subject to fine tuning, i.e. they can prefer very small volumes in parameter space that are physically not well motivated. Once the data reach sufficient statistical power, both methods will give equivalent results. However, until then, we believe that it is important to use both Bayesian and frequentist methods as complementary tools to mitigate the shortcomings of both methods.

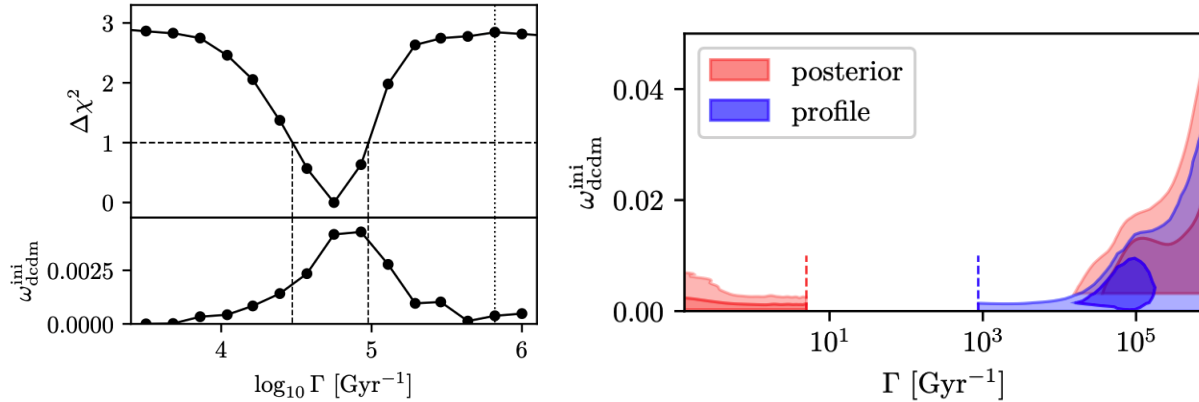


Figure 7.1: Profile likelihood results of the initial energy density fraction of DCDM, $\omega_{\text{dcdm}}^{\text{ini}}$, and decay rate, Γ . *Left*: 1-dimensional profile likelihood in $\log_{10} \Gamma$ (top subplot) with corresponding best-fitting values of $\omega_{\text{dcdm}}^{\text{ini}}$ (bottom subplot). *Right*: 2-dimensional profile likelihood in $\omega_{\text{dcdm}}^{\text{ini}}$ and Γ (blue) compared to the MCMC posterior (red). While the posterior prefers either very long- or short-lived DCDM, the profile likelihood slightly favors an intermediate regime. Taken from Holm *et al.* (2023).

Understanding the influence of prior volume effects is not only important for the EDE model but is important also for other beyond- Λ CDM models. The reason for the strong influence of prior volume effects in the EDE model is the parametrization of the model, which has a structure that is common for many beyond- Λ CDM models: The model introduces several additional parameters and reduces to Λ CDM once the abundance of the beyond- Λ CDM energy density approaches zero. In this limit, all other parameters of the extended model are unconstrained, which leads to an enhanced prior volume and with that an up-weighting of the Λ CDM limit in cases where there is no clear preference for the beyond- Λ CDM model.

One recent example, where prior volume effects were shown to have a strong influence is *decaying cold dark matter* (DCDM), where a fraction of dark matter (DM) decays into invisible dark radiation with a certain lifetime. Studies using Bayesian methods show that CMB data either prefer the very short-lived regime, i.e. a fraction of DM decays immediately, which corresponds to the Λ CDM model with extra dark radiation, or the very long-lived regime, which corresponds to the standard Λ CDM model (Nygaard *et al.*, 2021; Holm *et al.*, 2022). Using profile likelihoods to constrain the energy density fraction of DCDM, ω_{dcdm} , and the decay rate, Γ , which corresponds to the inverse of the lifetime, Holm *et al.* (2023) find that prior volume effects are important. The results of this study are shown in Fig. 7.1. Opposed to the Bayesian credible intervals, which prefer either very large or very small values of Γ , the profile likelihood slightly favors an intermediate regime, where a small fraction of DM (about 3%) decays with a decay rate $\log_{10}(\Gamma \cdot \text{Gyr}) = 4.76^{+0.24}_{-0.29}$. The preferred Γ corresponds to a decay around recombination, which reveals interesting parallels to EDE, which is also important around recombination. Another example where the profile likelihood gives important complementary information compared to the Bayesian credible interval is New Early Dark Energy (NEDE). Cruz *et al.* (2023) find that while

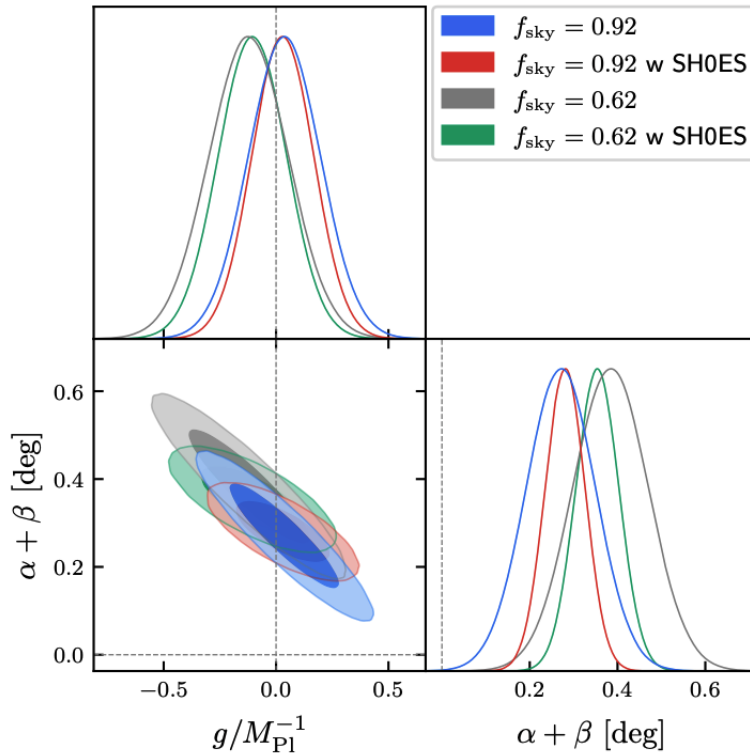


Figure 7.2: Posterior distribution of the parity-violating coupling of EDE and photons with coupling constant, g , and instrumental miscalibration and cosmic birefringence, $\alpha + \beta$, for two different EDE models (with/without SH0ES) and two sky cuts. *Planck* data prefers $\alpha + \beta$ as an explanation for the EB-correlation data. Taken from Eskilt *et al.* (2023).

the Bayesian credible interval gives tight upper limits on the fraction of NEDE when all parameters of the model are varied, the profile likelihood prefers higher values of NEDE, which yield values of the Hubble constant that resolve the tension with the SH0ES experiment, very similar to the case of EDE.

The results presented in this thesis are also relevant for future research on EDE. Since we find that EDE is not ruled out by current CMB and LSS experiments, it is important to look for other signatures that give corroborating evidence for EDE or rule out the EDE model. One example for this is the possibility that EDE could be related to the observed signal of correlation in EB polarization data from *Planck* (see Komatsu, 2022, for a review). The axion-like EDE model could couple to photons in a parity-violating manner, which could explain the observed EB signal. Murai *et al.* (2023); Eskilt *et al.* (2023) find that *Planck* polarization data disfavor the predicted shape of EB-correlation from (pre-recombination) EDE with coupling constant, g , but prefer (post-recombination) cosmic birefringence, β , or instrumental miscalibration, α (see Fig. 7.2). This approach gives complementary insights into the micro-physics and potential of the axion-like EDE model.

While in this thesis, we find that the tension-resolving EDE model presents a good fit to current CMB and LSS data sets, future observational data will shed new light on this model. Next generation LSS experiments like HETDEX (Gebhardt *et al.*, 2021), DESI (Aghamousa *et al.*, 2016), PFS (Ellis *et al.*, 2014) and Euclid (Laureijs, 2011) will provide a crucial test for the EDE model by tightly constraining the clustering amplitude of the galaxy power spectrum, which is increased in EDE cosmologies compared to Λ CDM, and the Hubble parameter, $H(z)$, at different redshifts. Further, the preference of the EDE model over Λ CDM by ground-based CMB experiments like ACT (see Sec. 2.6.4) needs further investigation. CMB temperature and polarization data from current and future experiments like SPT (Dutcher *et al.*, 2021), ACT (Aiola *et al.*, 2020), Simons Observatory (Ade *et al.*, 2019), CMB-S4 (Abazajian *et al.*, 2019), and LiteBIRD (Allys *et al.*, 2022) will give insights about the reason behind this preference. Moreover, it will be crucial to confirm the robustness of the Hubble tension or find systematics in one or several of the measurements, which can explain the tension. New methods are being developed that give independent constraints on the Hubble constant (see Sec. 2.3). If the tension is confirmed to be caused by new physics, this will give important insights into particular models like EDE but more importantly may shed light on the general nature of the dark sector of the Universe.

Bibliography

- Abazajian, K. *et al.*, arXiv-eprints (2019), arXiv:1907.04473 [astro-ph.IM].
- Abbott, T. M. C. *et al.* (DES), Mon. Not. Roy. Astron. Soc. **480**, 3879 (2018a), arXiv:1711.00403 [astro-ph.CO].
- Abbott, T. M. C. *et al.* (DES), Phys. Rev. D **98**, 043526 (2018b), arXiv:1708.01530 [astro-ph.CO].
- Abbott, T. M. C. *et al.* (DES), Phys. Rev. D **105**, 023520 (2022), arXiv:2105.13549 [astro-ph.CO].
- Abdalla, E. *et al.*, JHEAp **34**, 49 (2022), arXiv:2203.06142 [astro-ph.CO].
- Abitbol, M. H. *et al.* (Simons Observatory), Bull. Am. Astron. Soc. **51**, 147 (2019), arXiv:1907.08284 [astro-ph.IM].
- Addison, G. E., Watts, D. J., Bennett, C. L., Halpern, M., Hinshaw, G., and Weiland, J. L., Astrophys. J. **853**, 119 (2018), arXiv:1707.06547 [astro-ph.CO].
- Ade, P. *et al.* (Simons Observatory), JCAP **02**, 056 (2019), arXiv:1808.07445 [astro-ph.CO].
- Ade, P. A. R. *et al.* (Planck), Astron. Astrophys. **571**, A16 (2014a), arXiv:1303.5076 [astro-ph.CO].
- Ade, P. A. R. *et al.* (Planck), Astron. Astrophys. **566**, A54 (2014b), arXiv:1311.1657 [astro-ph.CO].
- Aghamousa, A. *et al.* (DESI), arXiv-eprints (2016), arXiv:1611.00036 [astro-ph.IM].
- Aghanim, N. *et al.* (Planck), Astron. Astrophys. **594**, A11 (2016), arXiv:1507.02704 [astro-ph.CO].
- Aghanim, N. *et al.* (Planck), Astron. Astrophys. **641**, A5 (2020a), arXiv:1907.12875 [astro-ph.CO].
- Aghanim, N. *et al.* (Planck), Astron. Astrophys. **641**, A6 (2020b), arXiv:1807.06209 [astro-ph.CO].
- Agrawal, P., Cyr-Racine, F.-Y., Pinner, D., and Randall, L., arXiv-eprints (2019), arXiv:1904.01016 [astro-ph.CO].

- Aiola, S. *et al.* (ACT), JCAP **12**, 047 (2020), arXiv:2007.07288 [astro-ph.CO].
- Akaike, H., IEEE Transactions on Automatic Control **19**, 716 (1974).
- Alam, S. *et al.* (BOSS), Mon. Not. Roy. Astron. Soc. **470**, 2617 (2017), arXiv:1607.03155 [astro-ph.CO].
- Alam, S. *et al.* (eBOSS), Phys. Rev. D **103**, 083533 (2021), arXiv:2007.08991 [astro-ph.CO].
- Alexander, S. and McDonough, E., Phys. Lett. B **797**, 134830 (2019), arXiv:1904.08912 [astro-ph.CO].
- Allali, I. J., Hertzberg, M. P., and Rompineve, F., Phys. Rev. D **104**, L081303 (2021), arXiv:2104.12798 [astro-ph.CO].
- Allys, E. *et al.* (LiteBIRD), arXiv-eprints (2022), 10.1093/ptep/ptac150, arXiv:2202.02773 [astro-ph.IM].
- Aloni, D., Berlin, A., Joseph, M., Schmaltz, M., and Weiner, N., Phys. Rev. D **105**, 123516 (2022), arXiv:2111.00014 [astro-ph.CO].
- Anand, G. S., Tully, R. B., Rizzi, L., Riess, A. G., and Yuan, W., Astrophys. J. **932**, 15 (2022), arXiv:2108.00007 [astro-ph.CO].
- Archidiacono, M., Brinckmann, T., Lesgourgues, J., and Poulin, V., JCAP **02**, 052 (2017), arXiv:1610.09852 [astro-ph.CO].
- Archidiacono, M., Hannestad, S., and Lesgourgues, J., JCAP **09**, 021 (2020), arXiv:2003.03354 [astro-ph.CO].
- Asgari, M. *et al.* (KiDS), Astron. Astrophys. **645**, A104 (2021), arXiv:2007.15633 [astro-ph.CO].
- Audren, B., Lesgourgues, J., Benabed, K., and Prunet, S., JCAP **02**, 001 (2013), arXiv:1210.7183 [astro-ph.CO].
- Aylor, K., Joy, M., Knox, L., Millea, M., Raghunathan, S., and Wu, W. L. K., Astrophys. J. **874**, 4 (2019), arXiv:1811.00537 [astro-ph.CO].
- Baldauf, T., *Effective Field Theory in Particle Physics and Cosmology: Lecture Notes of the Les Houches Summer School: Volume 108, July 2017* (Oxford University Press, 2020) <https://academic.oup.com/book/0/chapter/372565490/chapter-pdf/45818469/oso-9780198855743-chapter-7.pdf> .
- Baldauf, T., Mirbabayi, M., Simonović, M., and Zaldarriaga, M., Phys. Rev. D **92**, 043514 (2015), arXiv:1504.04366 [astro-ph.CO].
- Ballesteros, G., Notari, A., and Rompineve, F., JCAP **11**, 024 (2020), arXiv:2004.05049 [astro-ph.CO].

- Bardeen, J. M., Phys. Rev. D **22**, 1882 (1980).
- Bashinsky, S. and Seljak, U., Phys. Rev. D **69**, 083002 (2004), arXiv:astro-ph/0310198.
- Baumann, D., Green, D., Meyers, J., and Wallisch, B., JCAP **01**, 007 (2016), arXiv:1508.06342 [astro-ph.CO].
- Baumann, D., Nicolis, A., Senatore, L., and Zaldarriaga, M., JCAP **07**, 051 (2012), arXiv:1004.2488 [astro-ph.CO].
- Benevento, G., Kable, J. A., Addison, G. E., and Bennett, C. L., Astrophys. J. **935**, 156 (2022), arXiv:2202.09356 [astro-ph.CO].
- Bernal, J. L., Verde, L., and Riess, A. G., JCAP **10**, 019 (2016), arXiv:1607.05617 [astro-ph.CO].
- Beutler, F., Blake, C., Colless, M., Jones, D. H., Staveley-Smith, L., Campbell, L., Parker, Q., Saunders, W., and Watson, F., Mon. Not. Roy. Astron. Soc. **416**, 3017 (2011), arXiv:1106.3366 [astro-ph.CO].
- Beutler, F. and McDonald, P., JCAP **11**, 031 (2021), arXiv:2106.06324 [astro-ph.CO].
- Birrer, S. *et al.*, Astron. Astrophys. **643**, A165 (2020), arXiv:2007.02941 [astro-ph.CO].
- Blakeslee, J. P., Jensen, J. B., Ma, C.-P., Milne, P. A., and Greene, J. E., Astrophys. J. **911**, 65 (2021), arXiv:2101.02221 [astro-ph.CO].
- Blas, D., Lesgourgues, J., and Tram, T., JCAP **07**, 034 (2011), arXiv:1104.2933 [astro-ph.CO].
- Boyle, A. and Komatsu, E., JCAP **03**, 035 (2018), arXiv:1712.01857 [astro-ph.CO].
- Braglia, M., Ballardini, M., Emond, W. T., Finelli, F., Gumrukcuoglu, A. E., Koyama, K., and Paoletti, D., Phys. Rev. D **102**, 023529 (2020a), arXiv:2004.11161 [astro-ph.CO].
- Braglia, M., Ballardini, M., Finelli, F., and Koyama, K., Phys. Rev. D **103**, 043528 (2021), arXiv:2011.12934 [astro-ph.CO].
- Braglia, M., Emond, W. T., Finelli, F., Gumrukcuoglu, A. E., and Koyama, K., Phys. Rev. D **102**, 083513 (2020b), arXiv:2005.14053 [astro-ph.CO].
- Brinckmann, T. and Lesgourgues, J., Phys. Dark Univ. **24**, 100260 (2019), arXiv:1804.07261 [astro-ph.CO].
- Burnham, K. and Anderson, D., *Model selection and multimodel inference: a practical information-theoretic approach* (Springer Verlag, 2002).
- Caldwell, R. R. and Devulder, C., Phys. Rev. D **97**, 023532 (2018), arXiv:1706.03765 [astro-ph.CO].

- Camarena, D. and Marra, V., *Mon. Not. Roy. Astron. Soc.* **504**, 5164 (2021), arXiv:2101.08641 [astro-ph.CO].
- Campeti, P. and Komatsu, E., *Astrophys. J.* **941**, 110 (2022), arXiv:2205.05617 [astro-ph.CO].
- Campeti, P., Özsoy, O., Obata, I., and Shiraishi, M., *JCAP* **07**, 039 (2022), arXiv:2203.03401 [astro-ph.CO].
- Carrasco, J. J. M., Foreman, S., Green, D., and Senatore, L., *JCAP* **07**, 057 (2014), arXiv:1310.0464 [astro-ph.CO].
- Carrasco, J. J. M., Hertzberg, M. P., and Senatore, L., *JHEP* **09**, 082 (2012), arXiv:1206.2926 [astro-ph.CO].
- Carrillo González, M., Liang, Q., Sakstein, J., and Trodden, M., *JCAP* **04**, 063 (2021), arXiv:2011.09895 [astro-ph.CO].
- Carroll, B. W. and Ostlie, D. A., *An Introduction to Modern Astrophysics* (Cambridge University Press, 1996).
- Choi, S. K. *et al.* (ACT), *JCAP* **12**, 045 (2020), arXiv:2007.07289 [astro-ph.CO].
- Chudaykin, A., Gorbunov, D., and Nedelko, N., arXiv-eprints (2022), arXiv:2203.03666 [astro-ph.CO].
- Chudaykin, A., Ivanov, M. M., Philcox, O. H. E., and Simonović, M., *Phys. Rev. D* **102**, 063533 (2020), arXiv:2004.10607 [astro-ph.CO].
- Clark, S. J., Vattis, K., Fan, J., and Koushiappas, S. M., arXiv-eprints (2021), arXiv:2110.09562 [astro-ph.CO].
- Cole, S. *et al.* (2dFGRS), *Mon. Not. Roy. Astron. Soc.* **362**, 505 (2005), arXiv:astro-ph/0501174.
- Cooke, R. J., Pettini, M., and Steidel, C. C., *Astrophys. J.* **855**, 102 (2018), arXiv:1710.11129 [astro-ph.CO].
- Cousins, R. D., *Am. J. Phys.* **63**, 398 (1995).
- Cowan, G., Cranmer, K., Gross, E., and Vitells, O., *Eur. Phys. J. C* **71**, 1554 (2011), arXiv:1007.1727 [physics.data-an].
- Cruz, J. S., Hannestad, S., Holm, E. B., Niedermann, F., Sloth, M. S., and Tram, T., arXiv-eprints (2023), arXiv:2302.07934 [astro-ph.CO].
- Csörnyei, G., Vogl, C., Taubenberger, S., Flörs, A., Blondin, S., Cudmani, M. G., Holas, A., Kressierer, S., Leibundgut, B., and Hillebrandt, W., arXiv-eprints (2023), arXiv:2302.03112 [astro-ph.SR].

- D'Amico, G., Gleyzes, J., Kokron, N., Markovic, K., Senatore, L., Zhang, P., Beutler, F., and Gil-Marín, H., *JCAP* **05**, 005 (2020), arXiv:1909.05271 [astro-ph.CO].
- D'Amico, G., Senatore, L., and Zhang, P., *JCAP* **01**, 006 (2021a), arXiv:2003.07956 [astro-ph.CO].
- D'Amico, G., Senatore, L., Zhang, P., and Zheng, H., *JCAP* **05**, 072 (2021b), arXiv:2006.12420 [astro-ph.CO].
- Das, S., Maharana, A., Poulin, V., and Sharma, R. K., *Phys. Rev. D* **105**, 103503 (2022), arXiv:2104.03329 [astro-ph.CO].
- Desjacques, V., Jeong, D., and Schmidt, F., *Phys. Rept.* **733**, 1 (2018), arXiv:1611.09787 [astro-ph.CO].
- Di Valentino, E. and Bridle, S., *Symmetry* **10**, 585 (2018).
- Di Valentino, E. and Melchiorri, A., *Astrophys. J. Lett.* **931**, L18 (2022), arXiv:2112.02993 [astro-ph.CO].
- Di Valentino, E., Mena, O., Pan, S., Visinelli, L., Yang, W., Melchiorri, A., Mota, D. F., Riess, A. G., and Silk, J., *Class. Quant. Grav.* **38**, 153001 (2021), arXiv:2103.01183 [astro-ph.CO].
- Dodelson, S. and Schmidt, F., *Modern Cosmology* (Elsevier Science, 2020).
- Doran, M., Lilley, M. J., Schwindt, J., and Wetterich, C., *Astrophys. J.* **559**, 501 (2001), arXiv:astro-ph/0012139.
- Doran, M. and Robbers, G., *JCAP* **06**, 026 (2006), arXiv:astro-ph/0601544.
- Dutcher, D. *et al.* (SPT-3G), *Phys. Rev. D* **104**, 022003 (2021), arXiv:2101.01684 [astro-ph.CO].
- Efstathiou, G., arXiv , arXiv:2007.10716 (2020), 2007.10716 [astro-ph.CO].
- Efstathiou, G., *Mon. Not. Roy. Astron. Soc.* **505**, 3866 (2021), arXiv:2103.08723 [astro-ph.CO].
- Eisenstein, D. J. *et al.* (SDSS), *Astrophys. J.* **633**, 560 (2005), arXiv:astro-ph/0501171.
- Ellis, R. *et al.* (PFS Team), *Publ. Astron. Soc. Jap.* **66**, R1 (2014), arXiv:1206.0737 [astro-ph.CO].
- Escudero, M. and Witte, S. J., *Eur. Phys. J. C* **81**, 515 (2021), arXiv:2103.03249 [hep-ph].
- Eskilt, J. R., Herold, L., Komatsu, E., Murai, K., Namikawa, T., and Naokawa, F., arXiv-eprints (2023), arXiv:2303.15369 [astro-ph.CO].
- Feldman, G. J. and Cousins, R. D., *Phys. Rev. D* **57**, 3873 (1998), arXiv:physics/9711021.
- Fixsen, D. J., Cheng, E. S., Gales, J. M., Mather, J. C., Shafer, R. A., and Wright, E. L., *Astrophys. J.* **473**, 576 (1996), arXiv:astro-ph/9605054.

- Freedman, W. L., Madore, B. F., Scowcroft, V., Burns, C., Monson, A., Persson, S. E., Seibert, M., and Rigby, J., *Astrophys. J.* **758**, 24 (2012), arXiv:1208.3281 [astro-ph.CO].
- Freedman, W. L. *et al.*, *Astrophys. J.* **882**, 34 (2019), arXiv:1907.05922 [astro-ph.CO].
- Freese, K. and Winkler, M. W., *Phys. Rev. D* **104**, 083533 (2021), arXiv:2102.13655 [astro-ph.CO].
- Friedmann, A., *Zeitschrift fur Physik* **10**, 377 (1922).
- Gall, E. E. E. *et al.*, *Astron. Astrophys.* **611**, A25 (2018), arXiv:1705.10806 [astro-ph.CO].
- Gebhardt, K. *et al.*, *Astrophys. J.* **923**, 217 (2021), arXiv:2110.04298 [astro-ph.IM].
- Gelman, A. and Rubin, D. B., *Statist. Sci.* **7**, 457 (1992).
- Giusarma, E., Vagnozzi, S., Ho, S., Ferraro, S., Freese, K., Kamen-Rubio, R., and Luk, K.-B., *Phys. Rev. D* **98**, 123526 (2018), arXiv:1802.08694 [astro-ph.CO].
- Gogoi, A., Sharma, R. K., Chanda, P., and Das, S., *Astrophys. J.* **915**, 132 (2021), arXiv:2005.11889 [astro-ph.CO].
- Goldstein, S., Hill, J. C., Iršič, V., and Sherwin, B. D., arXiv-eprints (2023), arXiv:2303.00746 [astro-ph.CO].
- Gómez-Valent, A., *Phys. Rev. D* **106**, 063506 (2022), arXiv:2203.16285 [astro-ph.CO].
- Goroff, M. H., Grinstein, B., Rey, S. J., and Wise, M. B., *Astrophys. J.* **311**, 6 (1986).
- Gross, E., CERN Yellow Rep. School Proc. **3**, 199 (2018).
- Hadzhyska, B., Wolz, K., Azzoni, S., Alonso, D., García-García, C., Ruiz-Zapatero, J., and Slosar, A., arXiv-eprints (2023), arXiv:2301.11895 [astro-ph.CO].
- Hagstotz, S., Reischke, R., and Lilow, R., *Mon. Not. Roy. Astron. Soc.* **511**, 662 (2022), arXiv:2104.04538 [astro-ph.CO].
- Hamann, J., *JCAP* **03**, 021 (2012), arXiv:1110.4271 [astro-ph.CO].
- Hannestad, S., *Phys. Rev. D* **61**, 023002 (2000), arXiv:astro-ph/9911330.
- Hastings, W. K., *Biometrika* **57**, 97 (1970).
- Henrot-Versillé, S., Perdureau, O., Plaszczynski, S., d'Orfeuille, B. R., Spinelli, M., and Tristram, M., arXiv-eprints (2016), arXiv:1607.02964 [astro-ph.CO].
- Herold, L. and Ferreira, E. G. M., arXiv e-prints , arXiv:2210.16296 (2022), arXiv:2210.16296 [astro-ph.CO].

- Herold, L., Ferreira, E. G. M., and Komatsu, E., *Astrophys. J. Lett.* **929**, L16 (2022), arXiv:2112.12140 [astro-ph.CO].
- Hikage, C. *et al.* (HSC), *Publ. Astron. Soc. Jap.* **71**, 43 (2019), arXiv:1809.09148 [astro-ph.CO].
- Hildebrandt, H. *et al.*, *Astron. Astrophys.* **633**, A69 (2020), arXiv:1812.06076 [astro-ph.CO].
- Hill, J. C., McDonough, E., Toomey, M. W., and Alexander, S., *Phys. Rev. D* **102**, 043507 (2020), arXiv:2003.07355 [astro-ph.CO].
- Hill, J. C. *et al.*, *Phys. Rev. D* **105**, 123536 (2022), arXiv:2109.04451 [astro-ph.CO].
- Hinshaw, G. *et al.* (WMAP), *Astrophys. J. Suppl.* **208**, 19 (2013), arXiv:1212.5226 [astro-ph.CO].
- Hogg, R., McKean, J., and Craig, A., *Introduction to Mathematical Statistics*, 7th ed., Always learning (Pearson, 2013) . Theorem 6.1.2.
- Holm, E. B., Herold, L., Hannestad, S., Nygaard, A., and Tram, T., *Phys. Rev. D* **107**, L021303 (2023), arXiv:2211.01935 [astro-ph.CO].
- Holm, E. B., Tram, T., and Hannestad, S., *JCAP* **08**, 044 (2022), arXiv:2205.13628 [astro-ph.CO].
- Hou, Z. *et al.*, *Astrophys. J.* **782**, 74 (2014), arXiv:1212.6267 [astro-ph.CO].
- Ilić, S., Sakr, Z., and Blanchard, A., *Astron. Astrophys.* **631**, A96 (2019), arXiv:1908.00163 [astro-ph.CO].
- Ivanov, M. M., McDonough, E., Hill, J. C., Simonović, M., Toomey, M. W., Alexander, S., and Zaldarriaga, M., *Phys. Rev. D* **102**, 103502 (2020a), arXiv:2006.11235 [astro-ph.CO].
- Ivanov, M. M. and Sibiriyakov, S., *JCAP* **07**, 053 (2018), arXiv:1804.05080 [astro-ph.CO].
- Ivanov, M. M., Simonović, M., and Zaldarriaga, M., *JCAP* **05**, 042 (2020b), arXiv:1909.05277 [astro-ph.CO].
- de Jaeger, T., Galbany, L., Riess, A. G., Stahl, B. E., Shappee, B. J., Filippenko, A. V., and Zheng, W., *Mon. Not. Roy. Astron. Soc.* **514**, 4620 (2022), arXiv:2203.08974 [astro-ph.CO].
- Jain, B. and Bertschinger, E., *Astrophys. J.* **431**, 495 (1994), arXiv:astro-ph/9311070.
- James, F. and Roos, M., *Comput. Phys. Commun.* **10**, 343 (1975).
- Jedamzik, K. and Pogosian, L., *Phys. Rev. Lett.* **125**, 181302 (2020), arXiv:2004.09487 [astro-ph.CO].
- Jeong, D. and Komatsu, E., *Astrophys. J.* **651**, 619 (2006), arXiv:astro-ph/0604075.
- Jimenez, R., Cimatti, A., Verde, L., Moresco, M., and Wandelt, B., *JCAP* **03**, 043 (2019), arXiv:1902.07081 [astro-ph.CO].

- Kamionkowski, M., Pradler, J., and Walker, D. G. E., Phys. Rev. Lett. **113**, 251302 (2014), arXiv:1409.0549 [hep-ph].
- Kamionkowski, M. and Riess, A. G., arXiv-eprints (2022), arXiv:2211.04492 [astro-ph.CO].
- Kappl, R., Nilles, H. P., and Winkler, M. W., Phys. Lett. B **753**, 653 (2016), arXiv:1511.05560 [hep-th].
- Karwal, T. and Kamionkowski, M., Phys. Rev. D **94**, 103523 (2016), arXiv:1608.01309 [astro-ph.CO].
- Karwal, T., Raveri, M., Jain, B., Khoury, J., and Trodden, M., Phys. Rev. D **105**, 063535 (2022), arXiv:2106.13290 [astro-ph.CO].
- Knox, L. and Millea, M., Phys. Rev. D **101**, 043533 (2020), arXiv:1908.03663 [astro-ph.CO].
- Komatsu, E., Nature Rev. Phys. **4**, 452 (2022), arXiv:2202.13919 [astro-ph.CO].
- Krishnan, C., Colgáin, E. O., Ruchika, Sen, A. A., Sheikh-Jabbari, M. M., and Yang, T., Phys. Rev. D **102**, 103525 (2020), arXiv:2002.06044 [astro-ph.CO].
- La Posta, A., Louis, T., Garrido, X., and Hill, J. C., Phys. Rev. D **105**, 083519 (2022), arXiv:2112.10754 [astro-ph.CO].
- Laureijs, R. e. a., arXiv (2011), 1110.3193 [astro-ph.CO].
- Lemos, P., Lee, E., Efstathiou, G., and Gratton, S., Mon. Not. Roy. Astron. Soc. **483**, 4803 (2019), arXiv:1806.06781 [astro-ph.CO].
- Lesgourgues, J., arXiv-eprints (2011), arXiv:1104.2932 [astro-ph.IM].
- Lesgourgues, J. and Pastor, S., Phys. Rept. **429**, 307 (2006), arXiv:astro-ph/0603494.
- Lewandowski, M., Senatore, L., Prada, F., Zhao, C., and Chuang, C.-H., Phys. Rev. D **97**, 063526 (2018), arXiv:1512.06831 [astro-ph.CO].
- Lewis, A., arXiv-eprints (2019), arXiv:1910.13970 [astro-ph.IM].
- Lewis, A., Challinor, A., and Lasenby, A., Astrophys. J. **538**, 473 (2000), arXiv:astro-ph/9911177.
- Lin, M.-X., Benevento, G., Hu, W., and Raveri, M., Phys. Rev. D **100**, 063542 (2019), arXiv:1905.12618 [astro-ph.CO].
- Lista, L., *Statistical Methods for Data Analysis in Particle Physics*, Vol. 909 (Springer, 2016).
- Mather, J. C., Fixsen, D. J., Shafer, R. A., Mosier, C., and Wilkinson, D. T., Astrophys. J. **512**, 511 (1999), arXiv:astro-ph/9810373.

- Metropolis, N., Rosenbluth, A. W., Rosenbluth, M. N., Teller, A. H., and Teller, E., *J. Chem. Phys.* **21**, 1087 (1953).
- Misner, C. W., Thorne, K. S., and Wheeler, J. A., *Gravitation* (W. H. Freeman, San Francisco, 1973).
- Mortsell, E., Goobar, A., Johansson, J., and Dhawan, S., *Astrophys. J.* **933**, 212 (2022), arXiv:2105.11461 [astro-ph.CO].
- Mukhanov, V., *Physical Foundations of Cosmology* (Cambridge University Press, 2005).
- Mukhanov, V. F., Feldman, H. A., and Brandenberger, R. H., *Phys. Rept.* **215**, 203 (1992).
- Murai, K., Naokawa, F., Namikawa, T., and Komatsu, E., *Phys. Rev. D* **107**, L041302 (2023), arXiv:2209.07804 [astro-ph.CO].
- Murgia, R., Abellán, G. F., and Poulin, V., *Phys. Rev. D* **103**, 063502 (2021), arXiv:2009.10733 [astro-ph.CO].
- Neyman, J., *Phil. Trans. Roy. Soc. Lond. A* **236**, 333 (1937).
- Niedermann, F. and Sloth, M. S., *Phys. Rev. D* **102**, 063527 (2020), arXiv:2006.06686 [astro-ph.CO].
- Niedermann, F. and Sloth, M. S., *Phys. Rev. D* **103**, L041303 (2021), arXiv:1910.10739 [astro-ph.CO].
- Niedermann, F. and Sloth, M. S., *Phys. Rev. D* **105**, 063509 (2022), arXiv:2112.00770 [hep-ph].
- Nojiri, S., Odintsov, S. D., Saez-Chillon Gomez, D., and Sharov, G. S., *Phys. Dark Univ.* **32**, 100837 (2021), arXiv:2103.05304 [gr-qc].
- Nunes, R. C. and Vagnozzi, S., *Mon. Not. Roy. Astron. Soc.* **505**, 5427 (2021), arXiv:2106.01208 [astro-ph.CO].
- Nygaard, A., Tram, T., and Hannestad, S., *JCAP* **05**, 017 (2021), arXiv:2011.01632 [astro-ph.CO].
- Oikonomou, V. K., *Phys. Rev. D* **103**, 044036 (2021), arXiv:2012.00586 [astro-ph.CO].
- Perivolaropoulos, L. and Skara, F., *New Astron. Rev.* **95**, 101659 (2022), arXiv:2105.05208 [astro-ph.CO].
- Perko, A., Senatore, L., Jennings, E., and Wechsler, R. H., arXiv-eprints (2016), arXiv:1610.09321 [astro-ph.CO].
- Pesce, D. W. *et al.*, *Astrophys. J. Lett.* **891**, L1 (2020), arXiv:2001.09213 [astro-ph.CO].
- Philcox, O. H. E. and Ivanov, M. M., *Phys. Rev. D* **105**, 043517 (2022), arXiv:2112.04515 [astro-ph.CO].

- Philcox, O. H. E., Ivanov, M. M., Simonović, M., and Zaldarriaga, M., *JCAP* **05**, 032 (2020), arXiv:2002.04035 [astro-ph.CO].
- Poulin, V., Smith, T. L., and Bartlett, A., *Phys. Rev. D* **104**, 123550 (2021), arXiv:2109.06229 [astro-ph.CO].
- Poulin, V., Smith, T. L., Grin, D., Karwal, T., and Kamionkowski, M., *Phys. Rev. D* **98**, 083525 (2018), arXiv:1806.10608 [astro-ph.CO].
- Poulin, V., Smith, T. L., and Karwal, T., arXiv-eprints (2023), arXiv:2302.09032 [astro-ph.CO].
- Poulin, V., Smith, T. L., Karwal, T., and Kamionkowski, M., *Phys. Rev. Lett.* **122**, 221301 (2019), arXiv:1811.04083 [astro-ph.CO].
- Reeves, A., Herold, L., Vagnozzi, S., Sherwin, B. D., and Ferreira, E. G. M., *Mon. Not. Roy. Astron. Soc.* **520**, 3688 (2023), arXiv:2207.01501 [astro-ph.CO].
- Refsdal, S., *Mon. Not. Roy. Astron. Soc.* **128**, 307 (1964).
- Riess, A. G., Casertano, S., Yuan, W., Bowers, J. B., Macri, L., Zinn, J. C., and Scolnic, D., *Astrophys. J. Lett.* **908**, L6 (2021), arXiv:2012.08534 [astro-ph.CO].
- Riess, A. G., Casertano, S., Yuan, W., Macri, L. M., and Scolnic, D., *Astrophys. J.* **876**, 85 (2019), arXiv:1903.07603 [astro-ph.CO].
- Riess, A. G., Macri, L., Casertano, S., Lampeitl, H., Ferguson, H. C., Filippenko, A. V., Jha, S. W., Li, W., and Chornock, R., *Astrophys. J.* **730**, 119 (2011), arXiv:1103.2976 [astro-ph.CO].
- Riess, A. G. *et al.*, *Astrophys. J. Lett.* **934**, L7 (2022), arXiv:2112.04510 [astro-ph.CO].
- Robertson, H. P., *Astrophys. J.* **82**, 284 (1935).
- Ross, A. J., Samushia, L., Howlett, C., Percival, W. J., Burden, A., and Manera, M., *Mon. Not. Roy. Astron. Soc.* **449**, 835 (2015), arXiv:1409.3242 [astro-ph.CO].
- Roy Choudhury, S. and Hannestad, S., *JCAP* **07**, 037 (2020), arXiv:1907.12598 [astro-ph.CO].
- Sabla, V. I. and Caldwell, R. R., *Phys. Rev. D* **106**, 063526 (2022), arXiv:2202.08291 [astro-ph.CO].
- Sakr, Z., Ilic, S., and Blanchard, A., *Astron. Astrophys.* **666**, A34 (2022), arXiv:2112.14171 [astro-ph.CO].
- Sakstein, J. and Trodden, M., *Phys. Rev. Lett.* **124**, 161301 (2020), arXiv:1911.11760 [astro-ph.CO].
- Sasaki, M., *Prog. Theor. Phys.* **76**, 1036 (1986).

- Schmidt, B. P., Kirshner, R. P., and Eastman, R. G., *Astrophys. J.* **395**, 366 (1992), arXiv:astro-ph/9204004.
- Schöneberg, N. and Franco Abellán, G., *JCAP* **12**, 001 (2022), arXiv:2206.11276 [astro-ph.CO].
- Schöneberg, N., Franco Abellán, G., Pérez Sánchez, A., Witte, S. J., Poulin, V., and Lesgourgues, J., *Phys. Rept.* **984**, 1 (2022), arXiv:2107.10291 [astro-ph.CO].
- Schutz, B. F., *Nature* **323**, 310 (1986).
- Scoccimarro, R. and Frieman, J., *Astrophys. J. Suppl.* **105**, 37 (1996a), arXiv:astro-ph/9509047.
- Scoccimarro, R. and Frieman, J., *Astrophys. J.* **473**, 620 (1996b), arXiv:astro-ph/9602070.
- Scolnic, D. *et al.*, *Astrophys. J.* **938**, 113 (2022), arXiv:2112.03863 [astro-ph.CO].
- Secco, L. F., Karwal, T., Hu, W., and Krause, E., arXiv-eprints (2022), arXiv:2209.12997 [astro-ph.CO].
- Sekiguchi, T. and Takahashi, T., *Phys. Rev. D* **103**, 083507 (2021), arXiv:2007.03381 [astro-ph.CO].
- Senatore, L. and Zaldarriaga, M., arXiv-eprints (2014), arXiv:1409.1225 [astro-ph.CO].
- Senatore, L. and Zaldarriaga, M., *JCAP* **02**, 013 (2015), arXiv:1404.5954 [astro-ph.CO].
- Shajib, A. J. *et al.*, arXiv-eprints (2023), arXiv:2301.02656 [astro-ph.CO].
- Simon, T., Zhang, P., Poulin, V., and Smith, T. L., arXiv-eprints (2022), arXiv:2208.05929 [astro-ph.CO].
- Simon, T., Zhang, P., Poulin, V., and Smith, T. L., *Phys. Rev. D* **107**, 063505 (2023), arXiv:2208.05930 [astro-ph.CO].
- Smith, R. E., Peacock, J. A., Jenkins, A., White, S. D. M., Frenk, C. S., Pearce, F. R., Thomas, P. A., Efstathiou, G., and Couchmann, H. M. P. (VIRGO Consortium), *Mon. Not. Roy. Astron. Soc.* **341**, 1311 (2003), arXiv:astro-ph/0207664.
- Smith, T. L., Lucca, M., Poulin, V., Abellan, G. F., Balkenhol, L., Benabed, K., Galli, S., and Murgia, R., *Phys. Rev. D* **106**, 043526 (2022), arXiv:2202.09379 [astro-ph.CO].
- Smith, T. L., Poulin, V., and Amin, M. A., *Phys. Rev. D* **101**, 063523 (2020), arXiv:1908.06995 [astro-ph.CO].
- Smith, T. L., Poulin, V., Bernal, J. L., Boddy, K. K., Kamionkowski, M., and Murgia, R., *Phys. Rev. D* **103**, 123542 (2021), arXiv:2009.10740 [astro-ph.CO].
- Suyu, S. H., Chang, T.-C., Courbin, F., and Okumura, T., *Space Sci. Rev.* **214**, 91 (2018), arXiv:1801.07262 [astro-ph.CO].

- Suyu, S. H. *et al.*, Mon. Not. Roy. Astron. Soc. **468**, 2590 (2017), arXiv:1607.00017 [astro-ph.CO].
- Suyu, S. H. *et al.*, Astron. Astrophys. **644**, A162 (2020), arXiv:2002.08378 [astro-ph.CO].
- Tanseri, I., Hagstotz, S., Vagnozzi, S., Giusarma, E., and Freese, K., JHEAp **36**, 1 (2022), arXiv:2207.01913 [astro-ph.CO].
- Taruya, A., Nishimichi, T., and Saito, S., Phys. Rev. D **82**, 063522 (2010), arXiv:1006.0699 [astro-ph.CO].
- Vagnozzi, S., Phys. Rev. D **104**, 063524 (2021), arXiv:2105.10425 [astro-ph.CO].
- Vagnozzi, S., Dhawan, S., Gerbino, M., Freese, K., Goobar, A., and Mena, O., Phys. Rev. D **98**, 083501 (2018), arXiv:1801.08553 [astro-ph.CO].
- Vagnozzi, S., Giusarma, E., Mena, O., Freese, K., Gerbino, M., Ho, S., and Lattanzi, M., Phys. Rev. D **96**, 123503 (2017), arXiv:1701.08172 [astro-ph.CO].
- Verde, L., arXiv-eprints (2007), arXiv:0712.3028 [astro-ph].
- Vlah, Z., Seljak, U., Chu, M. Y., and Feng, Y., JCAP **03**, 057 (2016), arXiv:1509.02120 [astro-ph.CO].
- Wald, R. M., *General Relativity* (Chicago Univ. Pr., Chicago, USA, 1984).
- Walker, A. G., Proceedings of the London Mathematical Society **42**, 90 (1937).
- Weinberg, S., *Cosmology* (Oxford University Press, 2008).
- Wetterich, C., Phys. Lett. B **594**, 17 (2004), arXiv:astro-ph/0403289.
- Wilks, S. S., Annals Math. Statist. **9**, 60 (1938).
- Wong, K. C. *et al.*, Mon. Not. Roy. Astron. Soc. **498**, 1420 (2020), arXiv:1907.04869 [astro-ph.CO].
- Workman, R. L. *et al.* (Particle Data Group), PTEP **2022**, 083C01 (2022).
- Ye, G. and Piao, Y.-S., Phys. Rev. D **101**, 083507 (2020), arXiv:2001.02451 [astro-ph.CO].
- Ye, G., Zhang, J., and Piao, Y.-S., Phys. Lett. B **839**, 137770 (2023), arXiv:2107.13391 [astro-ph.CO].
- Yeche, C., Ealet, A., Refregier, A., Tao, C., Tilquin, A., Virey, J. M., and Yvon, D., Astron. Astrophys. **448**, 831 (2006), arXiv:astro-ph/0507170.
- Yuan, W., Riess, A. G., Macri, L. M., Casertano, S., and Scolnic, D., Astrophys. J. **886**, 61 (2019), arXiv:1908.00993 [astro-ph.GA].

Zel'dovich, Y. B., *Astron. Astrophys.* **5**, 84 (1970).

Zumalacarregui, M., *Phys. Rev. D* **102**, 023523 (2020), arXiv:2003.06396 [astro-ph.CO].

Acknowledgements

First and foremost, I would like to thank my supervisor Eiichiro Komatsu for his continuous guidance and encouragement during all stages of my PhD, while creating such a friendly and fun work environment. I am incredibly grateful for my time at MPA and all the things that I learned from him.

I want to express my deep gratitude towards Elisa Ferreira who was essentially my second supervisor. It was so much fun to work on our projects together and I learned so much! I would like to thank her for her friendship and constant support both scientifically and personally, her advice about all aspects of academia, and for inviting me to Japan, where I had an amazing time.

I would also like to thank my other collaborators Emil Holm, Alex Reeves, Sunny Vagnozzi, Steen Hannestad, and Thomas Tram for the super interesting and fun projects we worked on during my PhD and for learning a lot from them. Further, I would like to thank Vivian Poulin and Théo Simon for the fun time we had in Montpellier while working on our project together.

Thank you to Paolo Campeti, Elisa Ferreira, Emil Holm, Klaus Liegener, Andrija Kostic, Marta Monelli, Vyoma Muralidhara, Théo Simon, and Julia Stadler for their patient proof-reading and very helpful comments on the thesis.

I am grateful to my friends who I met at MPA. To Marta and Vyoma for sharing the ups and downs of the PhD with me, innumerable coffee breaks, and lots of great memories from pouring paintings to Alpaka hikes. To Agne for being my best MPE-twin-JC buddy, her kindness and fun nature. To Chris, Leila, Linda, Sam, Alex and Fabian for sharing their wisdom with me. To Eirini and Maja for being great office mates in the best office at MPA. To Julia, Henrique, Bea, Jose, Ipei, Paolo, Sten, Luisa, Minh, Andrija, Angelo, Drew, Silvia, Abhijeet, Miha, and Ivan who were always there for helping me and many fun discussions.

Außerdem würde ich gerne meiner Familie – Gisela, Thomas, Felix und Selli – für all die Unterstützung während meines gesamten Studiums danken, auf die ich mich immer verlassen konnte und ohne die all das nicht möglich gewesen wäre. Zum Schluss möchte ich Klaus von ganzem Herzen dafür danken, dass er all die Jahre sowohl in den schönsten als auch in den schwierigsten Momenten immer an meiner Seite war.